

# Projections and correlations in the fractional quantum Hall effect

Jørgen Fulsebakke



Thesis presented for the degree of

Doctor of Philosophy

to the

National University of Ireland Maynooth

Department of Mathematical Physics

February 2016

Department Head

Professor Daniel M. Heffernan

Research advisor

J. K. Slingerland

# Abstract

More than 30 years after its surprising experimental discovery, the quantum Hall effect remains one of the most active and interesting fields of research in condensed matter physics. The theory pertaining to the phenomenon comprises a hugely varied and fascinating body of work, incorporating frameworks such as variational trial wavefunctions, topological phases, conformal field theory and more. There are reasons to expect that some phases of the system harbour nonabelian excitations: particles whose interchange affects the state of the whole system in a way depending on the order of exchange. This has been proposed as a suitable basis for noise resistant quantum computing.

The excitations are an emergent property of the totality of the system, whose main active constituent is the well understood electron. The electrons act together in such a way as to manifest exotic quasiparticles; these kinds of strong correlations are a general feature of the system. One can argue that the quantum Hall effect shows the limits of reductionism.

In this work we focus on trial wavefunctions as descriptions of the phenomenon. Although highly successful in the past their evaluation is often impeded by a feature known as lowest Landau level projection. We approach the projection from several angles and in this context introduce an effective and general technique termed energy projection. Using this we examine several trial wavefunctions that have been difficult to deal with in the past.

The quantity known as the pair correlation function is an important tool for the analysis of wavefunctions. Its study, however, has often been mainly qualitative in the literature. We construct an expansion useful for exact characterisation and comparison of pair correlations and show that it has desirable properties as compared to a similar preexisting expansion. This is then used to scale pair correlation functions to macroscopic sizes.

# Acknowledgements

I would like to thank my supervisor Joost K. Slingerland, whose plentiful ideas, clear reasoning, insightful explanations and sheer enthusiasm has made this work possible and a delight to carry out. Furthermore I express my sincere thanks to Niall Moran and Mikael Fremling, who I have had the pleasure to collaborate with and learn from. Niall deserves special mention, having been of invaluable help on numerous occasions.

For creating a relaxed and enjoyable environment in which I have been lucky to work I thank my colleagues through several years: Robert Ainsworth, Aoife Kelly, Paul Watts, John Brennan, Úna Ní Ruairc, Olaf Smits, Sepanda Pouryahya, Iván D. Rodríguez, Elena Green, Tamer Boz, Stephen Nulty, Layla Hormozi, Graham Kells, Seamus Cotter, Domenico Pellegrino and Darragh Millar.

Finally I thank my friends and family for sharing this voyage through space. This goes especially for my best friend Arash Saidi, the *kjørvest* of them all, and the love of my life Saioa Arostegi Urrutia, who is out of a dream of music sublime.

This work was supported by Science Foundation Ireland through Investigator Award 12/IA/1697 and PI Award 08/IN.1/I1961. The SFI/HEA Irish Centre for High-End Computing (ICHEC) provided computational facilities and support.

# Contents

<b>1</b>	<b>Introduction</b>	<b>5</b>
1.1	The Quantum Hall effect . . . . .	5
1.1.1	The classical effect . . . . .	5
1.1.2	The integer effect . . . . .	6
1.1.3	The fractional effect . . . . .	10
1.2	Objectives and outline . . . . .	10
<b>2</b>	<b>Relevant background</b>	<b>14</b>
2.1	The Hamiltonian . . . . .	14
2.1.1	The single particle case . . . . .	14
2.1.2	The many particle case . . . . .	16
2.2	Geometry and single particle wavefunctions . . . . .	18
2.2.1	The slab and the disk . . . . .	19
2.2.2	The sphere . . . . .	21
2.2.3	The torus . . . . .	25
2.2.4	The second Landau level . . . . .	25
2.3	Pair correlation functions . . . . .	26
<b>3</b>	<b>Review of trial wavefunctions</b>	<b>29</b>
3.1	Ground states and excitations . . . . .	29
3.1.1	Quasiparticles . . . . .	29
3.1.2	Anyons . . . . .	30
3.2	Laughlin and the hierarchy . . . . .	31
3.2.1	Laughlin . . . . .	31
3.2.2	Laughlin quasiparticles . . . . .	32
3.2.3	The Haldane-Halperin hierarchy . . . . .	33
3.3	Jain's composite fermions . . . . .	34
3.3.1	Ground states . . . . .	34
3.3.2	Excited states . . . . .	36
3.4	Bonderson-Slingerland . . . . .	37
3.4.1	Conformal field theory . . . . .	37
3.4.2	Moore-Read . . . . .	38
3.4.3	A second Landau level hierarchy . . . . .	40

<b>4</b>	<b>Numerical methods</b>	<b>43</b>
4.1	Exact diagonalisation . . . . .	43
4.2	Monte Carlo . . . . .	45
4.2.1	Approximating integrals . . . . .	45
4.2.2	Monte Carlo on the sphere . . . . .	50
4.2.3	Error estimation . . . . .	51
<b>5</b>	<b>Results from trial wavefunctions</b>	<b>53</b>
5.1	Lowest Landau level Projection . . . . .	53
5.1.1	Exact projection . . . . .	53
5.1.2	Jain-Kamilla projection . . . . .	55
5.1.3	Energy projection . . . . .	58
5.2	Quantities to be computed . . . . .	63
5.2.1	Energy spectra . . . . .	63
5.2.2	Eigenstate overlaps . . . . .	66
5.2.3	Pair correlation functions . . . . .	66
5.3	Reverse flux composite fermions . . . . .	67
5.3.1	Energies . . . . .	67
5.3.2	Overlaps . . . . .	70
5.4	Bonderson-Slingerland . . . . .	72
5.4.1	Quasiholes . . . . .	75
5.5	Modified states . . . . .	76
5.5.1	Laughlin at filling $\nu = 1/3$ . . . . .	77
5.5.2	$\nu = 1/3$ as a reverse flux composite fermion state . . . . .	83
5.5.3	Modified composite fermions . . . . .	86
<b>6</b>	<b>Pair correlation functions decomposed</b>	<b>93</b>
6.1	Planar decomposition . . . . .	93
6.2	Spherical orthogonal decomposition . . . . .	95
6.2.1	Decomposition basis . . . . .	95
6.2.2	Condition number . . . . .	98
6.3	Testing the decomposition . . . . .	99
6.4	Pair correlation functions in the thermodynamic limit . . . . .	103
<b>7</b>	<b>Summary and outlook</b>	<b>110</b>
<b>A</b>	<b>The <math>\nu = 1</math> pair correlation function on the sphere</b>	<b>114</b>
<b>B</b>	<b>Proof of spherical basis orthonormality</b>	<b>117</b>

# Chapter 1

## Introduction

### 1.1 The Quantum Hall effect

This chapter introduces the quantum Hall effect as a phenomenon and highlights features important to this work. The treatments of relevant fundamental topics in this chapter and the next are based on refs. [1–4].

#### 1.1.1 The classical effect

The classical Hall effect [5] occurs in a conducting slab when a magnetic field is applied perpendicular to the slab while a current is running through it. The magnetic Lorentz force will add a perpendicular acceleration to the electrostatic one and give the carriers a curved path, causing charge to build up on the sides parallel to the current until the resulting electrostatic force cancels the magnetic one. Resulting is a situation where there is a voltage perpendicular to the current, and thus a transverse Hall resistivity  $\rho_H$ .

The latter can be determined using a semiclassical model and relativistic arguments. The charge carriers are modelled as classical particles of charge  $Q$  and density  $n$  comprising a current with an average velocity  $\mathbf{v}$ . In a frame  $S'$  moving with the current they are stationary and there is no external electric field, giving the electric and magnetic fields

$$\mathbf{B}' = -B'e_z \quad \text{and} \quad \mathbf{E}' = 0, \quad (1.1)$$

where  $B > 0$  is the applied magnetic field (pointing in the negative  $z$ -direction to simplify some expressions). Transferring to a second frame  $S$  where the Hall effect is observed, thus moving with a relative velocity  $-\mathbf{v}$  to  $S'$ , one sees a charge density  $\mathbf{j} = nQ\mathbf{v}$ . The Lorentz transformations give for this frame

## 1.1. THE QUANTUM HALL EFFECT

(up to first order in  $v/c$ ):

$$\mathbf{B} = -B\mathbf{e}_z \quad \text{and} \quad \mathbf{E} = \frac{B}{nQ}\mathbf{j} \times \mathbf{e}_z, \quad (1.2)$$

indicating zero longitudinal resistivity and a transverse Hall resistivity

$$\rho_H = \frac{B}{nQ}, \quad (1.3)$$

proportional to the ratio of magnetic field to carrier density. From this point on the carriers will be assumed to be electrons:  $Q = e$ .

The filling factor  $\nu$  gives a measure of filled electron states per magnetic field and is defined as

$$\nu = \frac{n}{N_\Phi}, \quad (1.4)$$

where  $N_\Phi = B/\Phi_0$  is the number of magnetic flux quanta  $\Phi_0 = h/e$  piercing the sample. In terms of the filling factor the transverse resistivity is

$$\rho_H = \frac{h}{\nu e^2}. \quad (1.5)$$

A more realistic model taking disorder into account will include a longitudinal resistivity, but the estimate (1.5) is robust.

### 1.1.2 The integer effect

It was discovered that when the sample is effectively two-dimensional, the external magnetic field is strong and the temperature approaches absolute zero, the Hall resistivity does not follow (1.5). On certain values of  $\nu$  it does, but around these it is constant with the magnetic field, creating plateaus in a plot of the Hall resistance  $R_H$  versus  $B$ ; see figure 1.1. The filling factors at which the plateaus are observed are indicated with arrows in the figure. Between plateaus the behaviour of  $\rho_H$  is approximately linear, but depending on how clean the sample is it may be completely dominated by the plateaus. Integer filling factors plateaus  $\nu \in \mathbb{N}$  were the first to be discovered [6], and this phenomenon is now called the integer quantum Hall effect (IQHE).

The integer effect can be explained from a single particle perspective. Charged particles in a magnetic field organise themselves in highly degenerate kinetic energy levels called Landau levels (LL), whose separation is proportional to  $B$  and whose degeneracy per unit area is equal to  $N_\Phi$  (see sections 2.1.1 and 2.2.1). This gives another meaning to  $\nu$  as the occupation of Landau

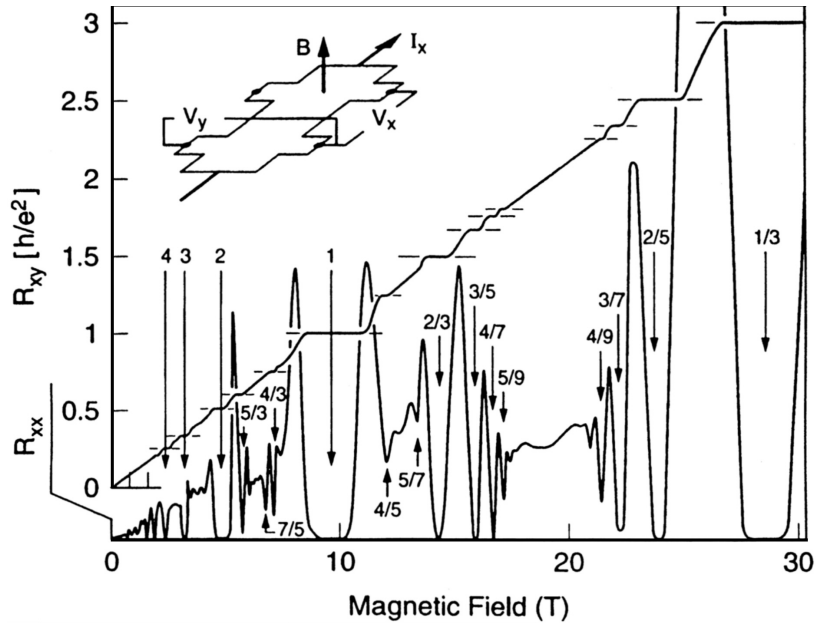


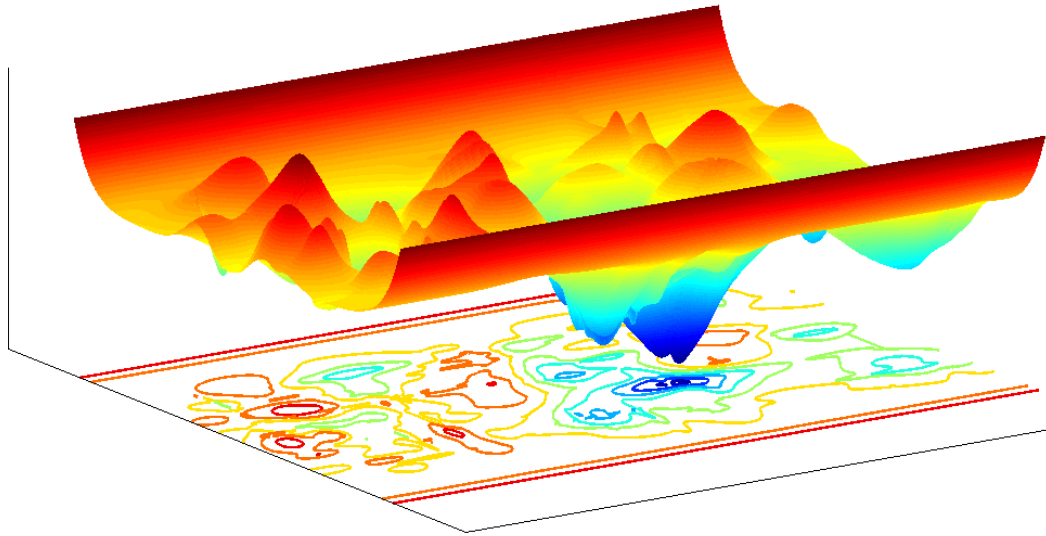
Figure 1.1: Measurement of the quantum Hall effect. The  $x$ -axis shows the perpendicular magnetic field  $B$ , and the primary  $y$ -scale gives the transverse Hall resistance  $R_{xy}$ . The latter has plateaus on certain values of the filling factor  $\nu$ , which are also accompanied by a drop in the longitudinal resistance  $R_{xx}$  (superimposed). Level lines besides  $R_{xy}$  and arrows to  $R_{xx}$  indicate plateaus. Reprinted with permission from ref. [7].

levels. From (1.4) this means that the middle of the IQHE plateau occurs when  $\nu$  Landau levels are completely filled.

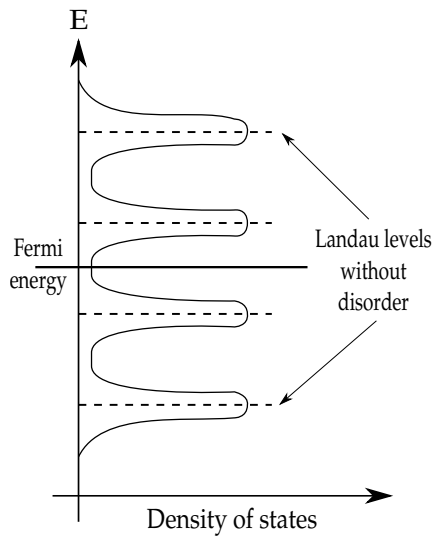
The following picture of the IQHE depends crucially on disorder; impurities in the sample that widen the original LL's and create a potential landscape within each level together with the steeper confining potential at the edge. A sketch of this is shown in figure 1.2a. Due to the strong magnetic field there will be a large gap in kinetic energy, meaning that the electron states are strongly confined to equipotential lines. Some of these are drawn at the bottom of the sketch.

Thus the bulk states with energy away from the middle of the widened Landau levels are localised, either around a “peak” or a “valley”. Those around the middle on the other hand are extended, as the potential contours reach from one edge of the sample to the other. In addition all states confined to equipotentials at the boundary are extended. These are called edge states, and they have some interesting properties discussed further below.

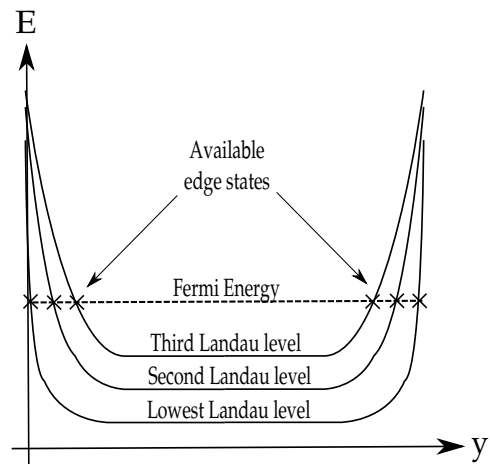
When the filling factor is an integer  $\nu = n$  the Fermi energy will lie near the highest contours associated with the Landau level  $E_{n-1}$  (without disorder) and the lowest contours at  $E_n$ , i.e. close to a point between two original LL's and thus in a gap between extended bulk states. This is indicated in a sketch of the density of states in figure 1.2b.



(a) Potential landscape in a Landau level with disorder and confining edges (not to scale). Electron states will be confined to equipotential contour lines, indicated at the bottom. Thus the edge states are extended while the bulk states are localised except close to the middle of the original level.



(b) Density of states as a function of energy. Only the bulk states located around the original Landau levels (without disorder) are extended. The IQHE occurs when the Fermi energy lies in a gap between extended bulk states.



(c) Energy levels in a cross section perpendicular to the current. The number of conducting edge states at the Fermi energy (indicated with crosses) depends on how many Landau levels lie below.

Figure 1.2: Sketches illustrating the integer quantum Hall effect.

## 1.1. THE QUANTUM HALL EFFECT

With the temperature being near zero only states around the Fermi energy are available, of which the edge states alone are extended and can contribute to electronic transport. The number of available conducting edge states depends on how many of the original Landau levels lie below the Fermi energy; as the corresponding edge states are shifted upwards by the confining potential. A sketch of a cross section perpendicular to the current in figure 1.2c illustrates this. It can be demonstrated that the resulting resistivity is equal to (1.5) with  $\nu = n$ .

Now to explain the plateaus, i.e. why the resistivity does not change when the magnetic field and therefore the filling factor  $\nu$  does. Changing the number of magnetic flux also changes the number of states in each Landau level, thus effectively shifting the Fermi energy. Decreasing the magnetic field gives fewer states per level, meaning that incoming electrons start occupying states higher in the landscape. But although the Fermi energy moves upwards in the sketches of figures 1.2b and 1.2c, there are still the same amount of conducting states available, corresponding to the number of LL's below the Fermi energy. Therefore the conductivity does not change and so neither does the resistivity.

This continues until the conducting bulk states at the middle of  $E_n$ , the next Landau level, become available; at which time the plateau comes to an end. Subsequently the story repeats but this time with another set of edge states from  $E_n$  included and thus a higher conductivity and a lower resistance – those of the next plateau. In an increasing magnetic field an analogous picture with electrons substituted for holes yields the same conclusions.

According to the reasoning above the current is carried along the edges when on a QHE plateau. It can be demonstrated that the edge states are chiral, in the sense that they can only move in one direction. This is done e.g. by placing the Landau gauge wavefunctions (section 2.2.1) in a potential of mild disorder plus approximately transversely symmetric edge potentials [4]. Therefore there is no backscattering and the current runs in a sense around the sample, leading to zero longitudinal resistivity. In addition to the plateaus the vanishing dissipative resistance is another signature of the quantum Hall effect, and in fact often more easily detected in experiments. It is also depicted in figure 1.1.

To summarise, a gap between single particle energy levels without disorder and edges leads to localised bulk states when the latter are included, with the exception of the middle of the levels. Considering the effect on this system of a changing magnetic field in a low temperature, together with properties of

the edge states, explains the quantum Hall effect.

The distribution of states in the bulk is often termed a mobility gap. This emphasises the fact that there may be plenty of accessible electron states at the Fermi energy but only some of them can carry current. The phase where the effect occurs is thus characterised by incompressibility from a charge transport perspective, in the sense that an excitation with energy above some minimal value, the mobility gap, is necessary to induce a response.

### 1.1.3 The fractional effect

According to the previous sections there should be nothing special happening between the integer plateaus, with the resistivity increasing in a manner somewhere between a step (localised quantum states) and linearly with magnetic field (the classical case) depending on the relative strength of the disorder potential. But soon after the discovery of the integer effect the same phenomenon was observed at fractional fillings – first at  $\nu = 1/3$  and  $2/3$  [8], then at many other odd denominators [9–14] and some even ones [15, 16]. This is called the fractional quantum Hall effect (FQHE).

The model of the integer effect does not predict any mobility gaps between integer  $\nu$ , and it turns out what is lacking is inclusion of electron interactions. These must act to create an incompressible phase at the observed fractions, or in other words to form a gap in the bulk in the absence of disorder. The strength of the interactions thus needs to be at least comparable to that of the impurities or one will only observe the integer effect. In keeping with this the fractional effect only occurs in exceptionally clean samples.

The inclusion of interactions makes models and theories of the FQHE more complicated than those of the IQHE. Prominent examples of the former include effective field theories (in particular Chern-Simons and conformal field theories), anyon models, diagonalisation of the Hamiltonian and variational trial wavefunctions. The latter are the main focus of this work.

## 1.2 Objectives and outline

As seen in the previous section any model of a plateau in the fractional quantum Hall effect must predict a gap (or at least a mobility gap) in the absence of disorder, and reproduce other properties such as the filling factor. One category of such models that has been strikingly successful since the early days of FQHE investigations is that of trial wavefunctions. Despite being variational,

they generally do not have many parameters that are not fixed by constraints like quantum numbers and symmetries of the system.

Typically a given trial wavefunction scheme will describe a certain series of filling factors  $\nu$  and states close to these, which are seen as trial wave functions for excitations of the incompressible liquid. A gap then implies that there is a finite difference between the ground state and all excitations, also in the thermodynamic limit. Usually the trial states indicate that different plateaus have distinct topological orders.

Tests of the wavefunctions include prediction of gaps at the correct filling factors and comparison to experimental measurements and other numerical and analytical models. In addition they have predicted novel properties of the systems, e.g. fractional quasiparticle charges and both abelian and nonabelian anyonic particle interchange statistics. Some of these have been confirmed in experiment while others are still being examined.

### Projections

Trial wavefunctions are necessarily simplifications. As long as they are close to the true wavefunction of the system, for example by being in the same universality class and thus adiabatically connected to it, this can be a strength; as it simplifies analysis and extraction of quantities of interest. The analysis of many prominent wavefunctions is still complicated, however, and usually requires numerical calculations. Even with modern computers there are often significant limits to the investigations of the more involved systems.

One common feature that complicates scrutiny of trial states is that of lowest Landau level projection. It often arises as physical arguments and intuition suggest a wavefunction that has desirable properties but unphysical components in higher Landau levels. The existing technical implementations of this projection are complicated, however, making the study of some wavefunctions limited to small systems or even outright intractable.

This is usually amended by utilising approximative projections. In this work we apply one such to as of yet untested systems, namely the Jain-Kamilla projection for reverse flux composite fermions (see sections 3.3 and 5.1.2) [17–20]. Its application is expedited by a new algorithm, also described in ref. [21]. Secondly we introduce an entirely new procedure that incorporates exact diagonalisation to construct a controlled and remarkably general approximation (see section 5.1.3), presented in ref. [22]. This paper is a collaboration with Fremling, Moran and Slingerland, in which the present author's

contributions include all of the analysis in the spherical geometry.

These techniques are then used to study systems and wavefunctions that have been previously inaccessible. An example of the latter are wavefunctions termed modified states (section 5.5), following an idea by Girvin and Jach [23].

### Pair correlation functions

The pair correlation function  $g$  contains a lot of information about multi particle systems. It gives the probability density of finding two particles depending on their relative distance, and thus describes both short range and long range correlations. Pair correlations are often utilised in the study of the quantum Hall effect to compare and elucidate properties of trial wavefunctions and exact energy eigenstates. They are also instrumental in computing a model of neutral excited states called the single mode approximation [24], which can give estimates for the gap.

However the information contained in  $g$  is usually presented only in graphical plots, making reproduction or quantitative comparison difficult. In order to express the pair correlation function concisely it can be expanded in a suitable basis.

In section 6.1 it is argued that the existing expansions have some numerically undesirable properties, and in light of this a new basis is constructed. This is then used to find pair correlations of various systems extrapolated to the thermodynamic limit, revealing properties of the macroscopic systems.

### Software

The results in this work were acquired through extensive numerical computations performed using specialised programs. Three main collections of software were utilised:

- **Monte Carlo computations on the sphere** were performed using software written by the present author and available at [https://bitbucket.org/jfulse/fqhe\\_mc\\_sphere.git](https://bitbucket.org/jfulse/fqhe_mc_sphere.git) and <http://www.thphys.nuim.ie/hammer/>. This includes optimised tools for generation and analysis of MC data for a variety of trial wavefunctions, including ground states and general excited states of the following wavefunctions: Laughlin, composite fermions in both flux directions, Moore-Read and Bonderson-Slingerland.

- **Most exact diagonalisation calculations** were done utilising the software “Hammer” developed by Niall Moran and available for free at <http://www.thphys.nuim.ie/hammer/>. In addition to programs performing diagonalisation of the sphere and the torus it also includes tools for Monte-Carlo computations of hierarchical states on the torus, the latter written by Mikael Fremling and partly by the present author.
- **Early diagonalisation computations** and some additional calculations, including generation of pseudopotentials and computation of pair correlation functions from energy eigenstates, were performed using the DiagHam package: <http://nick-ux.lpa.ens.fr/diagham/wiki>. This is a freely available set of utilities for performing calculations on FQHE systems.

### Chapter outline

Following is a summary of the chapter contents:

- (2) Summary of relevant background theory used in subsequent chapters.
- (3) Review of some common FQHE trial wavefunctions that are investigated in later sections, either in their original or modified forms.
- (4) Description of the numerical methods employed in the analysis, consisting of exact diagonalisation and Monte-Carlo calculations.
- (5) Results from the new projection techniques used on existing and modified trial wavefunctions. These are used to assess the effectiveness of existing and new projection schemes, and of the wavefunctions themselves by comparison to results from diagonalisation. Excited states of the Bonderson-Slingerland wavefunction are studied for the first time.
- (6) Description of the new pair correlation decomposition basis and results facilitated by it, including scaling of the pair correlations to the thermodynamic limit.
- (7) Summary of the preceding results and suggestions for further research.

# Chapter 2

## Relevant background

### 2.1 The Hamiltonian

The Hamiltonian  $H$  is fundamental to nonrelativistic quantum mechanics and essential in much of the following material. This section motivates the choice of  $H$  used in the remainder and discusses some of its properties.

#### 2.1.1 The single particle case

The Hamiltonian of a charged particle in a classical magnetic field is

$$H_1 = \frac{1}{2m_b} \left( \hat{\mathbf{p}} + \frac{e}{c} \mathbf{A} \right)^2 + H_Z, \quad (2.1)$$

where  $m_b$  is the band mass resulting from the periodic ion lattice,  $e$  is the electron charge and  $\mathbf{A}$  is the vector potential.

The Zeeman term  $H_Z$  gives the spin coupling. The quantum Hall effect occurs in a strong magnetic field, and as such the Zeeman energy can be comparable to both the disorder potential and the interaction energy; the relevant energy scales for the fractional effect (see the discussion in 2.1.2). It is often the case, however, that the state in question is completely polarised, so that the Zeeman energy is a constant and can therefore be ignored. This is assumed in the remainder of this work (non-polarised trial wavefunctions exist in the literature but are not considered here).

The operator  $\hat{\mathbf{p}} = -i\hbar\nabla$  is the canonical, gauge invariant momentum; one can also define a kinetic momentum  $\hat{\boldsymbol{\pi}} = \hat{\mathbf{p}} + \frac{e}{c}\mathbf{A}$ .  $H_1$  can be expressed in

## 2.1. THE HAMILTONIAN

terms of ladder operators (from here on assuming two dimensions):

$$\begin{aligned} a^\dagger &= \frac{\ell}{\sqrt{2}}(\hat{\pi}_x + i\hat{\pi}_y) \\ H_1 &= \frac{1}{2m_b}\hat{\pi}^2 = \frac{1}{2}\hbar\omega_c(aa^\dagger + a^\dagger a) , \end{aligned} \quad (2.2)$$

where a length scale and an energy scale are introduced in terms of the magnetic length  $\ell = \sqrt{\hbar c/eB}$  and the cyclotron frequency  $\omega_c = eB/m_b c$  respectively.  $B$  is the magnitude of the magnetic field piercing the system. Assuming for the moment a flat geometry with the magnetic field pointing in the  $z$ -direction, i.e.  $\mathbf{B} \parallel \mathbf{e}_z$ , we have  $B = |\nabla \times \mathbf{A}| = \partial_x A_y - \partial_y A_x$ . This gives the following commutation relations for the ladder operators:

$$\begin{aligned} [a, a^\dagger] &= \frac{\ell^2}{2\hbar^2}[\hat{\pi}_x + i\hat{\pi}_y, \hat{\pi}_x - i\hat{\pi}_y] \\ &= \frac{1}{B}([\partial_x, A_y] - [\partial_y, A_x]) = \frac{\partial_x A_y - \partial_y A_x}{B} = 1 . \end{aligned} \quad (2.3)$$

The same holds for other geometries. This familiar commutation relation implies that  $H_1$  is formally identical to the Hamiltonian for a harmonic oscillator, yielding the energy levels

$$E_n = \hbar\omega_c \left( n + \frac{1}{2} \right). \quad (2.4)$$

In this context these are called Landau levels, and this work will be referring to  $E_0$  as the lowest Landau level (LLL),  $E_1$  as the second Landau level (SLL) and so on.

It can be demonstrated that the operator  $\hat{\mathbf{r}}_0 = \mathbf{r} + \ell^2 \mathbf{e}_z \times \hat{\boldsymbol{\pi}}/\hbar$  commutes with the Hamiltonian and that  $\hat{\mathbf{r}}_0$  and  $\hat{\boldsymbol{\pi}}$  together describe classical cyclotron motion through Heisenberg's equations of motion. Thus  $\hat{\mathbf{r}}_0 = (x_0, y_0)$  is a constant of motion and a quantum analogue to the classical guiding center [25]. It gives rise to another set of ladder operators  $b^\dagger = (x_0 - iy_0)/\sqrt{2}\ell$ , again with  $[b, b^\dagger] = 1$ . These commute with  $a^\dagger$  and  $a$ , which means that  $b^\dagger$  and  $b$  cycle through degenerate single particle states within a given Landau level  $E_n$ .

When investigating particular gauges and geometries in section 2.2 it will be apparent that this degeneracy is huge, as also mentioned in the exposition of the QHE in section 1.1. For this reason it is meaningful to talk about systems residing only in the lowest or second Landau level, and systems with e.g.  $\nu < 1$  and  $\nu < 3$  are accessible in experiment.

The expression for  $\omega_c$  shows that the gap between single particle energy

levels is proportional to the magnetic field  $B$ . For the quantum Hall effect to occur this must be strong, leading to a large gap. Therefore an approximation is usually adapted in which the multiparticle system consists of polarised electrons residing in the lowest available Landau level.

This means that if the filling factor  $\nu$  is less than one the electrons are all in the LLL with the spin aligned opposite to the external field, if  $\nu$  is less than two but greater than one they are in the LLL occupying both spin directions (assuming  $\hbar\omega$  is stronger than the Zeeman energy), if  $\nu$  is less than three they are all in the LLL or SLL, et cetera. In addition it is a common approximation to have only one LL - spin combination partially filled, with the exception of studies explicitly investigating polarisation or Landau level mixing.

### 2.1.2 The many particle case

The many particle Hamiltonian can be expressed as

$$H = \sum_i H_1(\mathbf{r}_i) + \sum_{i<j} V(|\mathbf{r}_j - \mathbf{r}_i|) + \sum_i U(\mathbf{r}_i), \quad (2.5)$$

with the single particle Hamiltonian  $H_1$  discussed in the previous section, the interparticle potential  $V$  (assumed to be central), and a disorder potential  $U$ . It was argued above that the electrons can be approximated as fixed in a given Landau level. This means that the first term of (2.5) is a constant that can be ignored; this is often described as freezing out of the kinetic energy.

In experimental situations the periodic background potential from the positive ions has a period much smaller than the size of an electron wavepacket (see ref. [3] chapter 3); it will therefore be ignored beyond substituting the electron vacuum mass for the band mass in (2.1). An exception to this is when scaling interaction energy densities to the thermodynamic limit, where the background energy is modelled as a constant and included to obtain a well defined limit (see section 5.2.1).

According to the account in section 1.1 disorder is crucial for the occurrence of the quantum Hall effect and as such can not be neglected. However it was also pointed out that the main problem of the FQHE is explaining the existence of mobility gaps, and thus incompressibility, between integer fillings  $\nu \in \mathbb{N}$ . The plateaus in transverse resistance and vanishing of longitudinal resistance can be understood if one can infer incompressibility without the disorder potential  $U$ .

Thus the most common model of the fractional quantum Hall effect, used

in the remainder of this work, is a Hamiltonian consisting of the interparticle potential alone. This is usually taken to be the Coulomb interaction:

$$H = \sum_{i < j} V(|\mathbf{r}_j - \mathbf{r}_i|) = \sum_{i < j} \frac{e^2}{\epsilon |\mathbf{r}_j - \mathbf{r}_i|}, \quad (2.6)$$

with the dielectric constant  $\epsilon$ . Exceptions to this form are effective interactions, which are sometimes utilised for instance to model the effects of finite width of the system, or to simulate second Landau level dynamics using lowest Landau level wavefunctions (these examples are still two body potentials).

A common strategy in quantum mechanics consists of solving the free system, which often is feasible, and treating the more complicated interactions as perturbations. However this approach is ruled out for the fractional quantum Hall effect as the relevant Hamiltonian (2.6) consists of the interaction term exclusively (another famous example where this is impractical is quantum chromodynamics, where the interactions are too strong to be modelled as perturbations except at very high energies). This means that treatment of the model is more challenging and other methods must be brought to bear. But it also hints at why the system is so interesting in the first place, as the strongly interacting electron liquid forms exotic states of matter.

Much of this thesis is focused on the study of variational trial wavefunctions, often using comparison between results from these and exact results from solving the Hamiltonian (2.6) as an important benchmark. In this the latter is taken as the more realistic model of the physical system; however it should be kept in mind that this Hamiltonian is in itself an approximation to the physical one, which in particular will vary with the experimental setup.

### Pseudopotentials

Following Haldane [26] the Hamiltonian in (2.6) can be conveniently parametrised in terms of pseudopotentials  $V_L$  (this review based on ref. [27]). Since  $H$  is a two body potential it is sufficient to concentrate on two particle wavefunctions through the decomposition  $\Psi(\mathbf{r}_1, \dots, \mathbf{r}_{N_e}) = \sum_k \psi_k(\mathbf{r}_1, \mathbf{r}_2) \phi_k(\mathbf{r}_3, \dots, \mathbf{r}_{N_e})$ . This is followed by a further decomposition into center of mass and relative parts:

$$\psi(\mathbf{r}_i, \mathbf{r}_j) = \sum_{rs} A_{rs} \psi_r^{CM} \left( \frac{\mathbf{r}_i + \mathbf{r}_j}{2} \right) \psi_s^{rel}(\mathbf{r}_j - \mathbf{r}_i). \quad (2.7)$$

The Hamiltonian acts only on the relative part, for which a basis can be constructed as  $|L; i, j\rangle$  where  $L$  is the relative angular momentum between

particle  $i$  and  $j$ . This is assuming the relative angular momentum operator commutes with the Hamiltonian, which is true in particular for the disk and sphere geometries widely used in describing the FQHE (on the torus the symmetry is less pronounced and two parameters are necessary; yielding pseudopotentials  $V_{km}$  [28]). Being a complete set, the basis can be used to rewrite  $H$  as

$$H = \sum_{i < j} \sum_{LL'} |L; i, j\rangle \langle L; i, j| V |L'; i, j\rangle \langle L'; i, j| = \sum_{i < j} \sum_L V_L \mathcal{P}_L, \quad (2.8)$$

where rotational invariance of  $V$  has been assumed to require  $L = L'$  and  $\mathcal{P}_L$  projects onto angular momentum  $L$ . Having identical particles means that the pseudopotentials  $V_L = \langle L; i, j| V |L; i, j\rangle$  are independent of the indices  $i$  and  $j$ , yielding a compact representation of any potential observing the above assumptions. Note that only pseudopotentials with odd  $L$  are relevant for fermions, while the same is true with even  $L$  for bosons. This is because the basis functions  $|L; i, j\rangle$  are antisymmetric and symmetric for odd and even  $L$  respectively.

Since a lower relative angular momentum corresponds to a higher probability of the particles being closer together, the pseudopotentials also give an intuitive picture of the given interaction. The particles will avoid being at the typical distances associated with the largest pseudopotentials; or from another point of view  $V_L$  is the energy cost of having two particles with relative angular momentum  $L$ . With this in mind it is straightforward to construct effective interactions. A common one called the hardcore potential sets  $V_1 = 1$  and the rest  $V_{L>1} = 0$  (the corresponding bosonic version sets  $V_0 = 1$ ).

Returning to the quantum Hall effect, closed expressions have been found for  $V_L$  in general Landau levels for the most common geometries (see ref. [29] for the sphere). This often allows a straightforward adaption of a model from one Landau level to another, most commonly used from the LLL to the SLL.

## 2.2 Geometry and single particle wavefunctions

Although the classic experimental setup is rectangular, different spatial geometries have been used to elucidate different features of the quantum Hall effect. Below is a review of the most common ones and their single particle wavefunctions, with special attention to the spherical one due to its importance in the remainder.

### 2.2.1 The slab and the disk

The most natural geometry to describe experiments is a rectangular slab, here in a coordinate system with the external voltage at the boundaries in the  $y$ -direction, giving rise to a current along the same. An infinitely long slab with no disorder has a symmetry in the  $x$ -direction, which is preserved in the Landau gauge vector potential  $\mathbf{A} = By\mathbf{e}_x$ , leading to the Hamiltonian

$$\hat{H} = \frac{1}{2m_b}(\hat{p} - eA)^2 = \frac{1}{2}\hbar\omega_c \left[ (y/\ell - \ell k_x)^2 + \frac{\hat{p}_y^2 \ell^2}{\hbar} \right]. \quad (2.9)$$

The symmetry means that  $\hat{p}_x$  is conserved and can be replaced by its eigenvalue  $k_x$ , reducing (2.9) to a one dimensional shifted harmonic oscillator in  $y' = y/\ell - \ell k_x$  with the Landau energy levels  $E_n$  in 2.4. The fact that there is no dependence on  $k_x$  means that the energy levels are massively degenerate, with a degeneracy depending on the surface area through the number of states one can fit with  $y'(\ell k_x)$ .

The energy eigenstates are plane waves along  $x$  with a harmonic oscillator centered at  $y'$ :

$$\psi_{n,k_x} = \left( \frac{1}{\pi 2^{2n} (n!)^2} \right)^{\frac{1}{4}} e^{ik_x x} \exp\left(-\frac{1}{2}y'^2\right) H_n(y'), \quad (2.10)$$

where  $H_n$  are the Hermite polynomials. These are delocalised along  $x$  and localised around  $\ell k_x$  along  $y$ ; showing a connection between  $x$ -momentum and  $y$ -position. From here on natural units are adopted unless otherwise noted:

$$\hbar\omega_c = \ell = 1. \quad (2.11)$$

Another gauge useful for the form it gives the wavefunctions and for its utility with the simple circular disk geometry is the symmetric gauge:

$$\mathbf{A} = \frac{1}{2}\mathbf{B} \times \mathbf{r}. \quad (2.12)$$

The resulting Hamiltonian has the energy eigenfunctions

$$\psi_{nm} = (-1)^n \sqrt{\frac{n!}{\pi 2^{m+1} (n+m)!}} z^m L_n^m(|z|^2/2) e^{-\frac{|z|^2}{4}} \quad (2.13)$$

with the complex coordinate  $z = x + iy$ , associated Laguerre polynomials  $L_n^m(z)$  and an angular momentum quantum number  $m \in \{-n, -n+1, \dots\}$ .

Physical observables are gauge independent, and  $\psi_{mn}$  has the same Landau energy eigenvalues  $E_n$ . The Laguerre polynomials can be expressed in a series representation as [30]

$$L_n^m(z) = \sum_{k=0}^n \frac{(-1)^k (n+m)!}{(n-k)!(m+k)!k!} z^k . \quad (2.14)$$

The functions in (2.13) are symmetric along concentric circles, and from  $L_n^m(z) = \pm z^n/n! + \mathcal{O}(z^{n-1})$  one may estimate their extent through the expectation value of the squared radius  $r^2 = |z|^2$ :

$$\sqrt{\langle r^2 \rangle} \approx \sqrt{m+2n+1} . \quad (2.15)$$

Reintroducing the magnetic length  $\ell$ , this means that in a single Landau level one can fit approximately  $N$  states in an area  $A = 2\pi\langle r^2 \rangle = 2\pi\ell^2(N+n)$ , or in other words that the Landau level degeneracy per unit area is

$$d \sim 2\pi\ell^2 = N_\Phi , \quad (2.16)$$

which is a huge number in macroscopic systems. A magnetic field around  $B \sim 10$  T as in the experiment in fig. 1.1 corresponds to  $N_\Phi \sim 10^{15}$ .

Section 2.1.1 argues that in describing quantum Hall systems with  $\nu \leq 1$ , and sometimes also  $\nu > 1$  using effective Hamiltonians, the many body wavefunction can be approximated as a superposition of LLL single particle wavefunctions. Using  $L_0^m = 1$  with (2.13) shows that these in turn are superpositions of near holomorphic wavefunctions

$$\psi(z, z^*) = \sum_k c_k z^m e^{-\frac{|z|^2}{4}} = f(z) e^{-\frac{|z|^2}{4}} , \quad (2.17)$$

i.e. all dependence on  $z^*$  is in the Gaussian factor. This is fortituous as the analysis of holomorphic functions can be brought to bear, and a function space where the Gaussian is part of the integral measure is sometimes used so as to deal with holomorphic functions exclusively.

The many particle state consisting of a completely filled lowest Landau level, i.e.  $\nu = 1$  and  $N_e = N_\Phi - 1$ , has a particularly simple form. It can be demonstrated that filling a Slater determinant with the states  $\psi_{0m}$  in (2.13) gives the result

$$\Psi_{\nu=1} = \prod_{i<j} (z_i - z_j) e^{-\frac{1}{4} \sum_i |z_i|^2} . \quad (2.18)$$

The polynomial part of this expression appears as a factor in many trial wavefunctions.

When presented with a many body wavefunction  $\Psi$  in the lowest Landau level its filling factor can be identified through the highest power  $p_{max}$  of a single coordinate. The function  $\Psi$  will be a superposition of single particle wavefunctions  $\psi_{0m} \sim z^m$  (2.13), of which the one with the largest extent is somewhat loosely defined as the edge of the disk. This is also the one with the highest power, and with (2.15) and the comments below in mind this means that the number of available states inside the boundary, and thus the number of flux quanta piercing the sample is

$$N_{\Phi} \approx p_{max} . \quad (2.19)$$

This is then used to find the filling factor  $\nu = N_e/N_{\Phi}$ .

### 2.2.2 The sphere

Placing the system on a sphere has the advantage that there are no boundaries while the single particle wavefunctions stay relatively simple. Because of this all the calculations in later sections are done on this geometry, first introduced in ref. [26]. The electrons are located on a spherical shell, naturally described in the regular spherical coordinate system with radius, polar angle and azimuthal angle  $(R, \theta, \phi)$ . The radius of the sphere  $R$  is given in terms of  $\ell$  and assumed constant. There are two gauges typically used in the literature, the Wu-Yang gauge  $\mathbf{A}_{WY}$  [31] and the spinor gauge  $\mathbf{A}_S$ :

$$\begin{aligned} \mathbf{A}_{WY} &= -\frac{N_{\Phi}}{2eR} \left( \cot \theta + \frac{1}{\sin \theta} \right) \mathbf{e}_{\phi} \\ \mathbf{A}_S &= -\frac{N_{\Phi}}{2eR} \cot \theta \mathbf{e}_{\phi} . \end{aligned} \quad (2.20)$$

The latter are more convenient when utilising the spinor coordinates introduced below, and will be used throughout this work.

The field  $\mathbf{B}$  is uniform and points radially outwards, arising from a Dirac monopole in the center of the sphere. It can be shown that  $N_{\Phi}$ , the number of magnetic flux quanta piercing the surface, must be an integer so that the singularity associated with the monopole has no observable effect. It is convenient to define the quantity  $Q \in \{\frac{1}{2}, 1, \frac{3}{2}, 2, \dots\}$  through

$$N_{\Phi} = 2Q . \quad (2.21)$$

## 2.2. GEOMETRY AND SINGLE PARTICLE WAVEFUNCTIONS

Considering the flux through the surface shows that  $R = \sqrt{Q}$ . One may fix  $R$  since it commutes with the Coulomb Hamiltonian

$$\widehat{H} = \frac{\hbar}{2mR^2} |\widehat{\Lambda}|^2, \quad (2.22)$$

with the tangential momentum operator

$$\widehat{\Lambda} = \mathbf{R} \times \left( -i\nabla + \frac{e}{\hbar c} \mathbf{A}(R) \right). \quad (2.23)$$

Inspecting the commutation relations leads to the total angular momentum and its  $z$ -component

$$\begin{aligned} \widehat{\mathbf{L}} &= \widehat{\Lambda} + Q \frac{\mathbf{R}}{R} \\ \widehat{L}_z &= -i\partial_\phi. \end{aligned} \quad (2.24)$$

In the remainder  $R$  is usually left out of the expressions.

It can be demonstrated that  $\{H, L^2, L_z\}$  is a commuting set, and simultaneous eigenfunctions can be found as

$$\phi_{nm}^Q = \mathcal{N}_{Qnm} (-1)^{Q+n-m} u^{Q+m} v^{Q-m} \sum_{s=0}^n (-1)^s \binom{n}{s} \binom{2Q+n}{Q+m+s} |u|^{2s} |v|^{2n-2s}, \quad (2.25)$$

comprising the spherical single particle wavefunctions. The above introduces the spinor coordinates

$$u = \cos\left(\frac{\theta}{2}\right) e^{i\frac{\phi}{2}} \quad \text{and} \quad v = \sin\left(\frac{\theta}{2}\right) e^{-i\frac{\phi}{2}} \quad (2.26)$$

and the normalisation

$$\mathcal{N}_{Qnm} = \sqrt{\frac{2Q+2n+1}{4\pi} \frac{(Q+n+m)!(Q+n-m)!}{n!(2Q+m)!}}. \quad (2.27)$$

Again  $n$  indexes the energy Landau levels  $E_n = (n+1/2)\hbar\omega_c$ , connected to the  $L^2$  angular momentum eigenvalues through  $n = l - Q$ . Thus the angular momentum has a minimum value:  $l \in \{Q, Q+1, \dots\}$ . The eigenstate relations are

$$\begin{aligned} \widehat{L}^2 \phi_{nm} &= l(l+1) \phi_{nm} \\ \widehat{L}_z \phi_{nm} &= m \phi_{nm}. \end{aligned} \quad (2.28)$$

## 2.2. GEOMETRY AND SINGLE PARTICLE WAVEFUNCTIONS

The  $z$ -component quantum number takes values  $m \in \{-l, -l+1, \dots, l\}$ . This means that the number of states in Landau level  $n$  are

$$d(n) = 2(n + Q) + 1 . \quad (2.29)$$

For multiparticle eigenstates  $\Psi$  the total angular momentum quantum numbers are denoted by  $L$  and  $M$ :

$$\begin{aligned} \widehat{L}^2 \Psi(z_1, \dots, z_{N_e}) &= L(L + 1) \Psi(z_1, \dots, z_{N_e}) \\ \widehat{L}_z \Psi(z_1, \dots, z_{N_e}) &= M \Psi(z_1, \dots, z_{N_e}) . \end{aligned} \quad (2.30)$$

The notation above is slightly awkward, but will hopefully be clear from the context.

From (2.25) it is evident that, similarly to the disk, the lowest Landau level wavefunctions are holomorphic in  $(u, v)$ . As in (2.18) in the previous section the unnormalised  $\nu = 1$  Slater determinant wavefunctions can be found as

$$\Psi_{\nu=1} = \prod_{i < j} (u_i v_j - u_j v_i) . \quad (2.31)$$

Another coordinate system sometimes used on the sphere is that of the stereographic coordinate  $z = x + iy$ . A line is extended from a chosen pole to the particle, and  $z$  is where the line intersects a plane through the equator. This plane is taken to be the complex plane. Choosing the south pole leads to  $z = \tan(\theta/2) \exp(i\phi) = v/u$ . The north pole is mapped to the origin and the south pole to infinity. In terms of stereographic coordinates the  $\nu = 1$  wavefunction in the Wu-Yang gauge is

$$\Psi_{\nu=1} \prod_{i < j} (z_i - z_j) \prod_i (1 - |z_i|^2)^{-Q} , \quad (2.32)$$

In the spinor gauge there is an extra factor  $\prod_j \exp(i\phi_j)$ ; for convenience the Wu-Yang gauge is usually employed when working in stereographic coordinates.

The function in (2.32) is formally the same as (2.18) on the disk, up to the last factor in both. In fact, in the limit of infinite radius, where the sphere becomes a plane, they become equal. Owing to the ubiquitousness of these geometric factors multiplying the holomorphic polynomials of the LLL single particle wavefunctions, they are omitted in the remainder. Wavefunctions are generally presented in terms of  $z_i$ , which then stands for either complex

## 2.2. GEOMETRY AND SINGLE PARTICLE WAVEFUNCTIONS

coordinates on the disk without the geometric factor, spinor coordinates on the sphere with the substitution  $(z_i - z_j) \rightarrow (u_i v_j - u_j v_i)$ , in the spinor gauge, or stereographic coordinates on the sphere in the Wu-Yang gauge and omitting the geometric factor.

There are two natural distance measures on the sphere. Evaluating the distance from the north pole they are the arc length  $r_a = R\theta$ , which follows the curvature of the surface, and the chord length  $r_c = 2R \sin(\theta/2)$ , which draws a line through the three-dimensional embedding space. While the former might seem more physical, the latter is mostly used in the literature and simplifies most expressions. In particular, it makes the connection between common trial wavefunctions and distance between particles more clear. In the limit of an infinite system they become the same two dimensional Cartesian distance.

Chord length is used throughout this work and the subscript is dropped:  $r \equiv r_c$ . The distance between two particles can then be expressed as

$$r_{12} = 2R|u_1 v_2 - u_2 v_1| . \quad (2.33)$$

It is convenient to also define a dimensionless distance  $\eta \in [0, 1]$ :

$$\eta_{12} = \frac{r_{12}}{2R} = |u_1 v_2 - u_2 v_1| . \quad (2.34)$$

The sphere has a well defined surface area, in contrast with the disk. There is no analogue to the disk wavefunctions extending outside the region designated as the system boundary as in the end of section 2.2.1. The corresponding derivation of filling factor  $\nu$  from highest power of a coordinate using (2.19) therefore becomes rigorous on the sphere:

$$N_\Phi = p_{max} . \quad (2.35)$$

Most trial wavefunctions, however, do not match exactly the filling factor they are intended to describe when using this formula. It is said that they have a shift  $S$ , defined by

$$N_\Phi = \nu^{-1} N_e - S . \quad (2.36)$$

It turns out that  $S$  is not only an artifact of the trial wavefunctions, but constitutes a physically relevant quantity that describes the system's response to the curvature of the configuration space. It emerges also in flat geometries through its conjectured connection to the Hall viscosity [32], given as  $\eta^H = Sn/4$  with electron density  $n$  [33]. This has been confirmed numerically for

the Laughlin, Moore-Read and hierarchical  $\nu = 2/5$  wavefunctions on the torus [33, 34]. The fact that  $\eta^H$  can potentially be computed directly from the Hamiltonian means that  $S$  is another quantity useful in comparing trial wavefunctions.

### 2.2.3 The torus

The flat torus is a rhombus with opposite sides indentified, i.e. with periodic boundary conditions. It has the same topology and global geometry as the geometrical torus or donut shape. It was first introduced in the context of the FQHE in ref. [35], and is useful for having no boundaries and no curvature, and the access to a geometric parameter  $\tau$  which facilitates computation of the Hall viscosity.

The toroidal single particle wavefunctions are infinite linear combinations of Landau gauge functions (2.10) and complicated in general. Many of them can be adopted from the corresponding disk or sphere versions by changing  $(z_i - z_j) \rightarrow \theta((z_1 - z_2)/L|\tau)$  and adding a center of mass factor, where  $L$  and  $\tau$  parametrise the torus geometry ( $\tau = i$  corresponds to rectangular tori). The antisymmetric  $\theta$ -functions are quasiperiodic in two directions [36]. However the center of mass factor can in general be challenging to construct.

Ref. [22] introduces a new LLL projection technique and demonstrates that it is viable both on the sphere and torus geometries. The material concerning the sphere is presented in section 5.1.3. The analysis on the torus, however, was mostly done by the other authors and is excluded here. In light of this a more in-depth introduction to toroidal wavefunctions is deemed unnecessary.

### 2.2.4 The second Landau level

When describing states in partially filled higher Landau levels, it is common to approximate both spin directions of the levels below the topmost as completely filled and inert (unless specifically investigating LL mixing etc). An analogy may then be used in which the topmost level is modelled using states from the lowest Landau level. This is helpful because the single particle wavefunctions in the LLL have a simpler form, as seen in sections 2.2.1 and 2.2.2, and because doing so means that most of the methods that exist for dealing with the lowest Landau level can be transferred almost directly.

In particular this applies to states with filling factors  $2 < \nu < 3$ , i.e. in the second Landau level and with spin up. This region of fillings is especially

### 2.3. PAIR CORRELATION FUNCTIONS

interesting: firstly, unlike in the lowest Landau level (possibly except for under special circumstances [14,37,38]), even denominator states have been observed. Secondly, several models predict that some plateaus contain nonabelian quasiparticles (see sections 3.1.2 and 3.4.2).

When performing exact diagonalisations (section 4.1) in the SLL it is common to utilise LLL single particle wavefunctions but to exchange the LLL pseudopotentials for SLL ones. This is reasonable because the levels are isomorphic apart from the pseudopotential values, and in particular the actual wavefunctions are not used when diagonalising in momentum space. The only caveat is the size of the Landau levels on the sphere, where each level has two more states than the one below, as seen in (2.29). To compensate for this, when diagonalising a system in the second Landau level at physical flux  $N_\Phi$ , lowest Landau level wavefunctions are used with the SLL pseudopotentials evaluated at flux  $N_\Phi - 2$ .

When it comes to quantities like overlap between states, with no explicit dependence on the flux, this gives good results as is. The Coulomb energy, however, depends on the flux through the radius  $R$  of the sphere:  $E \propto R^{-1} = N_\Phi^{-1/2}$ . Thus when using eigenvalues in the second Landau level obtained using the method above, this is compensated for by the following correction:

$$E \rightarrow \sqrt{\frac{N_\Phi - 2}{N_\Phi}} E . \quad (2.37)$$

Lowest Landau level wavefunctions, with their holomorphic properties, are used rather than the corresponding SLL functions. Also in this case a correction is usually applied to acquire more accurate values for the energy. Rather than using the Coulomb interaction (2.6) an effective potential is utilised, whose pseudopotentials computed in the LLL basis are equal to those of the Coulomb interaction pseudopotentials in the SLL basis [39,40].

## 2.3 Pair correlation functions

A useful quantity in describing many-particle states is the pair correlation function  $\rho_2(\mathbf{r}_1, \mathbf{r}_2)$ , giving the probability density for finding one particle at  $\mathbf{r}_1$  and another at  $\mathbf{r}_2$ . It is defined as

$$\rho_2(\mathbf{r}_1, \mathbf{r}_2) = \frac{N_e(N_e - 1)}{\rho^2} \int \prod_{i>2} dS_i |\Psi(\mathbf{r}_1, \dots, \mathbf{r}_N)|^2 , \quad (2.38)$$

### 2.3. PAIR CORRELATION FUNCTIONS

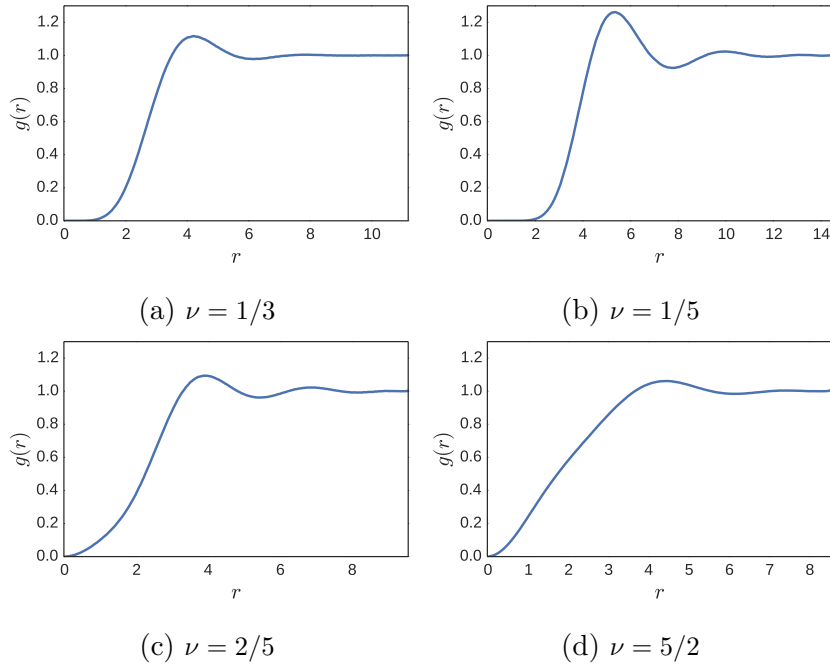


Figure 2.1: Pair correlation functions computed using Monte Carlo. The trial wavefunctions are (a) Laughlin at  $\nu = 1/3$  and  $N_e = 22$  particles, (b) Laughlin at  $\nu = 1/5$  and  $N_e = 22$ , (c) Composite fermions at  $\nu = 2/5$  and  $N_e = 20$  and (d) Moore-Read at  $\nu = 5/2$  and  $N_e = 20$ .

where it is assumed that  $|\Psi|$  is symmetric in particle interchange and that the density expectation value  $\rho$  is constant in space. As long as one is working on the sphere this is reasonable. Dividing by the density squared ensures that (2.38) is normalised to one when the two particles are uncorrelated; this makes the asymptote identical for different filling factors but means that  $\rho_2$  is not strictly speaking a probability amplitude.

The physics of many states considered in the remainder is symmetric in rotations of the sphere (with exceptions for some excitations), and therefore the pair correlation must be as well. In other words  $\rho_2$  should only depend on the length of the relative distance  $\mathbf{r}_{12} \equiv \mathbf{r}_2 - \mathbf{r}_1$ , yielding as a natural measure the quantity

$$g(r_{12}) = \frac{N_e(N_e - 1)}{A\rho^2} \int \prod_{i>1} dS_i |\Psi(\mathbf{r}_2 - \mathbf{r}_{12}, \mathbf{r}_2, \dots, \mathbf{r}_N)|^2, \quad (2.39)$$

where  $A$  is the surface of the sphere. In the remainder this is what is referred to as the pair correlation function. Some examples of  $g(r)$  for different trial wavefunctions are shown in figure 2.1

Much information can be gained from the pair correlation. Fermionicity requires  $g \rightarrow 0$  as  $r \rightarrow 0$ , but the size and shape of the correlation hole at the origin varies. In particular some states characterised by pairing will

### 2.3. PAIR CORRELATION FUNCTIONS

have a shoulder in the slope after the hole (see figure 2.1d for an example). Furthermore there is often oscillation after the maximum, signalling the onset of crystallisation as  $\nu$  decreases: contrast  $\nu = 1/3$  in figure 2.1a with  $\nu = 1/5$  in figure 2.1b. Finally, incompressibility implies suppressed long range correlations. This means that one should expect  $g \rightarrow 1$  within a moderate distance scale, independent of system size, for FQHE ground states.

Apart from being interesting in its own right the pair correlation can be used to compute the energy gap in the single mode approximation [24]. This is an approach in which the lowest energy band of neutral excitations can be estimated using only the ground state wavefunction  $\Psi$ . The excitation with momentum  $\mathbf{k}$  is modelled as a density wave modulation of  $\Psi$  projected to the lowest Landau level:

$$\Phi_{\mathbf{k}} = \mathcal{P}_{LLL} \sum_{j=1}^{N_e} e^{-i\mathbf{k}\cdot\mathbf{r}_j} \Psi . \quad (2.40)$$

This in turn yields an expression for the variational energy that can be calculated using  $g(r)$ .

# Chapter 3

## Review of trial wavefunctions

The main bulk of this work focuses on fractional quantum Hall effect trial wavefunctions. A number of schemes for generation of such have been proposed, some of which are discussed in this chapter.

### 3.1 Ground states and excitations

The first thing one expects from a trial wavefunction procedure is a description of the ground state, i.e. the lowest energy state of the electron system at an exact QHE plateau in terms of  $N_e$  and  $N_\Phi$  (bar deviations from the shift on the sphere). It must have the correct universal properties, and other features like the energy can be compared to experiment and other theoretical models.

In addition to this the low energy dynamics are important; described by excited state wavefunctions in the predominant trial schemes. Usually these are realised as quasiparticles, meaning that although the behaviour arises from the electron system as a whole, they are modelled as emergent particles that are often localised in either space or momentum or both.

In order to explain the quantum Hall effect a model should exhibit incompressibility, or in other words predict a gap. This can be tested by comparing the energies of excited state trial wavefunctions to that of the ground state.

#### 3.1.1 Quasiparticles

An excited state can be charged; altering the ratio of the number of electrons to the flux, relative to the ground state. Thus the system deviates from the middle of the FQHE plateau (which we are thinking of as the ground state, although one could argue that these "excited states" are ground states at other fillings). Likewise they can be neutral, meaning that they are on the middle of

the plateau but have a higher energy. These kinds of elementary excitations, when realised as quasiparticles, are labelled quasiholes (for heightened flux), quasielectrons (for lowered flux) or excitons (neutral). Excitons are usually constructed by combining a quasihole and a quasielectron; other states can be described using different combinations.

As seen below some of the proposed quasiparticles have fractional charge. The total system has an integer number of fundamental charges, being composed of electrons in three dimensions. But the emergent quasiparticles can act as independent entities with charge that is a fraction of this – as an example, introducing a flux quantum locally at  $\nu = 1/m$  will create a Laughlin quasihole (section 3.2.2) of charge  $e/m$  in the bulk and its antiparticle on the edge. This has been confirmed in experiment through tunnelling of the edge excitations [41–43]. Even more intriguingly, some quasiparticle states are predicted to have fractional statistical phase; in other words they are anyons.

### 3.1.2 Anyons

In two dimensions the possible multiparticle states are not limited to bosons or fermions: they can also acquire exchange angles  $\theta$  intermediate between 0 and  $\pi$  through interchange. Symbolically,

$$\Psi(\mathbf{r}_2, \mathbf{r}_1) = e^{i\theta} \Psi(\mathbf{r}_1, \mathbf{r}_2) . \quad (3.1)$$

The theoretical possibility of anyons was originally deduced from a configuration space perspective in ref. [44]. Rather than using coordinate symbols with no direct physical meaning and a configuration space which is a cartesian product of single particle spaces, as implied in (3.1), the authors considered the space obtained by taking the single particle space product and then identifying points where identical particles are interchanged. The connectedness of this space depends on the number of spatial dimensions and leads to different possibilities for exchange phases. Another argument notes that a two dimensional space gives the possibility of angular momentum which is not integer or half-integer, again yielding anyonic statistics [45].

The anyonic nature of quasiparticles has not been observed conclusively in experiment but evidence pointing in this direction exists [46, 47]. Some suggested states have nonabelian statistics [48, 49]. This means that braiding of the quasiparticles interchanges distinct states with the particles in the same positions, and the order of braiding matters when there are three or more

quasiparticles.

If realised in nature anyons could supply useful systems for topologically protected qubits in fault tolerant quantum computing, e.g. by encoding the information in nonabelian states. Global braiding operations are thus necessary to alter the qubit states, which then are protected from local noise [50–52]. Different trial wavefunctions predict different species of anyons, and discerning which ones are more likely to describe the physical system is therefore important.

## 3.2 Laughlin and the hierarchy

### 3.2.1 Laughlin

The first to be observed and most prominent of the FQHE filling fractions was  $\nu = 1/3$  [8], another early one was  $1/5$  [10], and a few years later  $1/7$  followed [13]. Laughlin’s wavefunction [53] pertains to these  $\nu = 1/m$  plateaus. His starting point was a trial wavefunction of Jastrow factors:  $\Psi = \prod_{i<j} f(z_i - z_j)$ . Since it should conserve angular momentum and be fermionic  $f(z)$  must be a homogeneous odd polynomial; imposing the correct filling factor and restricting to the lowest Landau level leaves a unique function

$$\Psi_m^L = \prod_{i<j} (z_i - z_j)^m, \quad (3.2)$$

leaving out the geometric Gaussian factors as mentioned in the discussion below equation (2.31). The flux in the system can be found using (2.35):  $N_\Phi = p_{max} = m(N_e - 1)$ . From (2.36) this means that the filling factor is  $\nu = 1/m$  as it should, while the shift on the sphere is  $S = m$ .

This wavefunction matches the exact system to a remarkable degree, as has been demonstrated in extensive numerical studies. Incompressibility can be argued from an upper bound on the gap estimated from the excited state trial wavefunctions in the following section, or from employing what is known as the plasma analogy:

Similarly to the correspondence between quantum theory and statistical mechanics, Laughlin pointed out that  $|\Psi_m^L|^2$  is formally identical to the energy  $E_m$  in the Boltzmann weight  $\exp(-E_m)$  for a two dimensional classical one-component plasma with particle charge to temperature ratio  $m$ . The Gaussian factor, left out in (3.2), yields a homogeneous background charge. The plasma

is known to be screening at parameters corresponding to the fractional quantum Hall effect.

In the Coulomb system a phase transition occurs when  $m \gtrsim 7$ , moving from an incompressible electron liquid to a crystalline state known as a Wigner crystal [54]. A similar transition also takes place for the trial wave function (3.2), but not until  $m \gtrsim 70$ , as can be seen using the plasma analogy and results from the two dimensional plasma [55].

Pseudopotentials (section 2.1.2) offer additional insight into Laughlin's wavefunction  $\Psi_m^L$ . Focusing on a pair of particles  $i$  and  $j$ , the factor  $(z_i - z_j)^m$  shows that they have relative angular momentum exactly equal to  $m$ , and the pseudopotentials  $V_L$  with  $L < m$  do not pick up any contribution to the energy. Thus  $\Psi_m^L$  is the highest density zero energy eigenstate of potentials where  $V_L = 0$  for  $L \geq m$  and  $V_L > 0$  for  $L < m$ ; in particular the  $1/3$  state is a ground state for the hardcore potential ( $V_1 = 1$  and  $V_L = 0$  for  $L > 1$ ).

### 3.2.2 Laughlin quasiparticles

A quasihole occurs when the ratio of flux to electrons is higher than at the plateau; Laughlin achieved this by raising the flux by one while keeping the number of electrons constant. This means that there is one extra single particle state available relative to the ground state that is unused by the electrons (or a superposition of such), so that the highest power of a single coordinate is raised by one. The original suggestion is localised in space:

$$\Psi_{m,qh} = \prod_{i=1}^{N_e} (z_i - z_0) \Psi_m . \quad (3.3)$$

The quasihole is located around  $z_0$ , where the electron density is the lowest.

This excitation has charge  $Q = e/m$  and exchange angle  $\theta = \pi/m$ . An intuitive way to justify this assertion is to imagine creating an extra electron at  $z_0$ ; this would give a factor  $\prod_{i=1}^{N_e} (z_i - z_0)^m$ . Since (3.3) is  $1/m$  of this factor, it is in a way “ $1/m$  missing electrons.” Laughlin deduced the charge more rigorously using the plasma analogy; a calculation of both using the Berry phase is in [56].

A natural guess for a localised quasielectron is the conjugate of the above (since the inverse factor would be singular), however this implies that the wavefunction is no longer limited to the lowest Landau level. Projection to the latter is thus in order. As seen in section 5.1 this projection is given by

$z^* \rightarrow \partial_z$  (with normal ordering), and this is reasonable since we need less flux relative to number of electrons and derivatives will lower the powers of the coordinates. The Laughlin quasielectron is therefore

$$\Psi_{m,qe} = \prod_{i=1}^{N_e} (\partial_{z_i} - z_0) \Psi_m . \quad (3.4)$$

This is more computationally intensive than the quasihole due to the complicated expression arising from the derivatives, and has been shown not to be as good as the quasihole in numerics [57]. Its charge and exchange angle is  $Q = -e/m$  and  $\theta = \pi/m$ .

### 3.2.3 The Haldane-Halperin hierarchy

Shortly after the state at filling  $\nu = 1/3$  was observed other odd denominator plateaus not following the  $\nu = 1/m$  pattern were found as well [9, 11, 12], and an extended trial wavefunction scheme was required to describe these. The hierarchy construction [26, 58] produces wavefunctions for other filling factors by using quasiparticles over the Laughlin wavefunction. Intuitively, once there are enough quasiparticles they condense into their own Laughlin state, being charged particles in similar conditions to the electrons that form the underlying Laughlin fluid. If the quasiparticle coordinates are  $w_k$ , the 1<sup>st</sup> level hierarchy wavefunction can be written as

$$\Psi_1^{HH} = \int \prod_{k=1}^{N_{qp}} d^2 w_k \Phi^*(w_1, \dots, w_{N_{qp}}) \Psi_{N_{qp}}^L(z_1, \dots, z_{N_e}, w_1, \dots, w_{N_{qp}}) , \quad (3.5)$$

where  $\Phi$  is a pseudowavefunction that guides the motion of the quasiparticles, since the above is a superposition of localised quasiparticle with weight  $\Phi$  (it is convenient to have  $\Phi$  be a holomorphic function, however we need conjugates  $w^*$  for the integral not to vanish – hence the conjugate on  $\Phi^*$  in (3.5)). As described above the pseudowavefunction will be of a Laughlin type, as is the 0<sup>th</sup> level wavefunction  $\Psi_{N_{qp}}^L$ .

One may then build subsequent levels of hierarchy states  $\Psi_k^{HH}$  with  $k > 1$  by iterating this procedure, creating unique trial wavefunctions for any filling factor. It can be argued that the stability of the state depends on the denominator of the filling fraction [58].

As written above the wavefunctions are unwieldy due to the integrals, but using methods from conformal field theory (section 3.4.1) these have been

### 3.3. JAIN'S COMPOSITE FERMIONS

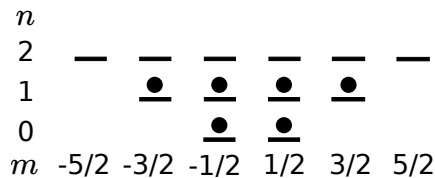


Figure 3.1: Sketch of six electrons occupying two Landau levels on the sphere. The index  $n$  gives the LL while  $m$  denotes the angular momentum.

simplified. Explicit expressions exist on the disk [59–61], the sphere [62] and the torus [63, 64]. In general these require explicit antisymmetrisation, which makes numerical investigations more time consuming.

## 3.3 Jain’s composite fermions

### 3.3.1 Ground states

The composite fermion (CF) approach [3, 17] uses intuition from the conceptually simpler integer quantum Hall effect to generate trial wavefunctions for a series of fractional states. The starting point is the ground state wavefunction for electrons corresponding to an integer number  $n$  Landau levels completely filled:

$$\Phi_n^q = \text{Det}[\phi_i^q(z_j)] . \quad (3.6)$$

The single particle wavefunction indices  $i = (k, m)$  run over Landau level  $k \in \{0, \dots, n - 1\}$  and angular momentum  $m \in \{-k, \dots, k\}$ , and the coordinate indices are  $j \in \{0, \dots, N_e - 1\}$ . Bearing in mind the number of states per LL on the sphere, (2.29) shows that  $\Phi_n^q$  has flux  $2q = N_e/n - n$ . A sketch on the sphere with  $n = 2$  and  $N_e = 6$ , is shown in Fig. 3.1.

These states are noninteracting, and so far have flux corresponding to integer fillings. To model fractional states with electron interactions, even powers of Jastrow factors  $\prod_{i < j} (z_i - z_j)^{2p}$  with  $p \in \mathbb{N}$  are attached to the wavefunction, adding magnetic flux through the Berry phase. Since the determinant is antisymmetric these are fermion states; to create bosons one may use odd powers  $2p - 1$  instead of  $2p$ . The inclusion of these factors has the effect of lowering the probabilities of configurations where the electrons are less spread out, informally “keeping them further apart” – thereby modelling repulsive interactions. The flux attachment procedure adds  $2p(N_e - 1)$  to the highest power of the coordinates. The result is a magnetic flux  $N_\Phi$ , filling factor  $\nu$  and

### 3.3. JAIN'S COMPOSITE FERMIONS

shift  $S$  given by

$$\begin{aligned} N_{\Phi} &= 2q + 2p(N_e - 1) = \frac{N_e}{n} - n + 2p(N_e - 1) , \\ &\implies \nu = \frac{n}{2pn + 1} , \\ S &= 2p + n . \end{aligned} \tag{3.7}$$

When  $n = 1$  this reduces to the Laughlin states, thereby forming a subset of the composite fermion series. As yet the  $n > 1$  states are not good models for the FQHE since the determinant  $\Phi_n$  contains single particle wavefunctions in higher Landau levels. This is remedied by projecting the whole state, yielding the composite fermion ground state wavefunctions

$$\Psi_{\nu}^{CF} = \mathcal{P}_{LLL} \Phi_n^q \prod_{i < j} (z_i - z_j)^{2p} . \tag{3.8}$$

Additional filling factors can be accessed by reverse flux states, obtained by having the initial magnetic field on the electrons point in the opposite direction (inwards on the sphere). This gives the magnetic flux, filling factor, shift and wavefunction

$$\begin{aligned} N_{\Phi} &= -\frac{N_e}{n} + n + 2p(N_e - 1) , \\ \nu &= \frac{n}{2pn - 1} , \\ S &= 2p - n , \\ \Psi_{\nu}^{CF} &= \mathcal{P}_{LLL} \Phi_n^{-|q|} \prod_{i < j} (z_i - z_j)^{2p} , \end{aligned} \tag{3.9}$$

where now  $q < 0$ . Reversing the flux amounts to complex conjugating the electron determinant before projection.

Many of the most prominent lowest Landau level FQHE plateaus are included in the CF series  $\nu = n/(2pn \pm 1)$ , but not all, notably the fraction  $\nu = 4/11$  [14]. It is possible to generate composite fermion wavefunctions for these as well by considering partially filled Landau levels in the determinants  $\Phi^q$ .

### 3.3. JAIN'S COMPOSITE FERMIONS

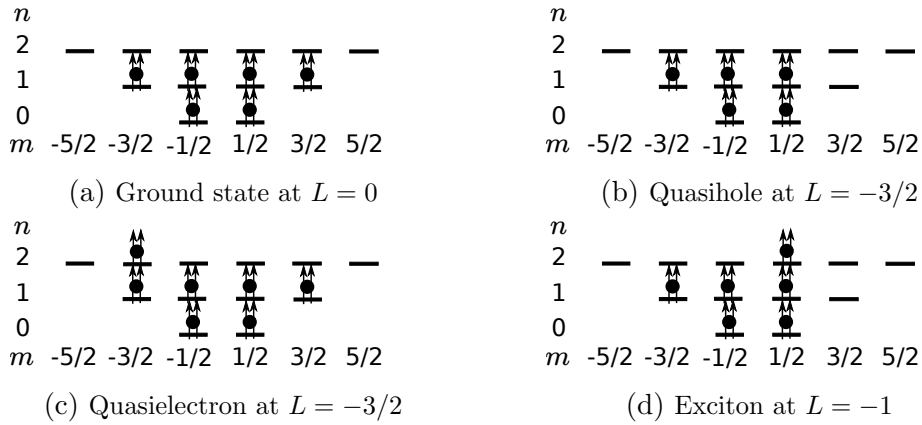


Figure 3.2: Sketches of composite fermion states at effective flux  $2|q| = 1$  and various total angular momenta. Circles with two arrows symbolise electrons with two fluxes attached. The ground state in (a) corresponds to  $n = 2$  CF Landau levels filled, yielding a filling factor  $\nu = 2/5$  (assuming  $2p = 2$  flux attached and original flux in the regular direction  $q > 0$ ). The remaining figures symbolise excitations of this.

#### 3.3.2 Excited states

The ground state wavefunctions provide trial states with an intuitive picture of composite fermions occupying CF Landau levels. The composite fermions can be thought of as emergent particles of the electron system, correlated through flux attachment and lowest Landau level projection. The flux  $2q$  felt by the composite fermions is called the effective flux. A sketch of this can be seen in Fig. 3.2a.

This provides a natural way to create quasiparticle states by altering the determinant of single particle wavefunctions. To form quasiholes it is necessary to lower the ratio of electrons to magnetic flux, which can be accomplished by removing composite fermions from the ground state, and contrarily for quasielectrons (note that for the reverse flux states adding a CF creates a quasihole and vice versa). These constitute charged excitations.

Excitons, being neutral excitations, can be modelled by adding a quasihole and a quasielectron simultaneously. Sketches of these three kinds of excitations are displayed in figures 3.2b, 3.2c and 3.2d respectively. The trial states can be expressed as

$$\Psi_{exc}^{CF} = \mathcal{P}_{LLL} \Phi_{exc}^q \prod_{i < j} (z_i - z_j)^{2p}. \quad (3.10)$$

The total angular momentum  $L$  of the state is obtained by adding those of the individual composite fermions present, which shows that quasiholes contribute the negative angular momentum of the removed states.

A quasihole at level  $k$  in the determinant  $\Phi^q$  will increase the maximum power of every particle in that level by one (after which the determinant anti-

symmetrises over the particles, removing the association of a given particle to a CF LL as it must be for fermions). Doing this in every level increases the max power in general by one, like the Laughlin quasihole. It can be demonstrated that this is exactly a delocalised Laughlin quasihole; i.e. a superposition of localised functions as in (3.3). Thus creating  $n$  CF quasiholes is the same as creating one Laughlin quasihole.

From the above discussion it is clear that composite fermion quasiholes are smaller excitations than Laughlin's variant, with the former in an intuitive sense comprising  $1/n$  of the latter. They therefore have smaller excitation energy. The CF quasielectron wavefunction is further distinct from the Laughlin one and performs better in numerics [65, 66].

The composite fermion model is not guaranteed to yield useful trial wavefunctions, although it has the right universal properties. Quantitative and qualitative numerical investigations show that they are highly favourable, however, by examining properties like ground state energies, overlaps with Coulomb eigenstates, energy gaps and energy spectra [18, 67–69].

Qualitative arguments imply that the quasiparticles have interchange angles  $\theta = \frac{2p}{2pn+1}$  [3]; this can also be shown using clustering arguments introduced by Su [70]. These angles are confirmed through numerical calculations for  $\nu = 1/3$  and  $2/5$  in [71, 72].

## 3.4 Bonderson-Slingerland

Composite fermions wavefunctions are very successful at describing plateaus in the lowest Landau level. In addition they can figure as components in a set of proposed wavefunctions describing states in the second level, outlined in this section.

### 3.4.1 Conformal field theory

Correlators of conformal field theories (CFT) [73] have proven to be another fertile ground for construction of fractional quantum Hall trial wavefunctions. The physical motivation, however, is fairly intricate and only a minimal summary is attempted here.

What is perhaps the clearest connection between CFT and FQHE states arises when considering the edge states [74]. A theory of the low energy FQHE dynamics can be written down in the form of an effective Chern-Simons theory [75, 76]. It allows computation of various quantities, including the resistivity,

but is not automatically gauge invariant when placed on a geometry with an edge. This can be amended by adding a boundary term to the action, which turns out to describe excitations in the form of gapless bosonic edge modes. The dynamics of these modes are characterised by a  $1 + 1$  dimensional conformal field theory of free bosons.

It can also be argued that correlators in conformal field theories yield real space wavefunctions for the quantum Hall bulk [48]; and that these theories are the same as those applied to the edge although strictly speaking the dimensionality is different ( $1 + 1$  and in a sense  $2 + 0$  respectively). Thus the FQHE may embody a principle of holography, which makes intuitive sense from the point of view of charged quasiparticles: any excess charge in the bulk must be compensated on the edge and vice versa.

Motivation and derivations from fundamentals aside, the fact remains that many prominent fractional quantum Hall trial wavefunctions can be generated using CFT, including the Laughlin state and its excitations. These techniques also produce explicit hierarchy wavefunctions without the integrals in (3.5), and the filling factors in the series  $\nu = n/(2pn \pm 1)$  reduce to the composite fermion wavefunctions – suggesting that the two may be different formulations of the same framework [77]. A caveat to the latter claim is that there is some freedom going from the conformal field theory to the real space functions, in particular placement of derivatives, and appropriate choices have to be made to identify composite fermion and hierarchy wavefunctions.

### 3.4.2 Moore-Read

After successfully reproducing several existing trial states Moore and Read inquired whether conformal field theory could also provide novel wavefunctions. In what was originally a demonstration that this is the case and that the result is consistent with the quantum Hall effect they constructed the following function [48]:

$$\Psi_q^{MR} = \text{Pf}\left(\frac{1}{z_i - z_j}\right) \prod_{i < j} (z_i - z_j)^q, \quad (3.11)$$

using the pfaffian  $\text{Pf}(A) = \sum_{\sigma \in S_{2n}} \prod_{i=1}^n A_{\sigma(2i-1)\sigma(2i)}$  of an antisymmetric  $2n \times 2n$  matrix.  $\Psi_q^{MR}$  has coordinate powers corresponding to the filling fraction  $\nu = 1/q$  with shift  $S = q + 1$  on the sphere. The pfaffian is antisymmetric, however, meaning that in order to describe fermions  $q$  must be even – thus describing an even denominator state.

Though it was originally meant as an example it was proposed [78] that

this state with  $q = 2$  might describe the prominent plateau at  $\nu = 2 + 1/2$  observed in the second Landau level [15] (where the increase by two in  $\nu$  corresponds to filling both sets of spin states in the lowest Landau level). Numerical calculations confirm that this is the case and  $\Psi_2^{MR}$  turns out to be very competitive at this filling factor [79, 80], as does its particle-hole dual [81–83].

Intriguingly the underlying CFT shows that (3.11) supports quasiparticles with nonabelian statistics, as alluded to in section 3.1.2. In particular the elementary excitation is a charge  $\pm e/(2q)$  nonabelian anyon of the Ising type. These can fuse to abelian charge  $\pm e/q$  Laughlin-type quasiparticles. It has been demonstrated, however, that Ising anyons do not facilitate universal quantum computation unless one also includes topologically unprotected operations [84].

Much like the Laughlin wavefunction, the Moore-Read state is the lowest density ground state of a model Hamiltonian, but one which discourages nearing of triplets of particles rather than pairs as with the hardcore interaction [78]:

$$V_3 = \sum_{ijk}^{\text{triples}} \delta(z_i - z_j) \delta(z_i - z_k) . \quad (3.12)$$

This is most easily seen for the  $\nu = 1$  state at  $q = 1$ , which has zero energy in the above potential.

Compared to Laughlin’s wavefunction the Moore-Read state is thus characterised by pairing in that it strongly deters triplets rather than pairs from approaching (the fermionic state at  $q = 2$  also necessarily vanishes when pairs coincide but to a lower power than the corresponding Laughlin state). This is recognised also by considering the pfaffian in (3.11), the single terms of which lowers the powers of the relative binomials. Finally the pairing shows up in the pair correlation function as the correlation hole has a distinct shape with a “shoulder” allowing the pairs closer together (see figure 2.1d). This concept was generalised to a set of  $k$ -body clustered states by Read and Rezayi [85], of which (3.11) corresponds to  $k = 2$ .

### Excited states

Several schemes have been proposed for explicit wavefunctions for the excited states. One suggestion for quasiholes consists of the ground states of (3.12) at altered magnetic flux  $N_\Phi$ , and these perform fairly well in numerical calculations [86, 87]. Constructions based on CFT [88] and vanishing properties [89]

also give expressions for quasielectrons and excitons. The most relevant proposal for the purposes of this work, however, uses the fact that  $\Psi_1^{MR}$  can be written as two symmetrised layers of  $\nu = 1/2$  Laughlin wavefunctions to propose the excited states [90]

$$\Psi_{exc}^{MR} = \mathcal{S} \left( \Psi_{exc,1}^{CF}(z_1, \dots, z_{N_e/2}) \times \Psi_{exc,2}^{CF}(z_{N_e/2+1}, \dots, z_{N_e}) \right) \prod_{i < j} (z_i - z_j). \quad (3.13)$$

$\Psi_{exc,i}^{CF}$  for  $i = 1, 2$  are bosonic composite fermion excited states (3.10) at  $\nu = 1/2$  of the first and second half of the electrons, respectively, and  $\mathcal{S}$  symmetrises over all possible divisions of the particles into these two groups. A similar construction was presented in [91]. These states match the exact spectra reasonably well and observe state counting predicted through other means [86,92]. Note that all the mentioned proposals generate the same quasiholes, while the quasielectrons and excitons are different.

### 3.4.3 A second Landau level hierarchy

After observing that few of the second Landau level plateaus are well described by the corresponding lowest Landau level states, Bonderson and Slingerland [93] considered a hierarchy similar in spirit to that of Haldane and Halperin (section 3.2.3) but built on the  $\nu = 5/2$  Moore-Read state; suggesting that the SLL in general might be characterised by pairing. The state at  $\nu = 5/2$  is the most prominent state in the SLL (with competition from  $\nu = 7/3$  and  $8/3$ ), and as such play the role of the  $\nu = 1/3$  Laughlin state in the lowest Landau level hierarchy.

This second Landau level hierarchy, called the BS wavefunctions, has more possibilities than the LLL one as the 0<sup>th</sup> level has several species of quasiparticles; the authors mostly focus on the simplest case where the condensing particles are of the Laughlin type with charge  $\pm e/2$ . In this case one may build trial wavefunctions for the observed states  $\nu = 8/3$  and  $12/5$  [94] in the 1<sup>st</sup> hierarchy level and  $\nu = 19/8$  [16] in the 2<sup>nd</sup> level.

Inspired by the correspondence between the lowest Landau level hierarchy wavefunctions and composite fermions, some of the BS ground state wavefunctions can be simplified to take the form of CF wavefunctions multiplying a bosonic Moore-Read state:

$$\Psi^{BS-CF} = \Psi_1^{MR} \Psi^{CF}. \quad (3.14)$$

The fact that multiplying factors amounts to adding powers, and the relations (3.7) and (3.9), imply that these have magnetic flux, filling factor and shift

$$\begin{aligned} N_{\Phi} &= (2p + 1)(N_e - 1) \pm \left( \frac{N_e}{n} - n \right) - 1 \\ \implies \nu &= \frac{n}{(2p + 1)n \pm 1} \\ S &= 2p + 2 \pm n, \end{aligned} \tag{3.15}$$

with the composite fermion parameters  $n$  (number of filled CF Landau levels) and  $p$  (number of attached flux quantum pairs) and the sign  $\pm$  corresponding to regular and reverse flux CF respectively. This series includes  $\nu = 12/5$  and  $19/8$  but not  $\nu = 8/3$ .

The functions in (3.14) are not identical to the hierarchical Bonderson-Slingerland wavefunctions, differing in the placement of the projection operators. They are expected to be in the same universality class, however, and should have similar properties – either way  $\Psi^{BS-CF}$  is a trial wavefunction that can be tested numerically.

### Testing the BS states

The special case  $\nu = 12/5$ , i.e. incorporating a reverse flux  $\nu = 2/3$  CF factor with  $n = 2$  and  $p = 1$ , is tested numerically in [95]. At the time of writing there were three main trial wavefunction contenders at this filling; namely the lowest Landau level hierarchy, the Bonderson-Slingerland state, and the particle-hole conjugate of the Read-Rezayi state with  $k = 3$ . Since then another state has been promoted [96] (again using particle-hole conjugation) which is a special case of the construction in ref. [97]. Of these only the quasiparticles of the Read-Rezayi state are applicable for universal quantum computation without additional unprotected gates, however. It is therefore crucial to determine which of these, if any, describe most closely the real system.

The Read-Rezayi wavefunction has been demonstrated to be favourable in numerical investigations [85, 98]. Ref. [95] examines exact excitation gaps as a function of the spherical shift and variational energies and overlaps of the Bonderson-Slingerland state with the second Landau level Coulomb ground state. Additional optimisations of the BS state through replacement of the pfaffian by improved pair wavefunctions [99] and perturbations of the Coulomb potential are also employed. The results indicate that both the Bonderson-Slingerland and Read-Rezayi states are viable trial states, but does not con-

clusively settle the issue; in fact suggesting that different physical realisations may be described by one or the other.

The  $\nu = 12/5$  and  $\nu = 13/5$  states have also been studied for larger systems using density matrix renormalisation group techniques in ref. [100]. It is argued that the Read-Rezayi state matches the system to a large degree by examining, among other things, entanglement spectra and the energies of the excitations.

Only ground states of  $\Psi^{BS-CF}$  have been studied, however, and it is of interest also to investigate how close its excitations match the real system. The formulation in (3.14) suggests two natural sets of quasiparticles: exciting the composite fermion sector as in (3.10) or the pfaffian sector as in (3.13). Both of these are constructed and compared to results from exact diagonalisation in section 5.4.

# Chapter 4

## Numerical methods

The numerical results in the following chapters are obtained through Monte Carlo computations and exact diagonalisation, where the latter is mostly used to assess the results acquired through the former. This chapter reviews these methods and how we use them on the sphere.

### 4.1 Exact diagonalisation

Knowing the energy eigenvalues and eigenstates can tell us a lot about a system, and these can be obtained using exact diagonalisation of the Hamiltonian  $H$ . In the context of the quantum Hall effect the method was first applied on the torus [35]. The word “exact” in this case can refer both to the fact that the numerical computation is usually performed to machine precision and that it yields the exact solution of the eigenvalue problem of  $H$ . This section gives a short description of the procedure; all the diagonalisation calculations in this work were done using code developed by other authors (see below). The computations are done on the sphere with the relevant Hamiltonian (2.22).

The first step is to build a multiparticle basis, which can be done using Slater determinants  $\Phi_n$  of single particle wavefunctions  $\phi_k$ , in our case given in (2.25). These can be expressed as  $\Phi_n = \mathcal{A}[\bigotimes_{k=1}^{N_e} \phi_{n_k}]$  with the antisymmetrisation  $\mathcal{A}$  and a chosen occupation  $n$  of the single particle functions. The Hamiltonian matrix to be diagonalised is then

$$H_{nm} = \langle \Phi_n | H | \Phi_m \rangle = \sum_{\substack{i,j \in n, k,l \in m \\ i+j=k+l}} A_{ijkl} \langle \Phi_n | c_i^\dagger c_j^\dagger c_k c_l | \Phi_m \rangle, \quad (4.1)$$

where we have assumed that  $H$  is a two-body operator to simplify the expression in terms of second quantised creation operators  $c_k^\dagger$ . The constraint

#### 4.1. EXACT DIAGONALISATION

$i + j = k + l$  expresses momentum conservation. Going to position space one can then compute the coefficients as

$$A_{ijkl} = \int \int d\Omega_1 d\Omega_2 \phi_i^*(\mathbf{r}_1) \phi_j^*(\mathbf{r}_2) V(|\mathbf{r}_2 - \mathbf{r}_1|) \phi_k(\mathbf{r}_1) \phi_l(\mathbf{r}_2), \quad (4.2)$$

assuming a central potential  $V$  (necessary when using pseudopotentials but not in general). The matrix  $H_{nm}$  can be constructed from the coefficients  $A_{ijkl}$  using efficient algorithms in terms of the creation operators.

Computationally the procedure is resource intensive because it involves diagonalisation of large matrices, whose dimension equals that of the lowest Landau level Hilbert space. Its size is given by the number of ways to distribute  $N_e$  fermions over  $N_\Phi$  states, i.e.  $\binom{N_\Phi}{N_e}$ . This increases exponentially with  $N_e$ , as can be seen defining  $\xi \equiv \nu^{-1}$  and using  $N_\Phi \approx \xi N_e$ :

$$\binom{N_\Phi}{N_e} \sim \frac{1}{2\pi N_e} \sqrt{\frac{\xi}{\xi - 1}} \left( \frac{\xi^\xi}{(\xi - 1)^{\xi-1}} \right)^{N_e}. \quad (4.3)$$

The system sizes suitable for diagonalisation are thus limited. This can be alleviated somewhat using symmetries of the Hamiltonian. One constructs a new basis  $\Phi'_n$  in which  $H$  is block-diagonal, each block corresponding to a sector of the symmetry. The procedure is then performed within the smaller blocks. The numerical tools that we have utilised incorporate the Krylov-Schur [101], Arnoldi [102] and Lanczos [103] algorithms; with the diagonalisation done in such a way that when retrieving a chosen number of eigenvalues and eigenstates they are ordered with respect to increasing energy.

For our purposes we are often interested in obtaining all states of a given system with certain angular momentum numbers  $(L, M)$  of the operators  $L^2$  and  $L_z$ , see (2.30). Getting the desired total  $z$ -component value  $M$  is straightforward, since  $M$  is the total degree of the polynomial, which is the sum of the degrees of the single particle wave functions. It is thus sufficient to use a restriction on the single particle wavefunctions  $\psi_k$  included in the basis states  $\Psi_n$ . A fast recursive algorithm for selecting these can be constructed.

In order to separate out states with a certain eigenvalue  $L = L_0$  we consider states with the maximal value of the  $z$ -component  $M = L_0$  and add a term to the Hamiltonian:  $H \rightarrow H + \epsilon \hat{L}^2$  with  $\epsilon \in \mathbb{R}$  (recall the notation  $\hat{L}^2 \Psi_L = L(L+1)\Psi_L$ ). When  $\epsilon$  is large enough this means that the lowest energy states also have the lowest  $L$ -values. In this way the states retrieved are ordered with increasing  $L$ , starting at  $L = L_0$ . The correct eigenvalues can be reconstructed

by subtracting the contribution from  $\epsilon \widehat{L}^2$ .

For our purposes exact diagonalisation has two functions: constructing the energy projection (section 5.1.3) and comparison with results from trial wavefunctions. In the latter case the eigenvalues and eigenstates are seen as the exact solutions of the model and can be used as a measure of how well the trial states represent the system. The latter can then be used to study system sizes and quantities which are inaccessible or hard to compute through exact diagonalisation.

## 4.2 Monte Carlo

Monte Carlo (MC) computation is a broad term that is used in general of any calculation that involves random numbers, but we will use it to refer more specifically to evaluating integrals by interpreting them as expectation values. The presentation below is based on [104].

### 4.2.1 Approximating integrals

As the simplest example consider approximating  $\int_a^b f(x)dx$  by drawing  $n$  uniformly distributed random numbers  $x$  between  $a$  and  $b$ , evaluating  $f(x)$ , and taking the average. As  $n \rightarrow \infty$  we will get the exact value, with the error decreasing with  $n$ . Using the standard deviation of the mean as an error estimate we get

$$\epsilon = \sigma_m \approx \frac{\sigma_0}{\sqrt{n-1}} \sim n^{-1/2} , \quad (4.4)$$

where  $\sigma_0$  is the spread of the function over our random values. Thus in general the error of Monte Carlo computations goes as the inverse square root of the number of samples. This is not particularly impressive, but the main strength of MC calculations is that this also holds for higher dimensional integrals; which entail picking random points in a higher dimensional space but getting the same general  $n$ -dependence in the error. Other methods of numerical integration are in general much slower in higher dimensions.

The naive method above is not efficient, however, since it prescribes picking all numbers with equal probabilities. We may then spend a lot of time adding very small numbers that do not change the average much. This can be mitigated by using what is known as importance sampling: we rewrite the integral as

$$\int_a^b f(x) = \int_a^b \frac{f(x)}{P(x)} P(x) dx , \quad (4.5)$$

## 4.2. MONTE CARLO

where  $P(x)$  is some chosen valid probability distribution. This has the form of an expectation value, which means that it can be approximated by drawing samples  $x$  from the distribution  $P(x)$  and then taking the average over the remaining factor of the integrand:

$$\int_a^b \frac{f(x)}{P(x)} P(x) dx \approx \frac{1}{n} \sum_{k=1}^n \frac{f(x)}{P(x)} \Big|_{x=x_k^{(p)}}, \quad (4.6)$$

where  $x_k^{(p)}$  is the  $k$ 'th random sample drawn from  $P(x)$ . Again the error estimate will go as  $n^{-1/2}$ , but by choosing  $P$  cleverly we can make  $\sigma_0$  smaller. In general we want to have a distribution function that is similar to the original integrand, to sample most often the values that will contribute the most to the estimate.

### Markov chains and detailed balance

The next step is to find a way to generate samples from the probability distribution. We use a Markov process, where one generates a sample  $k$  from a previous one  $j$  using a transition probability  $T_{j \rightarrow k}$ ; and in this way constructs a set of samples iteratively. This is a non-deterministic method that, given certain restrictions on the  $T$ 's, yields a set drawn from the correct probability distribution  $P$ .

Firstly the  $T$ 's have to be valid probabilities; i.e.

$$\sum_j T_{j \rightarrow k} = 1 \quad \forall \quad k. \quad (4.7)$$

Secondly, it must be possible to reach any state  $k$  from another  $j$  where they both occur in  $P$ , or we could end up in a situation where we never generate a sample that should have nonzero probability. This is known as ergodicity. Lastly we have to satisfy detailed balance:

If  $p_t(k)$  is the probability for the system to be in state  $k$  at iteration  $t$ , equilibrium of the Markov chain is described by (using (4.7)):

$$p_{t+1}(k) = \sum_j p_t(j) T_{j \rightarrow k}, \quad (4.8)$$

so that the transition frequency into and out of a state are equal. But although this describes an equilibrium we are not guaranteed that the samples generated from the process are drawn from the correct probability distribution  $P$  because

we may end up in a limit cycle. This is avoided by imposing the condition of detailed balance:

$$p_{t+1}(k)T_{k \rightarrow j} = p_t(j)T_{j \rightarrow k} \quad \forall \quad j, k, \quad (4.9)$$

or in terms of the sampling probabilities:

$$P(x_k)T_{k \rightarrow j} = P(x_j)T_{j \rightarrow k} \quad \forall \quad j, k. \quad (4.10)$$

This means that the probability of going from a given state to another equals the probability of the opposite.

### The Metropolis algorithm

The Metropolis algorithm [105] is a Markov chain that from a given state  $j$  proposes a random state  $k$  and then accepts or rejects it depending on the two states according to  $T_{j \rightarrow k}$  in a way that satisfies the necessary conditions. The transition probabilities are

$$T_{j \rightarrow k} = \begin{cases} P(x_k)/P(x_j) & : P(x_k) < P(x_j) \\ 1 & : P(x_k) \geq P(x_j) \end{cases}. \quad (4.11)$$

One may check that detailed balance is satisfied by substituting (4.11) into (4.10) and testing the two cases  $P(x_k) < P(x_j)$  and the opposite.

We will be computing quantum mechanical expectation values  $\langle \mathcal{O} \rangle = \int d\Omega \mathcal{O} |\Psi|^2$  and overlaps  $\langle \psi | \phi \rangle = \int d\Omega \psi^* \phi$ , where  $d\Omega$  is the measure over the multidimensional configuration space, a cartesian product of spheres. In each case we seek the best choice for the probability  $P(\Omega)$ ; in the simplest case of an observable that can be computed for a single wavefunction, for example the variational energy, the best choice is usually  $P = |\Psi|^2$ :

$$\langle U \rangle = \int d\Omega U(\Omega) |\Psi(\Omega)|^2 \approx \frac{1}{n} \sum_{k=1}^n E(\Omega_k) \Big|_{\Omega = \Omega_k^{(|\Psi|^2)}}, \quad (4.12)$$

and we see that the summand is simple while the sampling distribution is similar to the integrand and should be a good choice for importance sampling.

We work with wavefunctions, and thus probabilities, where the normalisation is unknown. But from (4.11) we see that this does not matter for the Metropolis algorithm since it only involves fractions of probabilities. In effect this means that the last factor  $P$  in (4.5) will always be normalised. For a simple case as in (4.12) where the resulting summand does not depend on any-

thing that needs to be normalised this is the end of the story, but other cases are more complicated.

### Normalisation

As an example we consider the overlap between two wavefunctions  $\psi$  and  $\phi$ . We assume that their normalisation is unknown and denote unnormalised quantities with tildes:

$$\mathcal{N}_\psi = \int d\Omega |\tilde{\psi}|^2, \quad (4.13)$$

and correspondingly for  $\mathcal{N}_\phi$ . First of all we cannot use the complex  $\psi^*\phi$  as a probability distribution. This is a common problem for Monte Carlo integrals, and means that we have to choose a different  $P$  – a natural choice in this case would be  $P = |\psi|^2$  or  $P = |\phi|^2$ . Secondly we have to take into account that the sampling probability is automatically normalised while in general we do not know the probability norm  $\mathcal{N}_p = \int d\Omega \tilde{P}$ . This leads us to

$$\langle \psi | \phi \rangle = \int d\Omega \psi^* \phi = \frac{\mathcal{N}_p}{\sqrt{\mathcal{N}_\psi \mathcal{N}_\phi}} \int d\Omega \frac{\tilde{\psi}^* \tilde{\phi}}{\tilde{P}} P \approx \frac{\mathcal{N}_p}{n \sqrt{\mathcal{N}_\psi \mathcal{N}_\phi}} \sum_{k=1}^n \frac{\tilde{\psi}^* \tilde{\phi}}{\tilde{P}} \Big|_k, \quad (4.14)$$

where the MC summand only depends on unnormalised and thus known quantities, and ‘ $|_k$ ’ is an abbreviation for setting  $\Omega = \Omega_k^{(p)}$ . We can estimate the normalisation in a similar way:

$$\mathcal{N}_\psi = \mathcal{N}_p \int d\Omega \frac{|\tilde{\psi}|^2}{\tilde{P}} P \approx \frac{\mathcal{N}_p}{n} \sum_{k=1}^n \frac{|\tilde{\psi}|^2}{\tilde{P}} \Big|_k, \quad (4.15)$$

and correspondingly for  $\mathcal{N}_\phi$ , so that in the end we have the normalised estimate

$$\langle \psi | \phi \rangle \approx \frac{\sum_{k=1}^n \frac{\tilde{\psi}^* \tilde{\phi}}{\tilde{P}} \Big|_k}{\sqrt{\sum_{k=1}^n \frac{|\tilde{\psi}|^2}{\tilde{P}} \Big|_k \sum_{k=1}^n \frac{|\tilde{\phi}|^2}{\tilde{P}} \Big|_k}}. \quad (4.16)$$

Different integrals require different ways of handling the normalisation. The factors in a Gram-Schmidt orthogonalisation, for instance, can be estimated as

$$\frac{\langle \tilde{\psi} | \tilde{\phi} \rangle}{\langle \tilde{\psi} | \tilde{\psi} \rangle} \approx \frac{\sum_{k=1}^n \frac{\tilde{\psi}^* \tilde{\phi}}{\tilde{P}} \Big|_k}{\sum_{k=1}^n \frac{|\tilde{\psi}|^2}{\tilde{P}} \Big|_k}. \quad (4.17)$$

There are other quantities for which it is hard to construct an efficient normalised expression; e.g. computing  $\mathcal{N}_\psi$  itself. The naive way, i.e. using

$P = |\tilde{\psi}|^2$ , does not work because it leads to a circular situation where one has to know the result in advance in order to find it. Therefore it is necessary to choose another  $P$  for which the Monte Carlo computation will not converge as fast. Similar reasoning shows why we cannot simply use  $P = E|\psi|^2$  in (4.12).

### Sampling strategy

Although a Markov chain satisfying ergodicity and detailed balance guarantees that one will generate samples for the chosen probability after an infinite number of iterations, we have to start accumulating samples at some point. How long we have to wait until the chain reaches an equilibrium and we can start sampling depends on the probability and the integrand (i.e. which observable is being computed), and has to be checked empirically. We begin in some initial state and then start running the chain, plotting the result from each sample, and note when it stabilises (with smaller random fluctuations). After doing this a few times one can estimate how many initial iterations are necessary; this is referred to as the thermalisation time.

Naive error estimates assume that the individual samples are statistically independent, but that is not generally the case when sampling from consecutive Metropolis iterations. In our case we will move a single electron for every iteration, meaning that they are clearly dependent. Although there are methods to estimate errors from dependent samples (see section 4.2.3) it is not efficient to sample every iteration after thermalisation, and instead we wait for a number of iterations between sampling. The optimal value of this number gives a balance between getting close to independent samples and not waiting longer than necessary, and an estimate can be obtained by comparing computation time and error for different sampling intervals. Usually it turns out to be of order  $\sim N_e$ , allowing each particle a few steps between every sampling.

Finally, it is not always efficient even when possible to use the squared wavefunction itself as a probability in computing an observable, as in (4.12). This may be because the wavefunction is computationally intensive and it would save time to only compute it on the iterations we sample, or because we already have generated a set of configurations that we would like to use for computing several integrals. In that case we use an estimate analogous to (4.16) for the relevant observable. The convergence will usually be slower than using the squared wavefunction itself, but keeping the considerations above in mind the computation can still be more efficient.

### 4.2.2 Monte Carlo on the sphere

When proposing a step for the Metropolis algorithm on the sphere the simplest procedure is choosing a random electron and then testing a random move in terms of spherical coordinates  $(\theta, \phi) \rightarrow (\theta + \Delta\theta, \phi + \Delta\phi)$  of a random steplength up to a certain maximum and with periodic boundaries.

As described above this will not satisfy detailed balance, however, because the configuration space of an electron on the sphere is curved while  $(\theta, \phi)$ -space is rectangular, and these steps will be biased because steps in  $\theta$  are not symmetric. One way of getting around this is to make the step in a different way than a simple one in angle space, for example in the flat three dimensional Cartesian space and then projecting onto the sphere in an unbiased way. This makes the algorithm more time consuming, however, and instead we have constructed a curved space Metropolis algorithm.

To analyse the situation we break the transition probability  $T_{j \rightarrow k}$  in (4.10) into two parts:  $t_{j \rightarrow k}$ , the probability of testing a move from  $j$  to  $k$ , and  $a_{j \rightarrow k}$ , the probability of accepting it. Implementing detailed balance with these quantities then amounts to

$$\begin{aligned} T_{j \rightarrow k} &= t_{j \rightarrow k} a_{j \rightarrow k} \Rightarrow \\ P(j) t_{j \rightarrow k} a_{j \rightarrow k} &= P(k) t_{k \rightarrow j} a_{k \rightarrow j} , \end{aligned} \quad (4.18)$$

where again  $P(x_j)$  is the probability to be in state  $x_j$ . In the analysis of section 4.2.1 we implicitly assumed that  $t_{j \rightarrow k} = t_{k \rightarrow j}$ , which is not the case with steps in the angle space. To compensate for this we alter  $a_{j \rightarrow k}$  away from the straightforward Metropolis implementation (4.11):

Consider a step  $(\theta_j, \phi_j) \rightarrow (\theta_k, \phi_k)$  and its reverse. Even if we are choosing any angle within the steplength all with the same probability, if  $\theta_k$  is closer to the equator than  $\theta_j$ , the associated area we are stepping into is larger and the chance of choosing  $(\theta_k, \phi_k)$  is smaller than that of choosing  $(\theta_j, \phi_j)$  in the reverse situation. The volume element on the sphere is  $dS = \sin\theta d\theta d\phi$ , and assuming that the step length is relatively small, we estimate

$$t_{j \rightarrow k} \propto \frac{1}{\sin\theta_k} . \quad (4.19)$$

This leads us to the following variant of the Metropolis algorithm, where we

are free to make the steps uniformly in angle space:

$$a_{j \rightarrow k} = \begin{cases} \frac{P(x_k) \sin \theta_k}{P(x_j) \sin \theta_j} & : \frac{P(x_k) \sin \theta_k}{P(x_j) \sin \theta_j} < 1 \\ 1 & : \frac{P(x_k) \sin \theta_k}{P(x_j) \sin \theta_j} \geq 1 \end{cases}. \quad (4.20)$$

To confirm that this satisfies detailed balance we first assume that  $P(x_k) \sin \theta_k < P(x_j) \sin \theta_j$ , so that we have the first condition in (4.20). We fill in (4.18), keeping in mind that for the right hand side the step is from  $k$  to  $j$  and so everything in (4.20) has to be reversed and its second condition is true:

$$P(j) \frac{1}{\sin \theta_k} \frac{P(x_k) \sin \theta_k}{P(x_j) \sin \theta_j} = P(k) \frac{1}{\sin \theta_j} \cdot 1, \quad (4.21)$$

showing that the condition is satisfied. We can then assume  $P(x_k) \sin \theta_k \geq P(x_j) \sin \theta_j$  and perform the same analysis. Numerical testing confirms that this gives the same results as stepping in an unbiased way from the outset.

Note that the procedure outlined above is not guaranteed to work near the poles, where one should rather test steps in a curved biconic shape (like a bowtie on the sphere). After testing this, however, we concluded that the resulting correction is much smaller than the typical error.

The optimal maximum step length can be found empirically by comparing errors and computation times (and making sure that we do not end up in a local minimum), and for our computations we find that an ideal one gives an acceptance of  $\sim 50\%$ . This corresponds to a relatively short step length, indicating that the analysis of detailed balance above is applicable.

### 4.2.3 Error estimation

The most naive estimate for the error is given by the standard deviation of the mean of the Monte Carlo summand over the samples, as in (4.4). However this is only valid for independent samples and observables that are defined for a single MC sample. Counterexamples to the latter are normalised energy eigenstate overlaps (necessary for the energy projection in section 5.1.3), where the sum of the squares of all the lowest Landau level overlaps is involved, or energy eigenvalues from a diagonalised subspace of excited states (see section 5.2.1).

One method of estimate the error in cases like the above is called binning errors. It is computed by separating the samples into  $n_b$  bins, computing the relevant observable  $\mathcal{O}$  in each bin, and finding the standard deviation of the

## 4.2. MONTE CARLO

mean over the bins, i.e.

$$\epsilon_{\text{bin}} = \sqrt{\frac{\langle \mathcal{O}_b^2 \rangle - \langle \mathcal{O}_b \rangle^2}{n_b - 1}}, \quad (4.22)$$

where  $\mathcal{O}_b$  is the value computed for the observable in bin  $b$ .

This gives a measure of the spread of the data and can be computed in more involved cases like the ones mentioned above – and we can see that dependency of the samples is suppressed by treating bins of samples as independent rather than individual ones. The best justification however is a comparison to brute force estimates, which in testing are within a factor of two of the bin estimates. Brute force in this context refers to actually computing the final result a number of times and taking the standard deviation of the outcomes.

The estimate (4.22) depends on the number of bins  $n_b$ . An optimal number can be found by plotting it against the error estimate and noting which range of  $n_b$  gives a stable result. All Monte Carlo errors in this work are estimated using bin errors.

Usually it is expected that the jackknife and bootstrap methods of estimating the errors (see ref. [104]) will give better results than the bin error described above. Regarding the calculations in this work, however, it was found that the latter gave better estimates when compared to brute force calculation of the error: the jackknife and bootstrap results were consistently closer to the naive estimate (4.4).

# Chapter 5

## Results from trial wavefunctions

This chapter contains most of our numerical results. Various fractional quantum Hall effect trial wavefunctions are studied in different contexts and employing different projection methods; the implications of the results are then discussed.

### 5.1 Lowest Landau level Projection

Several of the prominent fractional quantum Hall trial wavefunctions incorporate a projection to the lowest Landau level, in particular composite fermions and CFT hierarchy wavefunctions. As we will see this is in general resource intensive, and often comprises the main obstacle to fast evaluation of the wavefunctions.

After reviewing the analytic procedure we will present a commonly used approximation for the projection of composite fermion states and show an improvement of this. Subsequently we propose and test an entirely new and general method of projection.

#### 5.1.1 Exact projection

Assuming a Fock space representation of the state the projection is straightforward: simply eliminate constituents in higher Landau levels. With trial wavefunctions, however, one usually works with real space representations  $\Psi(z_k, z_k^*)$  where the components in different LL's are not as cleanly separated. Girvin and Jach [23] showed that the projection can be accomplished with real space functions on the disk using the following operation:

$$\mathcal{P}_{LLL}\Psi(z_1, z_1^*, \dots, z_{N_e}, z_{N_e}^*) = :\Psi(z_1, 2\partial_1, \dots, z_{N_e}, 2\partial_{N_e}):, \quad (5.1)$$

where  $:$  indicates a normal ordering that shifts all conjugate coordinates  $z^*$  to the left before substitution with derivatives. Note that these derivatives act only on the polynomial part and not the implicit Gaussian factors (or alternatively the normal ordering places the Gaussians to the left of the differential operators). The procedure in (5.1) is natural in the sense that it maps general functions to holomorphic ones, which as pointed out above (2.17) reside in the lowest Landau level. Following ref. [3] the proof of (5.1) can be stated as follows:

Consider a general single particle wavefunction on the plane, reinstating the Gaussian factor:  $\psi(z, z^*) = \sum_{j,k} c_{jk} z^j z^{*k} \exp(-|z|^2/4)$ . We want to confirm that the projected function  $\mathcal{P}_{LLL}\psi(z, z^*) = :\psi(z, \partial_z):$ , where the derivatives do not act on the Gaussian part, have the same overlaps with any lowest Landau level wavefunction as the unprojected function. To check this we compare with the angular momentum basis functions  $\phi_m(z, z^*) = z^m \exp(-|z|^2/4)$ :

$$\begin{aligned}
 \langle \phi_m | \psi \rangle &= \int dS z^{*m} e^{-\frac{1}{4}|z|^2} \sum_{j,k} c_{jk} z^j z^{*k} e^{-\frac{1}{4}|z|^2} \\
 &= \sum_{j,k} c_{jk} \int dS z^{*m} z^j (-2\partial_z)^k e^{-\frac{1}{2}zz^*} \\
 &= \sum_{j,k} c_{jk} \int dS e^{-\frac{1}{2}zz^*} (2\partial_z)^k (z^{*m} z^j) \\
 &= \sum_{j,k} c_{jk} \int dS e^{-\frac{1}{4}|z|^2} z^{*m} e^{-\frac{1}{4}|z|^2} (2\partial_z)^k z^j = \langle \phi_m | \mathcal{P}_{LLL}\psi \rangle, \quad (5.2)
 \end{aligned}$$

where we have used that the boundary terms vanish in the partial integration of the third line. The generalisation to multiparticle states is straightforward.

The spherical version is similar, with  $(u_k^*, v_k^*) \rightarrow (\partial_{u_k}, \partial_{v_k})$  in terms of spinor coordinates (2.26) (up to normalisation) [18]. On the torus the projection is more complicated because derivatives do not adhere to the periodic boundary conditions, necessitating superpositions of translation operators [64].

The projection conserves angular momentum and filling factor. However, even given a wavefunction that is relatively simple before projection, the derivatives will in general produce very complicated polynomials. This complexity grows quickly with the number of particles and imposes a strong limit on the system sizes that can be computed in practice.

### 5.1.2 Jain-Kamilla projection

Early studies of composite fermion states [65, 67, 106–109] were able to investigate different aspects using exact projection, including ground state energies, energy gaps, Coulomb state overlaps and excitation spectra. These analyses, however, were necessarily using a limited number of electrons. Larger systems became available with the approximation known as Jain-Kamilla projection.

The composite fermion wavefunction (3.8) can be rewritten by taking the Slater determinants from the flux attachment into the CF determinant:

$$\Psi_\nu^{CF} = \mathcal{P}_{LLL} \Phi_n^q \prod_{i<j} (z_i - z_j)^{2p} = \mathcal{P}_{LLL} \begin{vmatrix} \phi_1^q(z_1) J_1^p & \phi_1^q(z_2) J_2^p & \dots \\ \phi_2^q(z_1) J_1^p & \phi_2^q(z_2) J_2^p & \\ \vdots & & \ddots \end{vmatrix}, \quad (5.3)$$

where  $\phi_i$  are single particle wavefunctions and  $J_i = \prod_{j \neq i} (z_i - z_j)$ . Jain and Kamilla [18] proposed to approximate this wavefunction with

$$\Psi_\nu^{CF-JK} = \begin{vmatrix} \mathcal{P}_{LLL} \phi_1^q(z_1) J_1^p & \mathcal{P}_{LLL} \phi_1^q(z_2) J_2^p & \dots \\ \mathcal{P}_{LLL} \phi_2^q(z_1) J_1^p & \mathcal{P}_{LLL} \phi_2^q(z_2) J_2^p & \\ \vdots & & \ddots \end{vmatrix}, \quad (5.4)$$

so that the projection acts on individual elements of the determinant rather than the whole wavefunction. This gives a different expression with fewer derivatives. Numerical testing shows that it gives a good description of the FQHE system [18, 19, 68], however, which is what matters in the end. Following is a detailed account of the procedure.

#### Regular flux

We will call the elements in the determinant of (5.4) composite fermion orbitals  $\eta_{n,m,j}^q$ , where  $n$ ,  $m$  and  $j$  are the Landau level, angular momentum and coordinate index of the single particle elements; keeping in mind that each orbital then depends on the positions of all the electrons. Using the single particle expressions, Jain and Kamilla showed that for the regular flux composite fermions these orbitals are given by

$$\eta_{n,m,j}^q = \mathcal{N}_{qnm} (-1)^{q+n-m} \frac{(N_\Phi + 1)!}{(N_\Phi + n + 1)!} \sum_{s=0}^n (-1)^s \binom{n}{s} \times \left( \begin{matrix} 2q + n \\ q + m + s \end{matrix} \right) \left( \frac{\partial}{\partial u_j} \right)^s u_j^{q+m+s} \left( \frac{\partial}{\partial v_j} \right)^{n-s} v_j^{q-m+n-s} J_j, \quad (5.5)$$

with the normalisation

$$\mathcal{N}_{qnm} = \sqrt{\frac{2|q| + 2n + 1}{4\pi} \frac{(|q| + n - m)! (|q| + n + m)!}{n! (2|q| + n)!}}. \quad (5.6)$$

They also constructed an efficient algorithm for computing  $\eta_{n,m,j}^q$ .

### Reverse flux

The procedure above was extended to reverse flux composite fermions by Möller and Simon [19], who found a similar expression for the orbitals:

$$\begin{aligned} \eta_{n,m,j}^{-|q|} = & \mathcal{N}_{qnm} (-1)^n \frac{(N_\Phi + 1)!}{(N_\Phi - 2|q| + n + 1)!} \sum_{s=0}^n (-1)^s \binom{n}{s} \times \\ & \binom{2|q| + n}{|q| + n - m - s} \left( \frac{\partial}{\partial u_j} \right)^{|q| + m + s} u_j^s \left( \frac{\partial}{\partial v_j} \right)^{|q| - m + n - s} v_j^{n-s} J_j. \end{aligned} \quad (5.7)$$

Using this they demonstrated that also the reverse flux Jain-Kamilla projected CF states are good trial wavefunctions. The extra powers in the derivatives make these expressions more computationally intensive than the corresponding positive flux ones, however. This limits the accessible system sizes in practical computations.

The situation was improved by Davenport and Simon by rewriting 5.7 and letting the derivatives act [20]:

$$\begin{aligned} \eta_{n,m,j}^{-|q|} = & \mathcal{N}_{qnm} (-1)^n \frac{(N_\Phi + 1)!}{(N_\Phi - 2|q| + n + 1)!} \prod_{k \neq j} u_k \sum_{s=0}^n \binom{n}{s} \binom{2|q| + n}{q + m + s} \\ & \sum_{t=|q| + m + s}^{N_e - 1 - |q| + m - n + s} e_t^j (-1)^t \frac{(N_e - 1 - t)!}{(N_e - 1 - t - |q| + m - n + s)!} v_j^{N_e - 1 - t - |q| + m} \\ & \frac{t!}{(t - |q| - m - s)!} u_j^{t - |q| - m}, \end{aligned} \quad (5.8)$$

with the elementary symmetric polynomials

$$e_t^j(z_{k \neq j}) = \begin{cases} \sum_{0 < i_1 < i_2 < \dots < i_t \leq N_e}^{i_k \neq j} z_{i_1} \cdots z_{i_t} & : t \leq N_e \\ 0 & : t > N_e \end{cases}, \quad (5.9)$$

in terms of the stereographic coordinates  $z_k = v_k/u_k$ . They constructed an ef-

efficient algorithm for computing the wavefunctions using the recursive relations

$$\begin{aligned} e_t^j(z_{k \neq j}) &= \frac{1}{t} \sum_{r=1}^t (-1)^{r+1} p_r(z_{k \neq j}) e_{t-r}(z_{k \neq j}) \\ e_t^j(z_{k \neq j, l}) &= e_t^j(z_{k \neq j}) - z_l e_{t-1}^j(z_{k \neq j, l}) , \end{aligned} \quad (5.10)$$

where we have the power sum polynomials  $p_r(x_k) = \sum_i x_i^r$ .

For reverse flux states this algorithm is faster than the one described in 5.1.2, but there is an issue because as electron  $k$  moves towards the south pole we have

$$z_k \xrightarrow{\theta_k \rightarrow \pi} \infty . \quad (5.11)$$

To circumvent the resulting numerical precision issues one can employ high precision variables and let the memory per coordinate be dynamically determined from the configurations, but this slows down the computations considerably.

### New algorithm for reverse flux

In our code, we eliminated the need for high precision variables in (5.8) by rewriting the expression in terms of  $u_k$  and  $v_k$  exclusively. Note that

$$\prod_{k \neq j} u_k e_t^j(\{z_{k \neq j}\}) = \sum_{i_1, \dots, i_t \neq j} \left( \prod_{k \neq j, i_1, \dots, i_t} u_k \right) v_{i_1} \cdots v_{i_t} , \quad (5.12)$$

of which one example when  $N_e = 4$  and  $j = 2$  would be

$$\begin{aligned} t = 0 &\rightarrow u_1 u_3 u_4 \\ t = 1 &\rightarrow u_1 u_3 v_4 + u_1 v_3 u_4 + v_1 u_3 u_4 \\ t = 2 &\rightarrow u_1 v_3 v_4 + v_1 u_3 v_4 + v_1 v_3 u_4 \\ t = 3 &\rightarrow v_1 v_3 v_4 \end{aligned} . \quad (5.13)$$

An algorithm that computes these can be constructed as follows:

- For  $0 \leq j \leq N_e$ , define  $f_{t,0}^j = \begin{cases} 1 & : t = 0 \\ 0 & : t \neq 0 \end{cases}$ .

- Iterate  $n$  from 1 to  $N_e$  and set

$$f_{t,n}^j = \begin{cases} f_{t,n-1}^j & : n = j \\ f_{t,n-1}^j u_n & : n \neq j \text{ and } t = 0 \\ f_{t,n-1}^j u_n + f_{t-1,n-1}^j v_n & : n \neq j \text{ and } t > 0 \end{cases} .$$

- Finally we have  $\prod_{k \neq j} u_k e_t^j = f_{tN}^j$ .

Although this algorithm uses computation time of order  $\mathcal{O}(N_e^3)$  while the one outlined in (5.10) uses  $\mathcal{O}(N_e^2)$ , this proves to be much faster in testing because high precision variables are no longer necessary. It has been brought to our attention that Mukherjee and Mandal have arrived upon the same algorithm [21], presented in their study of the plateaus  $\nu = \frac{4}{13}$ ,  $\frac{5}{17}$  and  $\frac{3}{10}$ .

### 5.1.3 Energy projection

The Jain-Kamilla projection facilitates computation of many favourable trial wavefunctions but also has some adverse properties. It projects to the lowest Landau level in an uncontrolled manner; a clear understanding of its inner workings is lacking. In particular it is not an orthogonal projection, as can be seen by noting that the orthogonal projection is unique and comprised by (5.1). This means that wavefunctions that only differ by unphysical components in higher Landau levels are projected to different states.

Moreover there are many states for which Jain-Kamilla projection is not applicable and no practical method of lowest Landau level projection exists. Examples of this include modified states (defined in section 5.5) and all states on the torus requiring projection, where the JK approximation is ruled out [110].

Therefore a more general and controlled approach to projection is desirable. In this section we develop such a method, viable for systems up to sizes that are amenable to exact diagonalisation, and demonstrate its effectiveness. The procedure is also presented in ref. [22].

#### Method

We express the projected wavefunction in terms of the lowest Landau level eigenstates  $|k\rangle$  of a suitable Hamiltonian:

$$\mathcal{P}_{LLL}\Psi \approx \sum_{k=1}^M c_k |k\rangle, \quad (5.14)$$

where  $M$  is a chosen cutoff and the coefficients are found as

$$c_k = \frac{\langle k|\Psi\rangle}{\sqrt{\sum_{j=1}^M |\langle j|\Psi\rangle|^2}}. \quad (5.15)$$

In cutting off at  $k = M$  and normalising the coefficients  $c_k$  we approximate the LLL content of  $\Psi$  that is not captured in (5.14) to be negligible. This can be

## 5.1. LOWEST LANDAU LEVEL PROJECTION

achieved by using a sufficiently high  $M$  and choosing a Hamiltonian with which the overlaps with  $\Psi$  fall off rapidly with  $k$ ; usually the Coulomb potential is a natural choice. Note that the approximation is completely controlled through the parameter  $M$ , and that using all the eigenstates yields the exact projection.

We define the quantity

$$f = |\langle \Psi | \mathcal{P}_{LLL} \Psi \rangle|^2 = \sum_{k=1}^M |c_k|^2 \quad (5.16)$$

as the total lowest Landau level content bar the cutoff. The average size of the coefficients then depends on this as

$$|c_j| \sim \frac{\sqrt{f}}{M}, \quad (5.17)$$

giving an approximate norm of the projected wavefunction as

$$|\mathcal{P}_{LLL} \Psi| = \sqrt{\sum_{k=1}^M |c_k|^2} \sim \sqrt{f}. \quad (5.18)$$

It is pertinent to have a rough estimate of the necessary computational effort for the projection. The diagonalisation needed to obtain the  $M$  eigenstates is generally not the bottleneck of the calculations and will be ignored. We approximate the errors  $\delta_k$  on  $|c_k|$  to be independent and equal (neither of which are true, but this is sufficient for our purposes). The Monte Carlo error  $\mathcal{E}_\Psi$  on  $|\mathcal{P}_{LLL} \Psi|$  can then be estimated using error propagation with (5.14):

$$\mathcal{E}_\Psi \sim \sqrt{\sum_{k=1}^M \delta_k^2} \sim \epsilon \sqrt{M}. \quad (5.19)$$

As a benchmark we impose an upper bound of order  $\sqrt{f}$  on  $\mathcal{E}_\Psi$ . Using (4.4) this gives for the required number of MC samples

$$N_{MC} \sim \frac{1}{\epsilon^2} \sim \frac{M}{f}. \quad (5.20)$$

The size of the full Hilbert space, i.e. the number of Fock states, is given by  $\binom{N_\Phi}{N_e}$ , while evaluation of determinants is generally requires order  $\sim \mathcal{O}(N_e^3)$  computations. Therefore we estimate the amount of calculations necessary to compute all the real space Slater determinants to be of order  $\sim N_e^3 \binom{N_\Phi}{N_e}$ . As seen in section 4.1 this is an overestimate: in practice there are usually ways

to limit the Fock space, sometimes dramatically, using symmetries – e.g. by restricting to an  $(\widehat{L}^2, \widehat{L}_z)$ -subspace corresponding to that of  $\Psi$ .

The Fock states can be reused in computing the  $M$  energy eigenstates. Requiring  $\sim N_e$  Monte Carlo steps between each sample, as argued in section 4.2.1, gives a total number of necessary computations  $n$  in order to attain  $\mathcal{E}_\Psi \sim \sqrt{f}$  as

$$n \sim N_e(N_e^3 + M) \binom{N_\Phi}{N_e} N_{MC} \sim N_e M(N_e^3 + M) \binom{N_\Phi}{N_e} f^{-1}. \quad (5.21)$$

This limits the sizes that can be reached, but as we will see still allows scrutiny of many novel and untested states.

The results using energy projection in later sections are all obtained using the Coulomb Hamiltonian and  $M = 100$  eigenstates, except for the cases where the relevant lowest Landau level subspace is smaller than this, in which case it is not cut off and there is no approximation (only MC error).

One might ask whether, if construction of LLL Fock states and real space overlaps with these are viable, it is not better to project by expressing the wavefunction as a superposition of the Fock states themselves and thus avoid diagonalisation altogether. This turns out to be much less efficient, however. The main reason for this is that the Coulomb ground states, and thus also accurate trial wavefunctions, have comparable overlaps with a significant fraction of the Fock states; the individual overlaps are small.

Even if this was not the case there is no natural cutoff point in the Fock space. Therefore we assume use of the full Hilbert space of size  $\binom{N_\Phi}{N_e}$ . Performing a similar analysis to the one preceding (5.21) shows that the number of samples needed to get an error  $\mathcal{E}_\Psi$  of the same order as the norm of the result is  $n \sim N_e^4 \binom{N_\Phi}{N_e}^2 f^{-1}$ . With  $M$  comparatively small and the binomial coefficient growing exponentially with  $N_e$ , this  $n$  is in general much larger than the corresponding number (5.21) for energy projection.

### Testing the method

To minimise the error involved in cutting off the Hilbert space at  $M$ , the size of the overlaps  $\langle \psi | \phi_n \rangle$  with the eigenstates  $\phi_n$  of the chosen Hamiltonian should decrease rapidly with  $n$ . To test this we find overlaps between the eigenstates and the Laughlin wavefunction (section 3.2.1) and the composite fermion ground state wavefunction (section 3.3.1), with modification factors parametrised by the scalar  $d$ . These factors are introduced in section 5.5 and

## 5.1. LOWEST LANDAU LEVEL PROJECTION

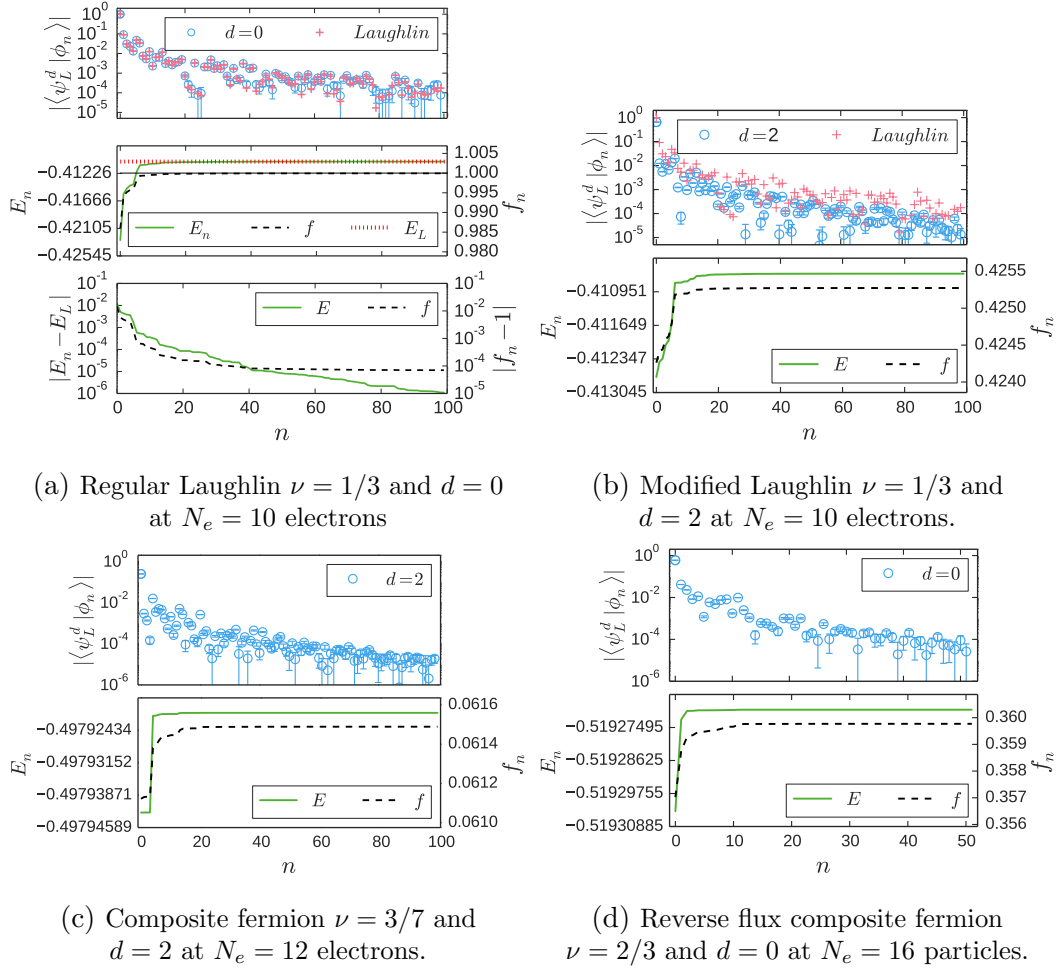


Figure 5.1: Measure of the effectiveness of the energy projection. The upper panels show squared overlaps between trial wavefunctions and Coulomb eigenstate  $n$ . The middle panel of (a) and the lower panels of (b), (c) and (d) give the saturation of energy  $E$  and LLL content  $f_n = |\langle \Psi | \mathcal{P}_{LLL} \Psi \rangle|^2$  with number of included states  $n$ . Note that we expect  $f \rightarrow 1$  for states completely contained in the LLL and  $f < 1$  otherwise. The lower panel of (a) shows the saturation of  $E$  and  $f$  relative to  $E_L$  and 1 respectively (in log scale). In this context ‘Laughlin’ refers to exact values from diagonalising the hardcore potential and  $E_L$  is its energy.

take the form

$$\Psi_d = \Psi \prod_{i < j} |z_i - z_j|^{2d}, \quad (5.22)$$

where  $\Psi$  is the unmodified wavefunction. This introduces additional components in higher Landau levels. The upper panels of figure 5.1 show the absolute squared overlaps for a chosen set of states, using the lowest Landau level Coulomb Hamiltonian.

Figures 5.1a and 5.1b display the Laughlin state at  $\nu = 1/3$  with modification factor  $d$  equal to 0 and 2 respectively (see section 5.5). In the former case the true overlaps can be obtained to machine precision using diagonalisation of the hardcore potential (section 2.1.2) and these are also displayed,

labelled ‘Laughlin’. For  $d = 0$  this is a test of the Monte Carlo estimate and for  $d = 2$  it shows that the overlaps decrease with  $d$ , which is natural since the LLL content does as well. In figures 5.1c and 5.1d we see the overlaps for two composite fermion states, the former with a modification factor  $d = 2$ . It is evident in all of the plots that the overlaps decrease quickly with  $n$  (note the log scale).

Another measure of the error due to the cutoff is shown in the second panels of figure 5.1; namely the saturation of Coulomb energy  $E_n$  and total lowest Landau level content  $f_n$  with the number  $n$  of eigenstates included. It is clear that the values stabilise very quickly.

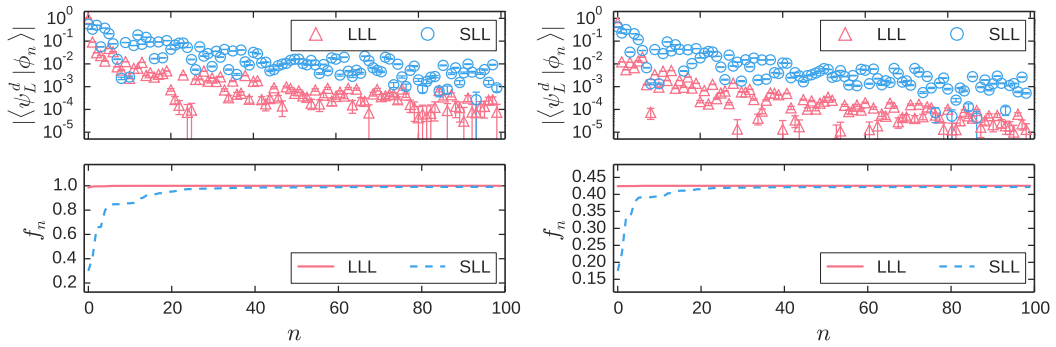
In the case of the regular Laughlin state at  $d = 0$ , the energy is known to machine precision from diagonalisation, and since it is fully in the LLL we have  $f = 1$ .  $E_n$  and  $f_n$  are compared to these values in the last panel of figure 5.1a in a log scale plot, and again the saturation with  $n$  is rapid. Note that  $f_n - 1$  reaches an approximate plateau around  $10^{-4}$  where almost all of the wavefunction is contained in the previous eigenstates and adding more states only gives a miniscule increase. These eigenstates have high energy eigenvalues, however, which explains why there is no corresponding plateau in the energy  $|E_n - E_L|$ .

It is desirable that the precise choice of Hamiltonian not be crucial for the energy projection, implying that the method is general. It is known that the regular Laughlin wavefunctions are not good trial wavefunctions for the second Landau level Hamiltonian, which has very different properties than the lowest level; making it a suitable comparison. The upper panels of Figure 5.2 contrast absolute squared overlaps with eigenstates from the lowest and second Landau level.

As expected the overlap with SLL states does not decrease as rapidly as that with LLL functions. However it is still fast enough for the energy projection to remain viable. This is emphasised in the lower panels, which show the saturation of  $E$  and  $f$  with number of included states. A stable value is approached within relatively few states.

In closing we note that the energy projection can possibly be used for other purposes than lowest Landau level projection, e.g. explicit symmetrisation or antisymmetrisation, as is necessary when using for example CFT generated hierarchy states and excited states of the Moore-Read wavefunction (see section 3.4.2). In addition, in reference [22] we demonstrate that the approach works just as well on the torus, where a projection method is especially in demand.

## 5.2. QUANTITIES TO BE COMPUTED



(a) Regular Laughlin  $\nu = 1/3$  and  $d = 0$   
at  $N_e = 10$  electrons

(b) Modified Laughlin  $\nu = 1/3$  and  
 $d = 2$  at  $N_e = 10$  electrons.

Figure 5.2: Comparison of overlaps with lowest and second Landau level eigenstates. The upper panels give the absolute squared overlaps while the lower panels give the accumulative LLL content  $f_n$ .

## 5.2 Quantities to be computed

In this section we expound upon the quantities that will be studied for different wavefunctions in the following sections.

### 5.2.1 Energy spectra

The Coulomb interaction energy (2.6) is straightforward to compute by Monte Carlo but does not have a well defined thermodynamic limit, increasing without bounds as  $N_e \rightarrow \infty$ . In order to facilitate interpolation we divide by the number of particles and add the energy resulting from a constant neutralising background, which on the sphere is given by [3]

$$V_{bb} + V_{eb} = -\frac{N_e}{2R}. \quad (5.23)$$

The index ‘ $bb$ ’ stands for the interaction of the background with itself and ‘ $eb$ ’ for that between the electrons and the background. The resulting energy densities usually have an approximately linear evolution with  $1/N_e$ . This division by  $N_e$  followed by background energy subtraction is performed for all energies in the following sections; which are usually denoted simply by ‘ $E$ ’ in the plots. The values are given in units of  $\frac{e^2}{\epsilon\ell}$ .

In addition, since the electron density  $\rho$  is size dependent through the spherical shift (2.36) and the energy is proportional to  $\rho^{1/2}$ , we sometimes apply the following correction to further linearise the behaviour:

$$E \longrightarrow E \sqrt{\frac{\rho_\infty}{\rho_N}} = E \sqrt{\frac{\nu N_\Phi}{N_e}}. \quad (5.24)$$

This shifts the individual values without impacting the limit. In the following sections this is applied whenever scaling to the thermodynamic limit is desired, and indicated in the text.

Sometimes we are concerned with the energy spectrum of a space of trial wavefunctions rather than a single one, for example when considering excitations where there are several states in the same energy band (see the next paragraph) and at the same angular momentum numbers  $L$  and  $M$ , as defined in (2.30). We will be dealing mostly with variations of the composite fermion wavefunctions, and therefore describe how to deal with these (see also section 5.8.4 and chapter 6 of ref. [3]):

Energy band in this context refers to the energy of the CF trial state before flux attachment and LLL projection, i.e. the occupation of the CF Landau levels. The computed energy of the final state is not fully determined by its band due to the effects of flux attachment and projection, but varies with angular momentum  $L$ . This variation is often small enough, however, that bands separated by finite gaps can be observed also in the final results.

In some cases it is possible to pick out approximate energy bands also in the exact spectrum computed by diagonalisation. For incompressible states there is usually one clear band above the ground state, corresponding to a single exciton, and sometimes more. For compressible states, e.g. a single quasihole or quasielectron, there is generally a clear lowest band. With increasing numbers of quasiparticles the bands become less defined as one would expect. Therefore a comparison between the number of states in the trial state energy bands and in the tentative exact bands comprises a qualitative test of the model.

The single-determinant excited states (3.10) are automatically eigenstates of  $\widehat{L}_z$  but not of  $\widehat{L}^2$ , which we need in order to compare to exactly diagonalised spectra. Therefore we construct superpositions  $|L, M, k\rangle$  using Clebsch-Gordan coefficients. The index  $k$  differentiates between distinct states with the same angular momentum. To find states with a given value  $L$ , we first identify all the single-determinant states with  $M = L$ , denoted  $|M = L, j\rangle$ . Then we compute the nullspace of the raising operator  $\widehat{L}_+ = \widehat{L}_x + i\widehat{L}_y$  within this space:

$$|L, L, k\rangle \in \{\ker(\widehat{L}_+) : |M = L, j\rangle\} . \quad (5.25)$$

States  $|L, M, k\rangle$  with general angular momenta can then be found using the lowering operators  $\widehat{L}_- = \widehat{L}_x - i\widehat{L}_y$ :

$$\widehat{L}_-|L, M, k\rangle = \sqrt{(L+M)(L-M+1)}|L, M-1, k\rangle . \quad (5.26)$$

Constructing the null states  $|L, L, k\rangle$  involves an arbitrary choice of basis for  $\ker(\widehat{L}_z)$ , however, and it is not clear a priori how to choose a good set of trial wave functions for energy eigenstates. Such can be obtained, however, by diagonalising the Coulomb Hamiltonian within the space of states spanned by  $|L, M, k\rangle$  for all  $k$  at the chosen  $(L, M)$ .

### Diagonalisation within a trial state space

Firstly the superpositions  $|L, M, k\rangle$  are not in general linearly independent, or even nonzero, due to dependencies introduced through flux attachment and projection. To identify the number of independent states we count the number of nonzero eigenvalues of the overlap matrix

$$G_{jk} = \langle L, M, j | L, M, k \rangle . \quad (5.27)$$

The number of independent states is in itself a nontrivial measure of whether the trial wavefunction scheme is a good one. We start out with an overly high number of states that is then reduced through a procedure after which the resulting number is hard to predict; hopefully ending up with the same number of states as in the tentative exact energy band (where such can be identified). It has been demonstrated that this works well for regular flux composite fermions [67, 69]. There is a caveat in that due to Monte Carlo error and approximative projection the overlap matrix (5.27) usually does not have any eigenvalues exactly equal to zero, but there is generally a clear break between a set of small and large eigenvalues respectively [90].

We use an orthogonal basis, constructed using the Gram-Schmidt procedure. The Hamiltonian is then diagonalised after finding its matrix elements in the orthogonal basis, resulting in the states

$$|L, M, j\rangle_E , \quad (5.28)$$

with  $E$  for energy eigenstate.

A final consideration comes from the fact that states with the same angular momentum numbers  $(L, M)$  but different composite fermion bands also can be linearly dependent. One approach would be to do the diagonalisation separately in each band, but this means that variational energies sometimes can be lower than the exact ones. This happens because, although the trial states are orthogonal after the Gram-Schmidt procedure, also between bands, the states in higher CF bands will not be orthogonal to the exact lower states.

Therefore we believe it is clearer to orthogonalise within the space of all states for each set of quantum numbers  $(L, M)$ , independent of composite fermion energy bands. The number of states depends on how many bands we include. This results in variational energies which are always higher than the exact ones. To confirm that this choice not significantly impact the outcome we compare to the results from diagonalising within each band in section 5.3.1.

### 5.2.2 Eigenstate overlaps

Another measure of the quality of a trial wavefunction is the overlap with eigenstates  $|\xi_i\rangle$  obtained through exact diagonalisation. We find the wavefunctions (5.25) and take the overlap  $\langle \xi_i | L, M, k \rangle_E$  with the exact states at the corresponding quantum numbers and energy band. When there are several wavefunctions in the same band with the same quantum numbers we use states (5.28) obtained through diagonalisation of the Hamiltonian and use the geometric mean of the overlaps as a measure. This can be computed as [67]

$$\prod_{i,j=1}^S \langle \xi_i | L, M, j \rangle_E^{1/S} = \text{Det}[\langle \xi_i | L, M, k \rangle]^{1/S}, \quad (5.29)$$

where  $S$  is the number of states in the subspace. Note that the right hand side of (5.29) uses the state (5.25) before diagonalisation (no subscript  $E$ ), which simplifies the calculation. We consistently report the absolute squares of the overlaps and geometric means.

### 5.2.3 Pair correlation functions

A plot of the pair correlation  $g(r)$  (2.39) given a real space wavefunction  $\Psi$  can be obtained in a straightforward manner. Approximating  $g(r)$  using averages  $\bar{g}_i$  over bins  $[r_i, r_{i+1}]$  and taking the mean over all electron pairs  $j$  and  $k$  yields the Monte Carlo estimate

$$\bar{g}_i = \frac{\int_{r_i}^{r_{i+1}} dS_r g(r_{12})}{\int_{r_i}^{r_{i+1}} dS_r} \approx \frac{2 \sum_m \frac{|\tilde{\Psi}|^2}{P} \left( \sum_{j < k} [H_i(r_{jk}) - H_{i+1}(r_{jk})] \right) \Big|_m}{A_i N_e \rho \sum_m \frac{|\tilde{\Psi}|^2}{P} \Big|_m}, \quad (5.30)$$

over MC samples  $m$  drawn from probability  $P$  (see section 4.2). Note that the factors  $N_e(N_e - 1)$  in (2.39) are cancelled by the number of pairs in the mean, i.e.  $N_e(N_e - 1)/2$ . We have defined the area  $A_i$  of bin  $i$ , the average density of

the whole system is  $\rho$ , and we use the Heaviside step function

$$H_i = \begin{cases} 0 & : r < r_i \\ 1 & : r \geq r_i . \end{cases} \quad (5.31)$$

The fact that we are taking the mean over all electron pairs means that each Monte Carlo sample contributes  $\sim N_e^2$  data points, which improves the statistical convergence. Note that a single term in the numerator of (5.30) amounts to counting how many pairs are separated by a distance corresponding to bin  $i$ .

## 5.3 Reverse flux composite fermions

The ground state energies, exciton gaps and dispersions of reverse flux composite fermion states are investigated in [19, 20], and we focus here on other states and properties. This includes more general energy spectra and overlaps with exactly diagonalised eigenstates. We also perform a comparison between the Jain-Kamilla and energy projections.

### 5.3.1 Energies

With the fast algorithm for reverse flux composite fermion states constructed in section 5.1.2 we probe the excitation spectrum of several systems, in a similar way to what has been done for positive flux states in [67–69]. Both the Jain-Kamilla projection and the energy projection are employed to see what effect the former has on the wavefunctions; the results are in figure 5.3.

Also in the figures are spectra obtained from exact diagonalisation of the Coulomb Hamiltonian. These are colored alternately red and blue in accordance with composite fermion energy bands (i.e. with the number of states in consecutive bands for each  $L$ ) to aid the comparison.

The figures 5.3a and 5.3b correspond to incompressible ground states and their neutral excitations in the form of one and two excitons, at  $n = 2$  and 3 filled Landau levels respectively (i.e. at filling factors  $\nu = 2/3$  and  $3/5$ ). The figures 5.3c, 5.3d, 5.3e and 5.3f show charged excitations in the form of quasielectrons and quasiholes together with one band of excitons. This marks the first time charged excitations, relevant for conductance measurements, have been studied for reverse flux states.

The first thing to note is that, similarly to regular flux composite fermions

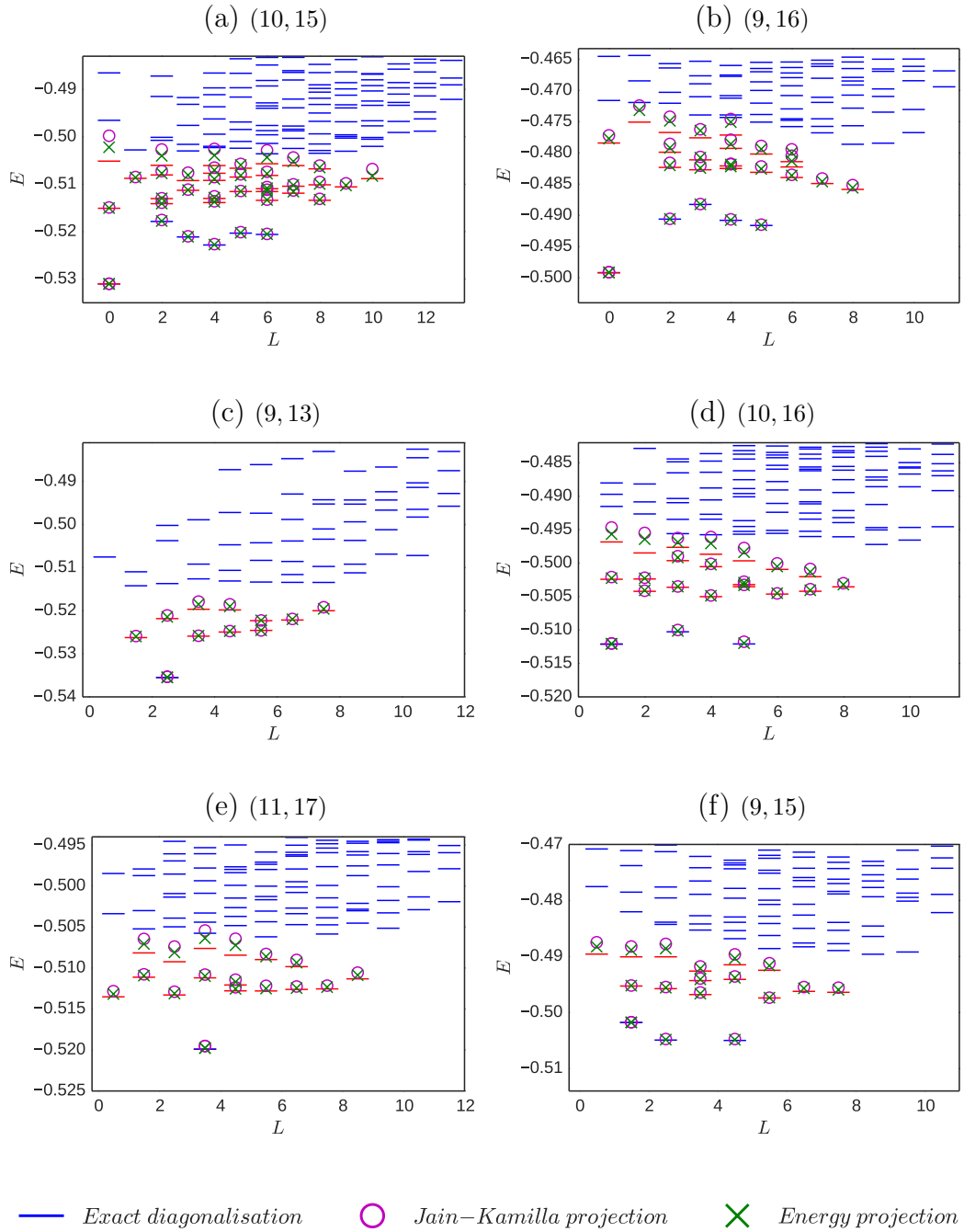


Figure 5.3: Exact Coulomb energy spectra at various sizes and filling factors together with variational spectra of corresponding CF trial wave functions, using Jain-Kamilla and energy projection. The figure subtitles give the parameters  $(N_e, N_\Phi)$ ; the states can be interpreted as (a)  $\nu = 2/3$ , (b)  $\nu = 3/5$ , (c)  $\nu = 2/3$  with one quasihole, (d)  $\nu = 2/3$  with two quasiholes, (e)  $\nu = 2/3$  with two quasielectrons and (f)  $\nu = 2/3$  with three quasielectrons or  $\nu = 3/5$  with three quasiholes. States of the exact spectra have been colored blue and red alternatingly in correspondence with CF energy bands. The MC errors are invisible on the scale of the figures.

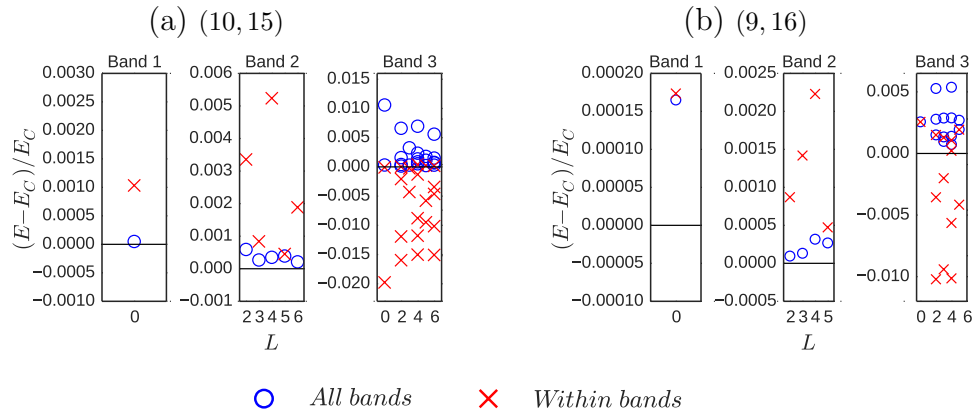


Figure 5.4: Relative difference between variational energy  $E$  and Coulomb energy  $E_C$  when the diagonalisation is performed on Jain-Kamilla projected states of angular momentum  $L$  using all bands (blue circles) and within each band (red crosses). Subtitles give the parameters  $(N_e, N_\Phi)$ ; the states are (a)  $\nu = 2/3$  and (b)  $\nu = 3/5$ .

and simpler reverse flux states, the trial wavefunctions are good in the sense that they fit the low lying spectrum well. The numbers of states produced by the trial wavefunctions match those of the exact spectrum, to the extent that the exact bands can be distinguished. Quantitatively the numerical values are close, especially for the lower energy states.

Since the Hamiltonian is diagonalised within the space of all states with the same angular momenta  $(L, M)$  one could argue that this mainly shows that lower energy states of the trial states as a collection are accurate; as a test on individual states or CF energy bands we also perform the diagonalisation within each band.

A comparison between these two methods is shown in figure 5.4, with plots of  $(E - E_C)/E_C$  for the two incompressible states in figure 5.3.  $E$  is the energy from the diagonalised trial states and  $E_C$  is the eigenvalue of the Coulomb Hamiltonian. We see that the difference between the two methods is relatively small; diagonalising within each band gives slightly less accurate energies but they are still matching to within a few percent. As mentioned in section 5.2.1 the latter are lower than the Coulomb energy when there are states at lower bands but the same  $(L, M)$ . Finally it should be noted as a minimal check that the states of higher CF bands never have energies below those of lower bands; the order of bands is intact (excepting the states which through overlaps prove to actually reside in the lower bands, see the discussion below (5.28)).

Since the ground states and single excitons of reverse flux states are known to perform well [19, 20], the same was expected of the fuller spectra. But it is informative to test this as in the above, especially in light of the fact that the states before projection have increasing components in higher Landau levels

as one implements higher excitations. This makes the projection more severe, and especially so for reverse flux states.

Another aim with this data is a test of the Jain-Kamilla projection as compared to the exact projection. The latter is possible since in these cases the energy projection is exact up to MC error as the full space of energy eigenstates has been used in the expansion (i.e. there is no cutoff). We observe that the variational energy of the Jain-Kamilla projected state is always higher but very close to the full projection, and on the scale in the plot they are often identical. But the difference is significant and grows with higher excitations, in conjunction with the increasing wavefunction content in higher Landau levels and corresponding complexity of the projection. This marks the first time the Jain-Kamilla projection has been tested to this extent.

There are examples, however where Jain-Kamilla projected states yield lower variational energies than their energy projected counterparts. Some examples of this are seen in sections 5.4 and 5.5.3 below.

### 5.3.2 Overlaps

The overlap between a trial state and the exact eigenstate carries information distinct to that of the Coulomb energy, which depends on the overlaps with all the states within the relevant subspace and the Coulomb eigenvalues. Table 5.1 lists the overlaps for states corresponding to those in figure 5.3.

The overlaps again indicate that the reverse CF trial states match the exact system to a high degree. The Jain-Kamilla projected states are close to the energy projected ones, with the latter always having a slightly higher overlap. This effect is stronger for higher energy states which have more content in higher Landau levels. These considerations support the conclusions drawn from examining the energy spectra.

In addition we note that for higher band states, the lower  $L$  wavefunctions are often those with the smallest overlaps. This is also reflected in the variational energies. This is probably because these represent states where the fundamental excitations (quasiholes and quasielectrons) have a higher probability of being closer together, and interactions between them play a bigger role – while these interactions are neglected in the regular CF model. It is possible to also take these into account using interactions between composite fermions [111]. This effect is not completely unequivocal, however, as evidenced by the fact that the decrease in overlap is not monotonic.

## 5.3. REVERSE FLUX COMPOSITE FERMIONS

(a) (10,15)				(b) (9,16)					
Band	L	$\mathcal{O}_{JK}^2$	$\mathcal{O}_{EP}^2$	Band	L	$\mathcal{O}_{JK}^2$	$\mathcal{O}_{EP}^2$		
1	0	0.97470(3)	0.9881(3)	1	0	0.997120(3)	0.9987(2)		
	2	0.8290(2)	0.882(2)		2	2	0.97193(2)	0.9830(7)	
	3	0.96595(4)	0.979(1)			3	0.93118(5)	0.9542(7)	
	2	4	0.95328(6)			0.9736(8)	4	0.92257(8)	0.9486(7)
		5	0.98727(2)			0.9950(10)	5	0.98844(1)	0.9937(6)
		6	0.9168(1)		0.950(1)	3	0	0.8450(1)	0.905(2)
3	0	0.7776(4)	0.8685(8)	1	0.6931(3)		0.726(2)		
	1	0.96289(5)	0.971(2)	2	0.8618(1)		0.8945(5)		
	2	0.8385(2)	0.8838(8)	3	0.90250(9)		0.9233(9)		
	3	0.9021(1)	0.929(1)	4	0.8487(1)		0.8839(6)		
	4	0.8687(2)	0.9079(7)	5	0.9145(1)		0.9382(7)		
	5	0.9382(1)	0.946(3)	6	0.8884(2)		0.9174(5)		
	6	0.9052(2)	0.9401(4)	7	0.9572(1)		0.978(1)		
	7	0.9198(2)	0.9483(5)	8	0.97651(6)	0.977(1)			
	8	0.9649(5)	0.9763(4)						
	9	0.9502(1)	0.971(2)						
10	0.9126(3)	0.941(2)							

(c) (9,13)				(d) (10,16)			
Band	L	$\mathcal{O}_{JK}^2$	$\mathcal{O}_{EP}^2$	Band	L	$\mathcal{O}_{JK}^2$	$\mathcal{O}_{EP}^2$
1	2.5	0.97230(3)	0.9866(6)	1	1	0.97285(3)	0.9834(9)
	1.5	0.96685(6)	0.980(3)		3	0.89744(10)	0.9298(10)
	2.5	0.92390(9)	0.956(4)		5	0.97480(3)	0.9863(6)
	3.5	0.9075(3)	0.9403(5)	2	1	0.8590(3)	0.915(1)
2	4.5	0.9256(4)	0.9541(4)		2	0.8428(4)	0.8925(8)
	5.5	0.9920(3)	0.9957(5)		3	0.8859(5)	0.9195(8)
	6.5	0.97562(4)	0.984(1)		4	0.8799(1)	0.9139(10)
	7.5	0.9358(1)	0.963(2)		5	0.8939(3)	0.9216(9)
					6	0.9587(2)	0.9752(9)
			7		0.9286(1)	0.9541(8)	
			8		0.94937(5)	0.965(2)	

(e) (11,17)				(f) (9,15)			
Band	L	$\mathcal{O}_{JK}^2$	$\mathcal{O}_{EP}^2$	Band	L	$\mathcal{O}_{JK}^2$	$\mathcal{O}_{EP}^2$
1	3.5	0.95701(3)	0.9774(6)	1	1.5	0.8779(1)	0.9192(10)
	0.5	0.94536(6)	0.968(1)		2.5	0.98241(2)	0.9928(6)
	1.5	0.8330(2)	0.8711(7)		4.5	0.98291(2)	0.9901(4)
	2.5	0.8633(1)	0.9042(8)	2	0.5	0.8400(2)	0.900(3)
	3.5	0.8136(1)	0.859(1)		1.5	0.8362(1)	0.890(1)
2	4.5	0.88378(10)	0.9229(8)		2.5	0.8694(1)	0.916(1)
	5.5	0.94891(6)	0.9708(9)		3.5	0.95572(5)	0.9757(6)
	6.5	0.94118(7)	0.9658(8)		4.5	0.8763(1)	0.9196(7)
	7.5	0.96751(3)	0.980(1)		5.5	0.93292(8)	0.9552(8)
	8.5	0.92969(9)	0.959(2)		6.5	0.93745(7)	0.954(1)
			7.5	0.94391(6)	0.966(1)		

Table 5.1: Squared ground state overlaps (geometric means of overlaps where applicable). Subtitles give the parameters  $(N_e, N_\Phi)$ ; the states can be interpreted as (a)  $\nu = 2/3$ , (b)  $\nu = 3/5$ , (c)  $\nu = 2/3$  with one quasihole, (d)  $\nu = 2/3$  with two quasiholes, (e)  $\nu = 2/3$  with two quasielectrons and (f)  $\nu = 2/3$  with three quasielectrons or  $\nu = 3/5$  with three quasiholes.

## 5.4 Bonderson-Slingerland

Reference [95] contains numerical investigations of the  $\nu = 12/5$  Bonderson-Slingerland ground state (3.14), but as yet no study of the excited states has been performed. The left column of figure 5.5 (labelled  $\delta V_1 = 0$ ) shows the exact spectrum computed by diagonalisation, together with the energies of the ground state and the first band of excitons, for three system sizes.

The first excited energy band is modelled using excitations both in the composite fermion and pfaffian sectors, as described in section 3.4.3. A possible generalisation of this would be to diagonalise the Hamiltonian in the space of both kinds of excitations; this is not attempted here. Both Jain-Kamilla and energy projection is utilised.

Since we need the phase of the wavefunction for overlaps, the identity  $|\text{Pf}(M)| = |\sqrt{\text{Det}(M)}|$  is not sufficient to compute the pfaffian ground state, and we have implemented the algorithm in ref. [112] to compute the pfaffian factors. For excited Moore-Read components a recursive algorithm is utilised to symmetrise the two composite fermion states.

As indicated in section 2.2.4, it is not trivial to obtain an estimate for the variational Coulomb energy when using lowest Landau level wavefunctions to model second Landau level states. A common strategy is to use an effective interaction whose pseudopotentials evaluated in the LLL equal those of the Coulomb potential evaluated in the SLL. Such an interaction has so far only been constructed for planar wavefunctions [39,40], however, giving small errors in the results (although this makes no difference in the thermodynamic limit).

The energy projection offers an alternative with no use of planar functions, also for the Jain-Kamilla projected states. In the latter case the projection itself is then redundant as the states already reside completely in the lowest Landau level, but expressing them in terms of energy eigenstates makes it straightforward to compute the energy from second Landau level eigenvalues. In other words, we express the state as in (5.14), with the states  $|k\rangle$  as SLL Coulomb energy eigenstates, giving the variational energy

$$\langle E \rangle = \sum_k |c_k| \mathcal{E}_k^{SLL} , \quad (5.32)$$

where  $\mathcal{E}_k^{SLL}$  are the second Landau level Coulomb eigenvalues. After this the correction in (2.37) is applied to compensate the offset in the sphere radius.

The ground state energies in figure 5.5 are not as close to the exact eigen-

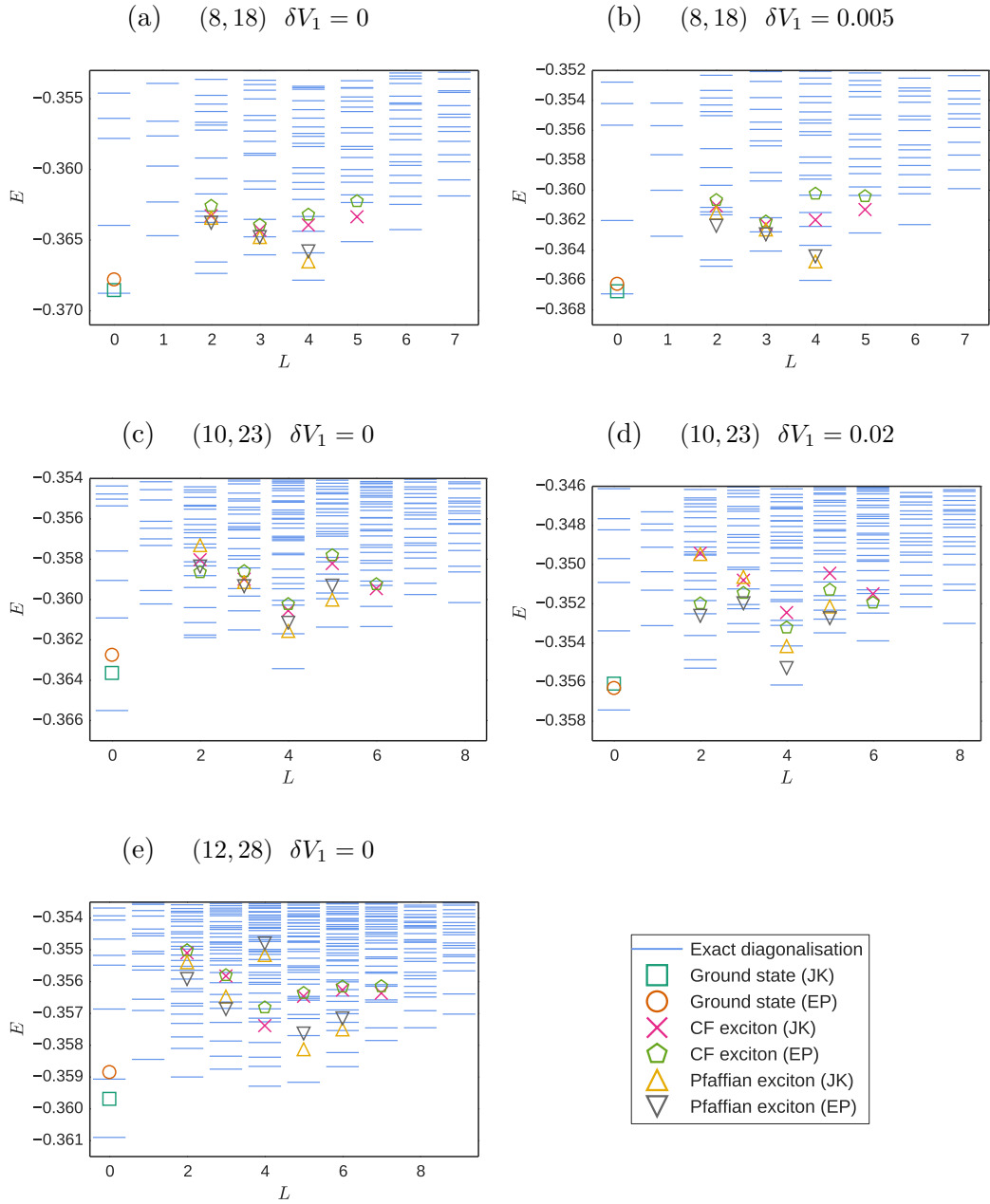


Figure 5.5: Low lying spectra of  $\nu = 12/5$  systems in the second Landau level obtained through exact diagonalisation, together with variational energies from Bonderson-Slingerland trial wavefunctions (intended to describe the lowest energy state at each  $L$ ). Data in the left column uses the pure Coulomb interaction, while the right column corresponds to a perturbation  $\delta V_1$ . The value of the perturbation is chosen to give the optimal ground state energy as per ref. [95] (note that for  $N_e = 12$  this occurs at  $\delta V_1 = 0$ ). Trial state excitations are made in both the composite fermion and pfaffian sectors, and both Jain-Kamilla projection (JK) and energy projection (EP) have been employed. Subtitles give the parameters  $(N_e, N_\Phi)$  and  $\delta V_1$ . The MC errors are invisible on the scale of the figures.

$N_e / L$	0	1	2	3	4	5	6	7	8
8	13	13	17	42	45	69	70	91	90
10	97	97	187	377	463	645	722	891	955
12	902	902	2405	4185	5662	7384	8787	10437	11741

Table 5.2: Number of multiplets at a given number of electrons  $N_e$  and angular momentum  $L$  for the Bonderson-Slingerland  $\nu = 12/5$  state. The number of magnetic flux quanta is given by  $N_\Phi = 5N_e/2 - 2$ .

values as e.g. the CF trial wavefunctions in 5.3 (note that the variational states are intended as trial wavefunctions of the lowest energy states at each  $L$ ), but still have relatively low values. This point is emphasised by considering the total number of states at angular momentum  $L = 0$ , which is displayed in the second column of table 5.2. We note that the variational energies lie between the two lowest states with the exception of the energy projected state at system size  $N_e = 12$ .

In fact the energy projected wavefunctions have higher variational energy than the Jain-Kamilla projected ones for all ground states. This is the opposite result as compared to the reverse flux composite fermion wavefunctions studied in section 5.3, although these BS states have the latter as a factor. One might question whether the same is true if the energy projection is applied to the CF factor before multiplication with the bosonic pfaffian, rather than projecting the entire state as is done here. This would require multiplication in momentum space, however, and is not attempted in this work.

Similar observations hold true for the excitons. The variational energies are not ideal matches but still relatively low when taking into account the number of states at each  $L$ , displayed in table 5.2. The excess variational energies are comparable to those of the ground states; slightly larger at low relative angular momenta where the interactions between quasiparticles (not part of this model) are expected to be the strongest. The JK projected states have lower energies than the EP ones for excitations in the composite fermion sector, while the opposite is true for pfaffian excitations.

Most interestingly, however, is the fact that the pfaffian excitons generally have lower energy than the CF versions (with a striking exception at  $L = 4$  for  $N_e = 12$  electrons). This is significant because the former have nonabelian statistics, and if the physical system should turn out to be essentially described by the Bonderson-Slingerland state, it may have consequences for experimental detection of nonabelions.

The physically realised system will in general not have the exact form

of the Coulomb Hamiltonian  $H$  (2.6) restricted to the second Landau level, due to effects from the finite width of the sample, random disorder, finite temperature and magnetic field, Landau level mixing, etcetera. One way to vary the potential away from  $H$  is to perturb the pseudopotentials; in the simplest case by varying  $\delta V_1$ , which is also the largest and thus most significant. There is no reason a priori to assume that the regular Coulomb potential yields a better description of the physical system than the altered one. Studying a trial wavefunction in the perturbed setting then corresponds to examining whether there is a region in the Hamiltonian space, close to the Coulomb potential, in which the wavefunction yields a good fit.

Such an analysis is performed in ref. [95], with the conclusion that a perturbation  $\delta V_1 = 0.005$  results in a better fit with the wavefunction at system size  $N_e = 8$ , and that  $\delta V_1 = 0.02$  does the same for  $N_e = 10$ . For  $N_e = 12$  electrons the regular Coulomb potential with  $\delta V_1 = 0$  is the optimum. The effect of the former two perturbations on the excitons are displayed in figures 5.5b and 5.5d.

It is clear that the same perturbations also yield improvements of the excited states. This is most impressive for the pfaffian excitons at  $N_e = 10$  electrons, where especially the  $L = 2$  state energy is significantly lower than at  $\delta V_1 = 0$ , and the excess variational energy is particularly small for the EP state at  $L = 4$ . We also note that for this system the energy projected ground state has a lower energy than the JK projected one.

### 5.4.1 Quasiholes

Having studied the BS wavefunctions at flux corresponding to incompressible states, we turn to quasiholes, i.e. at a relatively higher flux. One extra flux quantum is added, which corresponds to adding two quasiholes. These are realised either both in the pfaffian sector or both in the composite fermion sector (note that the latter implies adding quasielectrons in the reverse flux CF determinant).

The results, displayed in figure 5.6, are analogous those from the excitons in the previous sections. The variational energies, while a fair amount higher than the exact eigenvalues, are low compared to the entire spectrum. Generally quasiholes in the pfaffian have lower energies than those of the composite fermions, and energy projection yields better values than JK projection for the former and vice versa for the latter.

We note that the trial states with excitations in the pfaffian sector correctly

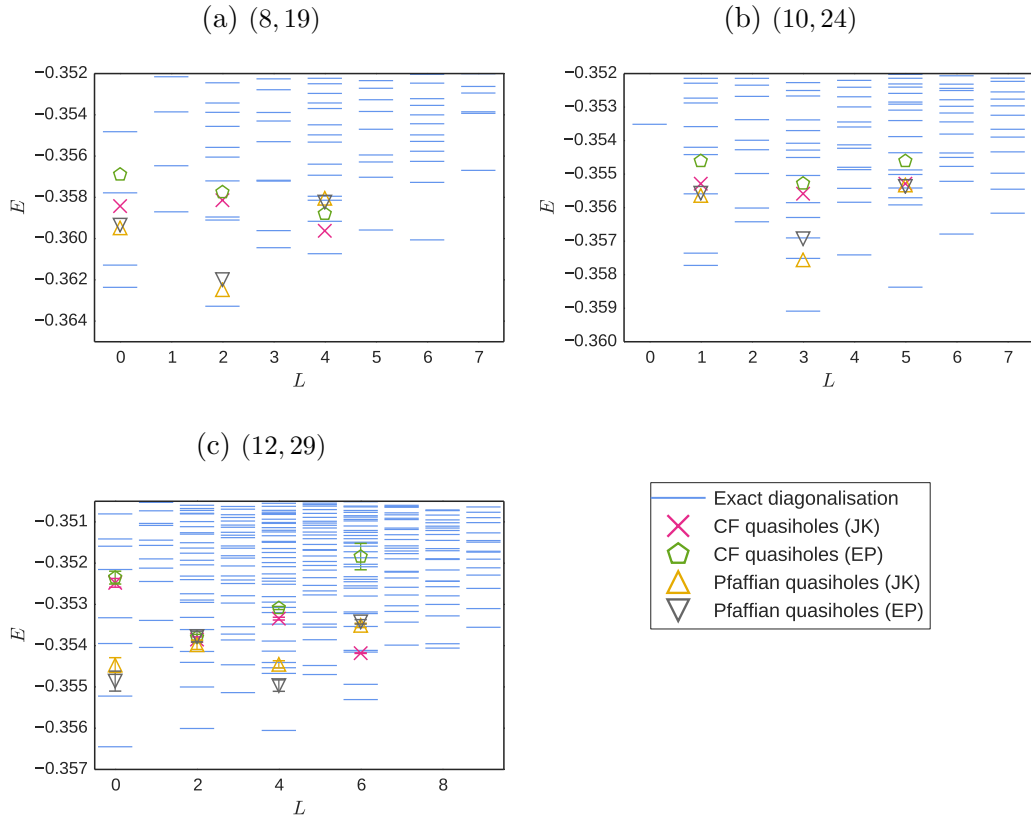


Figure 5.6: Exact low lying spectra of systems corresponding to excited BS states at filling  $\nu = 12/5$  with two quasipoles, i.e. at one extra flux, together with the variational energies of said states (note that the variational states are intended as trial wavefunctions of the lowest energy states at each  $L$ ). The two quasipoles are both realised in the same sector, corresponding to the CF or pfaffian part respectively, and both Jain-Kamilla (JK) and energy projection (EP) is utilised. Where not shown the errors are invisible on the scale of the figures.

predict the angular momentum of the lowest energy state at sizes  $N_e = 8$  and 10, respectively  $L = 2$  and 3. This is not the case for system size  $N_e = 12$ , however, where the exact spectrum has a minimum at  $L = 0$  while the pfaffian excitation energies at  $L = 0$  and 4 are equal up to error.

## 5.5 Modified states

In [23] it is noted that a trial wavefunction may be modified by a factor  $\prod_{i<j} f(|z_i - z_j|)$ , inserting lowest Landau level projection if not already present, without changing the universal properties of the state – thus introducing additional parameters that may improve the wavefunction. Taking a wavefunction  $\Psi$  as the starting point, we investigate the construct

$$\Psi_d = \mathcal{P}_{LLL} \Psi \prod_{i<j} |z_i - z_j|^{2d}, \quad (5.33)$$

with a modification factor  $d \in \mathbb{R}$ . These states have never before been studied because evaluation becomes intractable with the exact projection and there is no analogous approximation scheme to Jain-Kamilla.

The energy projection, however, is in principle indifferent to the form of the wavefunction before projection; as long as low LL content or other properties do not slow down the Monte Carlo convergence beyond applicability. This means that we can implement  $\Psi_d$  even for noninteger and negative  $d$ . The only constraint is that it must be limited to

$$d > -\frac{N_\Phi}{2(N_e - 1)} \quad (5.34)$$

to avoid the wavefunction becoming singular, as can be seen by considering the powers of the coordinates.

Naively a higher  $d$  will increase the correlations as the electrons are kept further apart (note explanation of this approximate term in section 3.3.1). This picture is complicated by the LLL projection, however, which makes the result harder to predict: in fact for the Laughlin state the  $N_e = 2$  and 3 wavefunctions with modification factor  $d = 1$  reduce to the regular  $d = 0$  states.

Note that the energy can never go below the exact Coulomb value regardless of the value of  $d$ . Moreover, as seen in section 3.2.1, raising the power can drive the system to a phase transition; although again the projection makes the result unclear. It seems the only way to discern the effect of modifying a trial wavefunction is by numerical investigation. Ref. [22] contains such a study by the present author together with Fremling, Moran and Slingerland; results from this paper constitute most of the next section.

### 5.5.1 Laughlin at filling $\nu = 1/3$

As a first test we attempt modification of the Laughlin state at filling  $\nu = 1/3$ , which has stood as a paradigmatic trial wavefunction for the fractional quantum Hall effect since its construction. The initial question is whether it can be improved with a nonzero factor  $d$  and if so which value is optimal.

Figure 5.7a exhibits the variational energy of the modified state as a function of  $d$  for system sizes  $N_e \in \{5, \dots, 11\}$ . It shows a dramatic improvement; note that the lower limits of the  $y$ -scales are the exact Coulomb energies. The minima lie somewhere between  $d = 1$  and 1.5, increasing with system size. The lower right plot scales the optimal value of  $d$  with  $1/N_e \rightarrow 0$  for values

$N_e > 6$ , where the worst finite size effects seem to have abated. The result is an interpolated estimate  $d_{min} = 1.487(8)$  in the thermodynamic limit. The fact that the modification factor has a well defined limit for macroscopic sizes gives confidence that the form of (5.33) is physically relevant.

In a sense it is no surprise that constructing a trial wavefunction with an additional parameter enables improvement. But the remarkable property of the data in figure 5.7a is the degree to which  $d \neq 0$  can lower the variational energy, which suggests that the parameter  $d$  captures important properties of the Coulomb state which is not fully reflected by the Laughlin wavefunction. Figure 5.7b shows that the difference in energy relative to the Coulomb state is considerably lowered using the state with optimal  $d$  versus the regular one at  $d = 0$ .

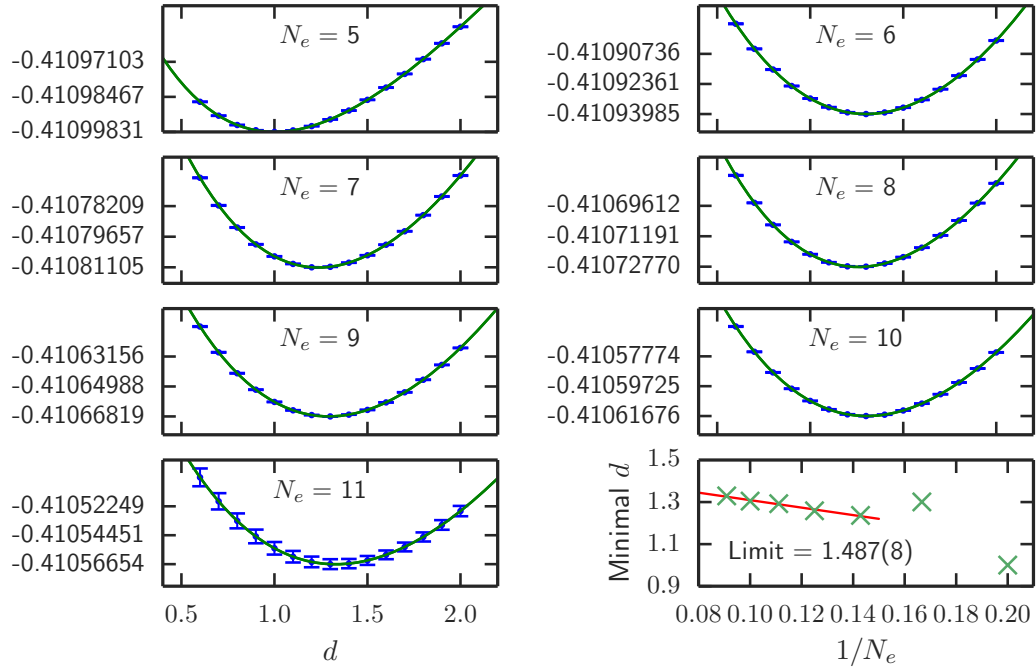
Another perspective is illustrated in figure 5.8, where the energy per particle is plotted against  $1/N_e$  for a range of modification factors up to  $d = 5$ . This allows us to interpolate the energy to the thermodynamic limit by using the constant term in a linear least squares fit as the energy in the infinite system. The interpolated results, shown in the figure, indicate that the improvement in variational energy is stable with system size and thus physically relevant. The fit includes system sizes  $N_e = 6$  to 11 to avoid the distinct finite size effects at  $N_e = 5$ , and the evolution with  $1/N_e$  is fairly linear until we reach  $d > 2$ . Whether the curve approaches linearity also for larger  $d$  at bigger sizes is unclear with the current data.

Note that the errors reported on the energies in thermodynamic limit in figure 5.8 only take into account the error from Monte Carlo and curve fitting, and not from the cutoff in the Hilbert space in the energy projection (these are likely negligible, however, and zero for systems below  $N_e = 9$ ) and more importantly further deviation with larger sizes  $N_e$ .

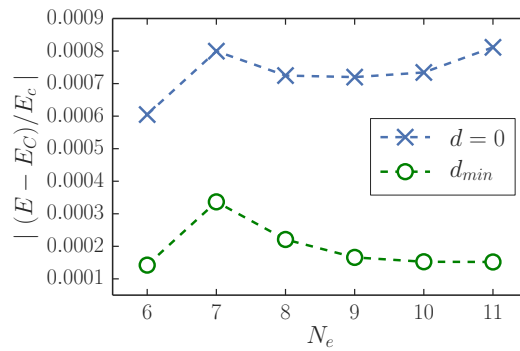
Figure 5.9 shows squared ground state overlaps for the modified states at different  $N_e$  and  $d$  and confirms that the optimum is around  $d = 1.3$  for these system sizes. Again these results indicate that the trial wavefunctions are greatly enhanced by altering  $d$ ; in particular the squared ground state overlap is extremely high around the maximum and does not decrease notably with the number of particles even up to  $N_e = 11$ .

A natural question is why the modified states perform so well. The original motivation was that the correlations would be improved as factors  $|z_i - z_j|$  contribute to keeping the electrons apart, and a natural measure for this is the pair correlation function  $g(r)$ . It is plotted at size  $N_e = 10$  in figure 5.10 for

## 5.5. MODIFIED STATES



(a) Variational energies of modified Laughlin  $\nu = 1/3$  states at different  $N_e$  with dependence on  $d$  and fitted using a polynomial of degree 5. The density correction (5.24) has been applied. The lower limits of the  $y$ -axes correspond to the Coulomb energy. The lower right panel show the optimal  $d$ -values plotted against  $1/N_e$  with a linear fit from  $N_e = 7$  to 11.



(b) Relative difference between the Coulomb eigenvalues  $E_C$  and variational energies  $E$  for the regular  $d = 0$  Laughlin state and the modified state at the minimum  $d_{min}$ , plotted against system size  $N_e$ .

Figure 5.7: Examining the variational energy of modified states as a function of  $d$ .

## 5.5. MODIFIED STATES

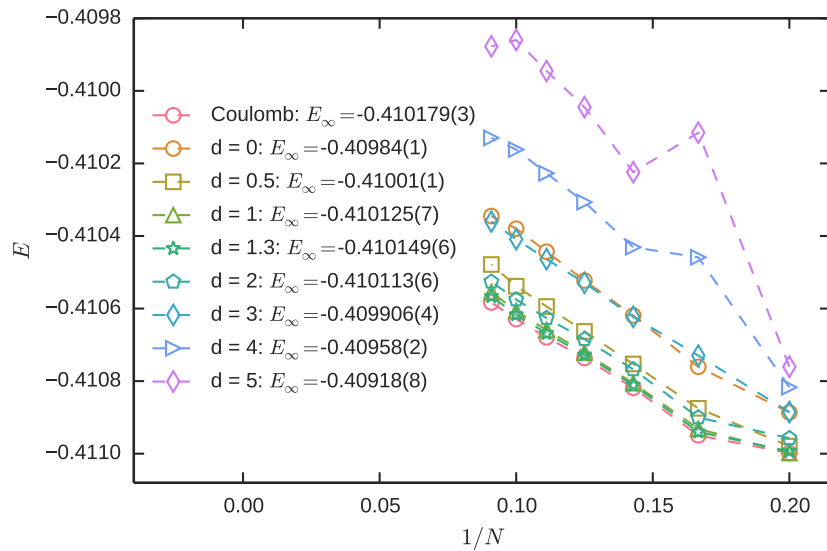


Figure 5.8: Energy dependence with system size  $N_e$  of modified Laughlin  $\nu = 1/3$  states at different  $d$ . The density correction (5.24) has been applied. The interpolation is a linear least squares fit including data points from  $N_e = 6$  to 11. The MC errors are invisible on this scale.

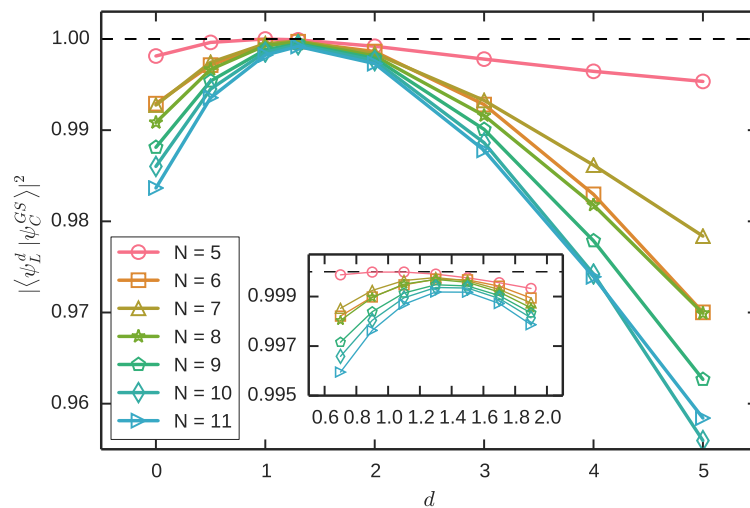


Figure 5.9: Overlaps squared between Coulomb ground states and modified Laughlin  $\nu = 1/3$  wavefunctions at different modification factors  $d$  and system sizes  $N_e$ . The inset shows detail around  $d \in [0.7, 1.9]$ . The MC errors are invisible on the scale of the figure.

## 5.5. MODIFIED STATES

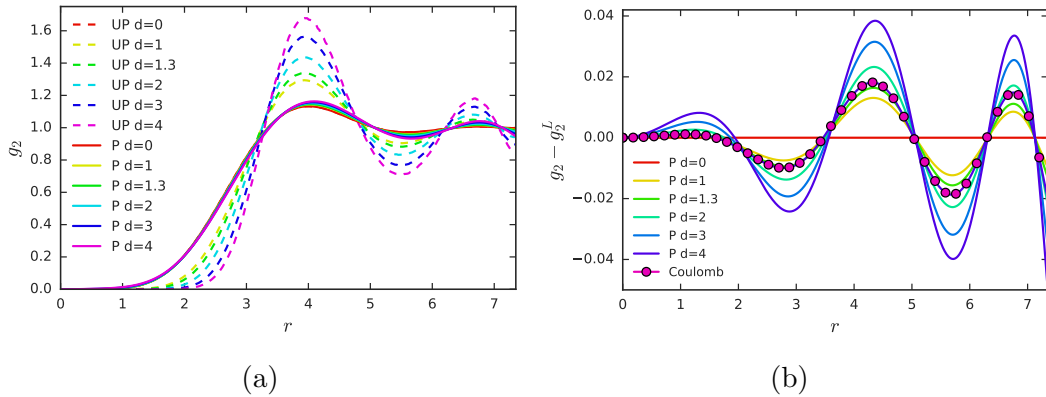


Figure 5.10: Pair correlation functions for the modified Laughlin states with  $N_e = 10$  electrons and different modification factors  $d$ . Dashed lines are unprojected states (UP) and solid lines are energy projected states (P). (a) shows  $g(r)$  plotted against the chord length  $r$  and (b) subtracts the regular Laughlin  $d = 0$  state and includes the exact result from diagonalisation of the Coulomb interaction.

chosen values of  $d$  before and after lowest Landau level projection.

In figure 5.10a the dashed lines show the unprojected states and it is clear that the intuition of the action of the modification before projection is correct; the correlation hole becomes wider with increasing  $d$ . In addition the oscillations already present in the regular Laughlin state are substantially increased, suggestive of the local onset of crystalline order. Examining the projected states plotted with solid lines, however, reveals that LLL projection eliminates most of the effect of the modification factors. The amplified oscillations are still discernible to an extent, while the alteration of the correlation hole is practically invisible on this scale.

Part of the effect of the LLL projection can be understood from the fact that there is a limit to how much states can be localised in the lowest Landau level. In particular the projection of the Dirac delta function is a coherent state of finite extent [23]. This imposes a constraint on the size of the correlation hole between two particles.

Figure 5.10b shows the pair correlation functions of the modified states, and the Coulomb state obtained from exact diagonalisation, with that of the regular  $d = 0$  Laughlin state subtracted. It illustrates the fact that the Coulomb state has stronger oscillations relative to the regular Laughlin state and that the modification factor in  $d$  assists in modeling these.

The state at  $d = 1.3$  is particularly close to the Coulomb state, especially at low  $r$ , in line with earlier observations; in about half of the plot the former is obscured by the latter. Note however that at higher  $r$  the  $d = 2$  state becomes as competitive or more, possibly related to the progression of optimal  $d$  at

## 5.5. MODIFIED STATES

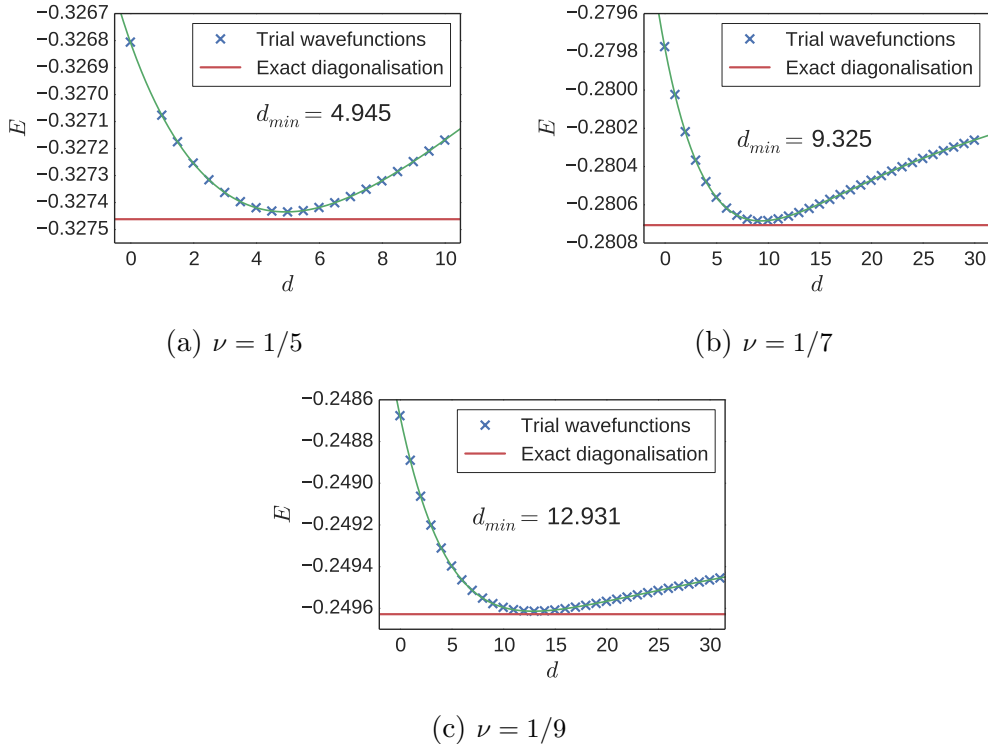


Figure 5.11: Plots of energy versus modification factor  $d$  for Laughlin states at  $\nu = 1/5$ ,  $1/7$  and  $1/9$  at system size  $N_e = 6$ . The errors are invisible on the scale of the figures.

larger sizes noticed in the lower right plot of figure 5.7a.

As mentioned above, a number of the numerical results presented here have been collected in ref. [22]. This paper also shows similar data for the torus geometry. The conclusions from the latter are analogous, although finite size effects appear larger on the torus; this indicates that the benefits of the energy projection and the modified states do not depend on the chosen geometry.

Finally one might ask how the results are affected by looking at modified Laughlin states at the filling factors  $\nu = 1/5$ ,  $1/7$  and  $1/9$ , i.e. using  $m = 5$ ,  $7$  and  $9$ . Figure 5.11 shows the energies plotted against  $d$  for these three states at  $N_e = 6$  particles, and we see that the results are again greatly improved by  $d \neq 0$ . The minima, however, occur at increasing values of  $d$ : around  $d_{min} = 4.945$  for  $\nu = 1/5$ ,  $d_{min} = 9.325$  for  $\nu = 1/7$  and  $d_{min} = 12.931$  for  $\nu = 1/9$ .

These considerations can possibly throw some light on the transition between the incompressible electron liquid of the fractional quantum Hall effect and the Wigner crystal (section 3.2.1). From experiment this is expected to occur between densities corresponding to  $\nu = 1/7$  and  $1/9$ . This can also be seen from the excited trial wavefunctions at  $\nu = 1/9$  by the fact that they have lower energies than the ground state, implying that the latter is unstable [18].

The regular Laughlin ground state itself, however, does not predict a transition between  $\nu = 1/7$  and  $\nu = 1/9$ ; from the plasma analogy and knowledge of the one-component two dimensional plasma (see section 3.2.1) this does not occur until the exponent, giving the ratio between plasma charge and temperature, reaches  $m \gtrsim 70$  [55]. The properties of the plasma can be expected to be altered by the modification factor, however. Before projection,  $|\Psi_d^L|^2$  for  $d > 0$  corresponds exactly to the Boltzmann weight of a two dimensional plasma at higher charge to temperature ratio than for  $d = 0$ , but with the wavefunction describing the same FQHE filling factor as the latter.

We do not expect a potential phase transition to vanish as a result of the projection, although this is not confirmed analytically. The modified Laughlin state closest to the ground state at  $\nu = 1/9$  might not quite reach plasma parameters corresponding to a crystal for the plasma (the thermodynamic limit is yet to be examined), but it appears to be significantly closer than the regular Laughlin wavefunction.

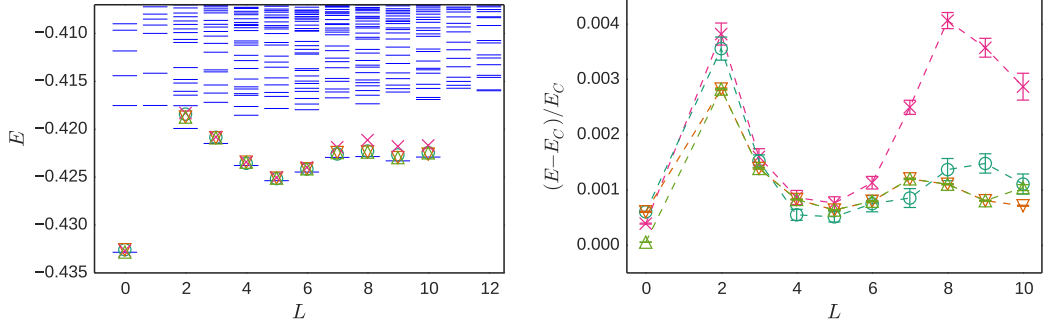
### 5.5.2 $\nu = 1/3$ as a reverse flux composite fermion state

The Laughlin  $\nu = 1/3$  state with modification factor  $d = 1$  is a special case, as it can also be seen as a reverse flux composite fermion state. The expressions for the reverse state in (3.9) with  $n = 1$  and  $p = 2$ , i.e. a single filled CF Landau level with  $2p = 4$  flux attached, gives the exact same state as the modified state (5.33) using  $d = 1$  and Laughlin's wavefunction (3.2) at  $m = 3$ .

We already know from section 5.5.1 that the modified Laughlin state with  $d = 1$  handled using the energy projection gives an improvement of the state; with this we are in a position to examine how these results are affected by utilising Jain-Kamilla projection instead. The latter can be implemented using the algorithm in section 5.1.2 and its generalisation to  $p = 2$  states in ref. [21].

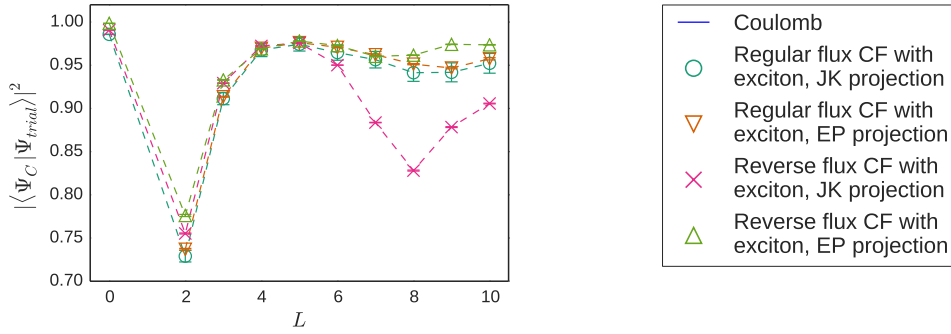
Considering the fact that the Laughlin  $\nu = 1/3$  state is the most prominent FQHE trial wavefunction, the question of whether the also well-established but little studied reverse flux CF state gives a better description should be handled with care. With this in mind we examine the ground state and first band of excitations projected both using energy and Jain-Kamilla projections, where the neutral excited states of the Laughlin wavefunction are taken to be excitons of regular flux composite fermions. Note that this leaves us with four distinct trial wavefunctions: the regular flux  $p = 1$  CF state and the reverse flux  $p = 2$  CF state, both using the two different projections.

## 5.5. MODIFIED STATES



(a) The exact spectrum and variational energies.

(b) Relative difference between variational energies  $E$  and the exact values  $E_C$ .



(c) Squared overlaps between trial wavefunctions and exact eigenstates.

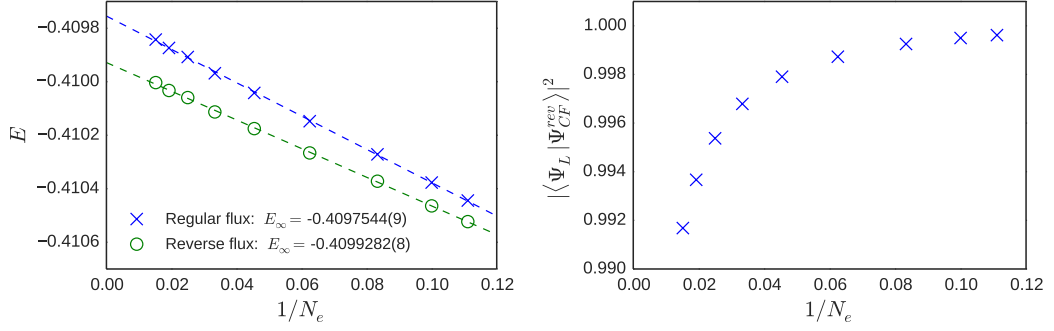
Figure 5.12: The  $\nu = 1/3$  state as a regular flux CF  $d = 0$  wavefunction and as a reverse flux CF  $d = 1$  wavefunction, projected using Jain-Kamilla (JK) and energy (EP) projection. The system size is  $N_e = 10$  electrons.

## Energies

Figure 5.12 displays results for  $N_e = 10$  electrons. The plot in 5.12a shows the energies from exact diagonalisation as well as the variational energies from the trial states. On this scale the differences are not clear; to alleviate this figure 5.12b shows the variational energies with the exact energies subtracted. As seen earlier the energy projected reverse flux wavefunction has a significantly lower ground state energy, and this is true for the Jain-Kamilla projected version as well although the difference is smaller.

But for the excitons there is no clear trend as to which state yields the lowest values, apart from the Jain-Kamilla projected reverse flux states, which have significantly higher energies. This is not the case for the corresponding energy projected state, showing that this property is not intrinsic to the reverse flux composite fermion state. Figure 5.12c displays the squared overlaps of the trial wavefunctions with the exact states, and the results are in line with the observations above.

## 5.5. MODIFIED STATES



(a) Variational energies plotted against  $1/N_e$  with the density correction (5.24) applied. The thermodynamic limits  $E_\infty$  are obtained from linear least squares fits.

(b) Overlap squared between the  $d = 0$  and  $d = 1$  states versus  $1/N_e$ .

Figure 5.13: The  $\nu = 1/3$  state as a regular flux CF  $d = 0$  wavefunction and as a reverse flux CF  $d = 1$  wavefunction, projected using Jain-Kamilla and scaled to the thermodynamic limit. The errors are invisible on the scale of the figures.

As mentioned in section 5.3.2 the excited trial states at lower  $L$  are often less accurate because they do not take into account interactions between excitations, which are expected to be more important at lower angular momentum where the particles have a higher probability of being closer together. This is especially pronounced in figure 5.12, where the overlap and variational energy are both markedly worse at  $L = 2$ .

The fact that the  $d = 1$  state can be computed also using the Jain-Kamilla projection means that we have access to bigger system sizes than those amenable to diagonalisation, and that the thermodynamic limit can be investigated more thoroughly. The limit was already studied using the data in figure 5.8, with the conclusion that  $d \neq 0$  states are more favourable also for macroscopic systems, but because of the restricted system sizes for the energy projection, finite size effects cannot be completely ruled out.

Figure 5.13a shows variational energies of the regular and reverse flux CF states projected using Jain-Kamilla, for system sizes up to  $N_e = 66$  electrons. The thermodynamic limit  $1/N_e \rightarrow 0$  shows unequivocally that the  $d = 1$  state is significantly more favourable also for macroscopic systems, with values  $E_\infty = -0.4097544(9)$  and  $E_\infty = -0.4099282(8)$  for the  $d = 0$  and  $d = 1$  wavefunctions respectively (as seen earlier the improvement using energy projection, and for different values of  $d$ , are even better). Considering this, the overlaps between the two states displayed in figure 5.13b are surprisingly high.

## Gaps

The gap to neutral excitations, modeled using CF excitons, is examined in figure 5.14. Similarly to the conclusions following figure 5.12 we see from the plot in 5.14a that the Jain-Kamilla projected reverse flux states have a higher energy at some values of the total angular momenta  $L$ , generally at values after and close to the minimum. The plot for  $N_e = 40$  particles in addition shows a small range of  $L$ -values where the regular flux energy is higher.

The gaps, i.e. the difference between the energies of the ground state and the lowest exciton, are displayed in figure 5.13b. They are equal within statistical error for the two states. This is true also in the thermodynamic limit, with estimates of  $\Delta_\infty = 0.0665(3)$  and  $\Delta_\infty = 0.0659(4)$  for the regular and reverse flux states respectively (note that this seems to disagree with the results in ref. [107] for the regular flux gap; the discrepancy stems from the fact that we use the lowest exciton energy while the latter reference uses that of the highest angular momentum exciton at  $L = N_e$ . Using the same state we get equal results).

### 5.5.3 Modified composite fermions

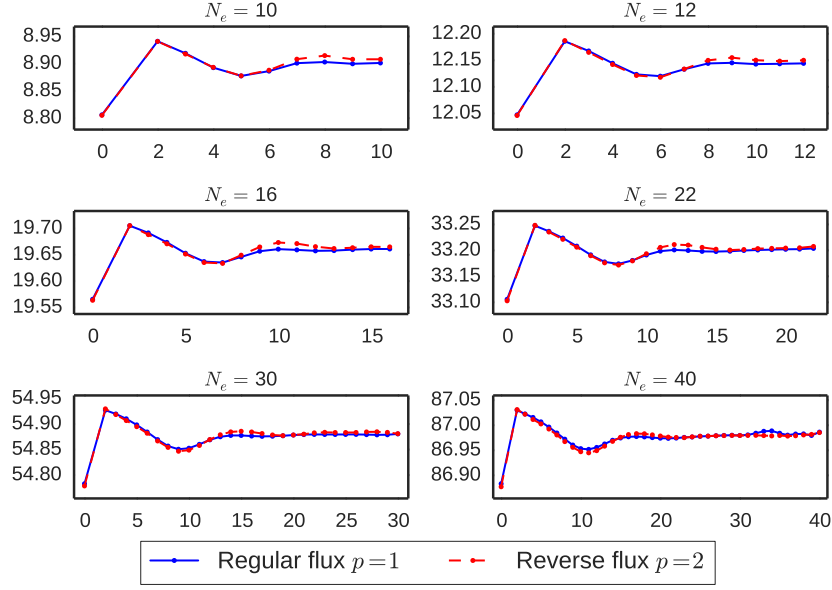
Having confirmed that the modified Laughlin states offer significant improvement over the regular versions, we turn to composite fermions and investigate whether the same holds true. The modified version of the wavefunction (3.8) is

$$\Psi_{\nu,d}^{CF} = \mathcal{P}_{LLL} \Phi_n^q \prod_{i<j} (z_i - z_j)^{2p} \prod_{i<j} |z_i - z_j|^{2d}, \quad (5.35)$$

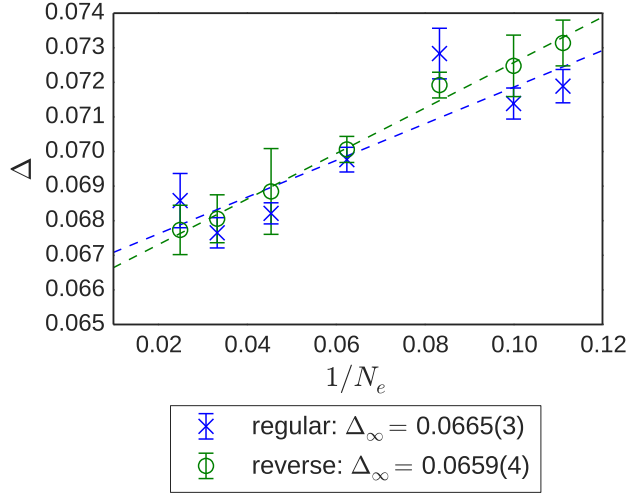
where  $\Phi_n^q$  is a determinant filling  $n$  CF Landau levels, with the magnetic field pointing into the sphere when  $q < 0$ . The filling factor is  $\nu = n/(2pn \pm 1)$ .

There is some freedom of interpretation in how to implement the lowest Landau level projection in (5.35). The only known way to project the last factor for general  $d$  is using the energy projection, which amounts to exact projection in all the examples in this section because the Hilbert space sizes allow incorporating all energy eigenstates (which means that bigger systems would also be within computational reach). The composite fermion part of the function, however, can be projected either using the Jain-Kamilla approximation or the (exact) energy projection. In section 5.3 it was demonstrated that, for the reverse flux states at  $d = 0$ , these give very similar results with the exact projection slightly better in general.

## 5.5. MODIFIED STATES



(a) Ground state and exciton energies.



(b) Exciton gap scaled to the thermodynamic limit  $1/N_e \rightarrow \infty$

Figure 5.14: Exciton gap  $\Delta$  at filling factor  $\nu = 1/3$  as a function of system size  $N_e$  for the regular flux CF  $p = 1$  state and the reverse flux CF  $p = 2$  state. The errors of the ground state and exciton energies in (a) are invisible on the scale of the figures.

The end results of approximate projection of some factors followed by exact projection of the rest versus exact projection of the entire state are hard to predict a priori. We will treat them as two sets of trial wavefunctions that are distinct but related; in particular they are very likely in the same universality class. These two sets can then be numerically tested. Below they are referred to as the EP state and the JK-EP state, signifying the projection of the entire function using energy projection and a combination of that and Jain-Kamilla projection respectively.

A third possibility would be to project the regular composite fermion state

## 5.5. MODIFIED STATES

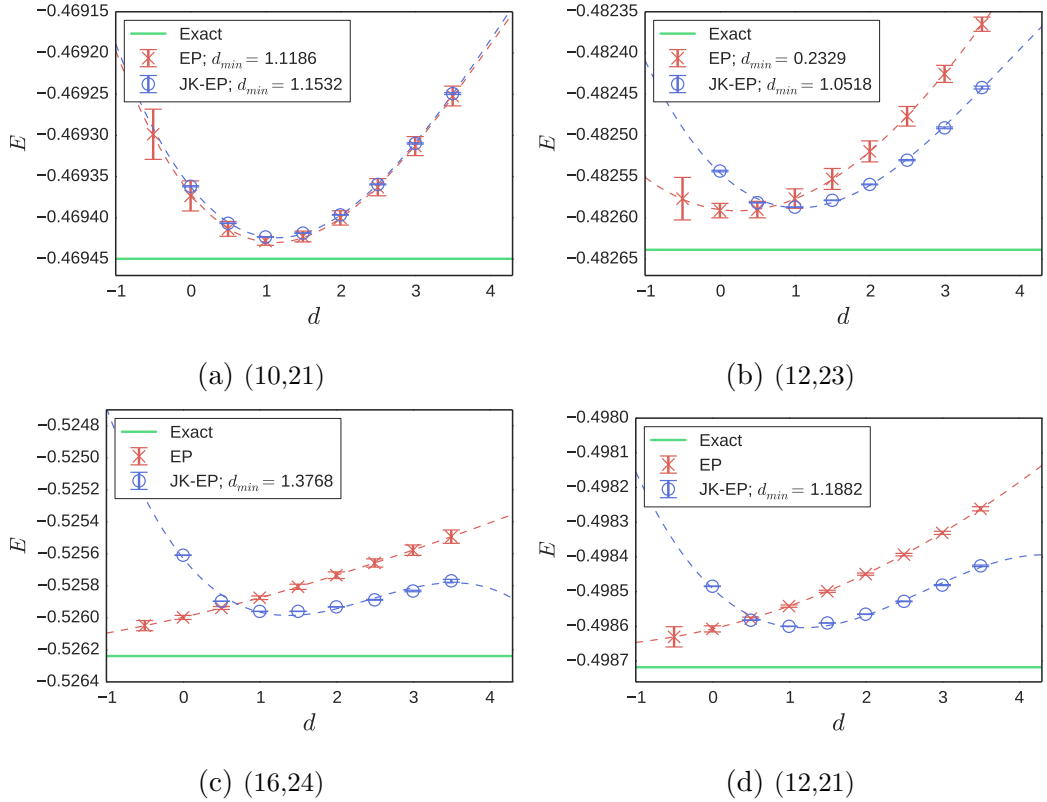


Figure 5.15: Energies of different modified composite fermion states as a function of  $d$ , both using exact projection of the entire state (EP, in red) and Jain-Kamilla projection of the normal CF factor followed by exact projection (JK-EP, in blue). Least square fits using polynomials of order 3 are shown with dashed lines. The minima of the fits are displayed where they can be found. Subtitles give the parameters  $(N_e, N_\Phi)$ ; the states are (a):  $\nu = 2/5$ , (b):  $\nu = 3/7$ , (c):  $\nu = 2/3$  and (d):  $\nu = 3/5$ . The energies of the exact states correspond to results from diagonalisation (green, solid line).

and the modification factor separately by energy projection and then multiply them. This requires multiplication in momentum space, however, and we concentrate on the first two options.

### Energies

Figure 5.15 displays variational ground state energies of the two sets of trial wavefunctions plotted against the modification factor  $d$ . The figures 5.15a and 5.15b show the regular flux states  $\nu = 2/5$  and  $\nu = 3/7$ , while 5.15c and 5.15d show the reverse flux states  $\nu = 2/3$  and  $\nu = 3/5$ . The exact Coulomb eigenvalues are also displayed.

The first thing to note is that modification factors  $d \neq 0$  again contribute to lowering the variational energy. But although the amount varies for the different states the improvement is in general not as drastic as that manifested in the Laughlin states in section 5.5.1. It is also clear that the choice of projection method matters, as both the quantitative and qualitative behaviour

is different for the two versions; manifested in the individual values and shapes of the interpolated curves respectively. The lowest energies obtained for each filling factor are comparable with the two methods, however.

The JK-EP states, although kept from being singular by the constraint (5.34), have very poor Monte Carlo convergence for  $d < 0$ , and the resulting values are not displayed. This is maybe not so surprising since the Jain-Kamilla projection lowers the powers of the coordinates in the function, which is then apparently unable to support well an inverse factor of absolute Slater determinants before projection.

The most interesting feature, however, is the qualitatively different behaviour of the regular and reverse flux composite fermion wavefunctions. Most strikingly, the reverse flux EP states obtain the minimum energy with negative modification factors, i.e.  $d_{min} < 0$ . In fact, due to the constraint on negative values of  $d$ , the fitted curves do not have clear minima in the sense that the regular flux wavefunctions do; the lowest  $d$  possible also gives the lowest energy.

Although they cannot support negative values of  $d$  the reverse flux JK-EP states also show a subtle departure from the regular flux states, in that the fit using a third degree polynomial is not as good. In particular the curve is not as symmetric around its minimum.

These qualitative differences show that the choice of projection method, although in principle a question of technical implementation, can have a significant impact on the resulting state. We also note that the non-orthogonality of the Jain-Kamilla projection is what allows these wavefunctions, which only differ in higher Landau level components, to project to different LLL functions. Finally it is striking that the orthogonal (exact) projection is not always the method to give the most beneficial results, as is clear at various values of  $d$  in the plots of figure 5.15.

### Pair correlations

As demonstrated in section 5.5.1, the effect of the modification factors can be illuminated by examining the pair correlation functions  $g(r)$ . This is also true when considering the contrast between regular and reverse flux CF states. Figures 5.16 (regular flux) and 5.17 (reverse flux) show the pair correlations of the same choice of wavefunctions as figure 5.15, with the EP states in the left columns and the JK-EP states on the right. The pair correlation of the exact Coulomb ground state is included, and the function  $g_{d=0}$  corresponding to the regular wavefunction with  $d = 0$  is subtracted.

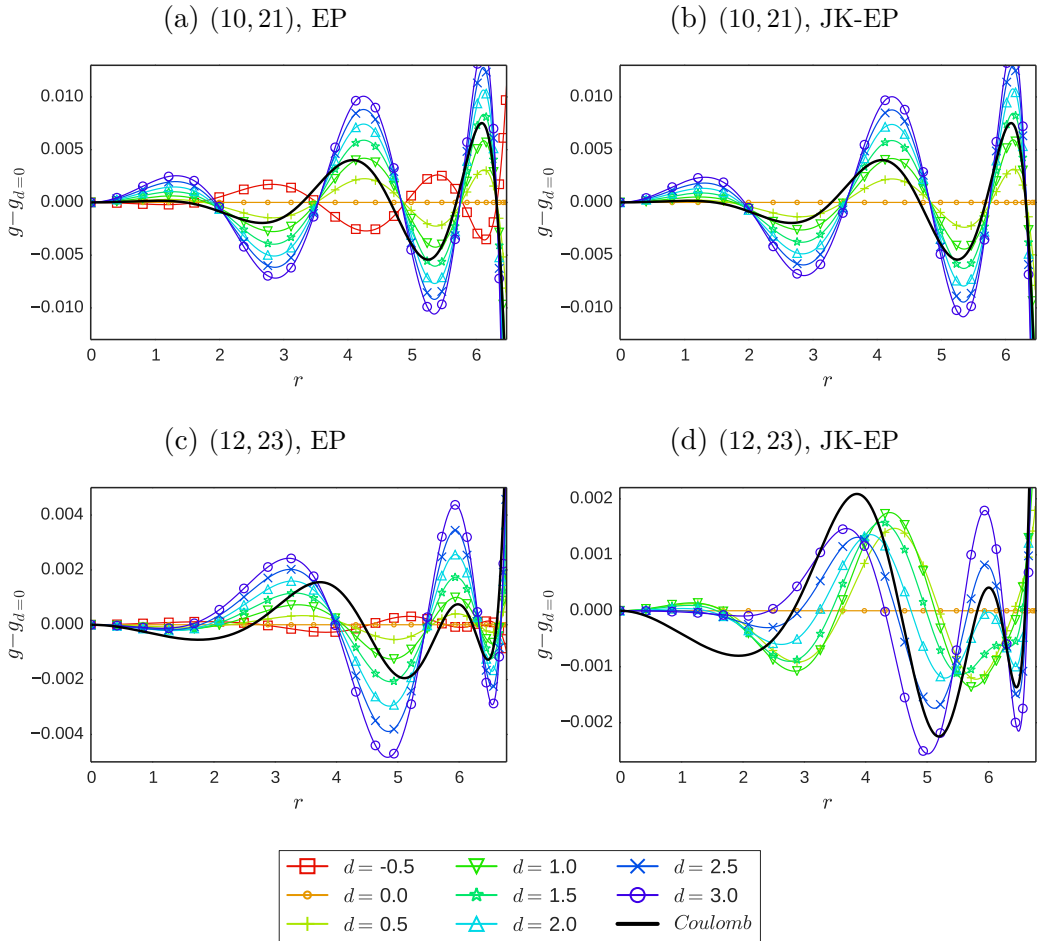


Figure 5.16: Pair correlation functions of modified regular flux composite fermion states at different modification factors  $d$  together with the corresponding Coulomb eigenstates. The pair correlations of the unmodified states at  $d = 0$  are subtracted. Wavefunctions in (a) and (c) are projected using energy projection while those in (b) and (d) are using a combination of energy projection and Jain-Kamilla projection. Note the different scales.

For the regular flux states one may draw similar conclusions to those following the pair correlations of the  $\nu = 1/3$  Laughlin state in figure 5.10. The Coulomb state has a differently sized correlation hole and oscillations relative to the  $d = 0$  composite fermion state, and the modified  $d \neq 0$  wavefunctions assist in modelling this. The pair correlation functions of the modified trial states closest to that of the Coulomb state are not as close as in the Laughlin case, however, in line with the results for the energy in figure 5.15.

We also note that it is not as clear which state has the lowest variational energy from simply looking at the pair correlation. Taking the regular EP state at filling  $\nu = 3/7$  in figure 5.17c as an example, one might think that with the Coulomb interaction being short range the state with the best fit around small  $r$  gives the lowest energy. That would seem to indicate a fairly high factor  $d$  is

favourable, maybe around  $d = 2$ . The energy, however, has a minimum value around  $d_{min} = 0.2329$ . Possibly this is due to the heightened value of  $g(r)$  relative to the Coulomb state around  $r \approx 3$  for the higher  $d$  states.

No significant qualitative differences between EP and JK-EP states can be surmised from the plots in figure 5.16, possibly apart from the fact that the difference between the results for the two sets of wavefunctions is greater for  $\nu = 3/7$  than for  $2/5$ . This is not surprising since  $\nu = 3/7$  has a larger content in higher Landau levels before projection, and we have already seen that the Jain-Kamilla and energy projections have a larger deviation in that case.

The same observation can be applied to the plots in figure 5.17: being reverse flux states they have larger content in higher LL's before projection and thus the difference between EP and JK-EP states is larger than for the regular flux states of figure 5.16.

For the reverse flux EP states in figures 5.17a and 5.17c we see that the oscillations of the pair correlation functions of states with  $d > 0$  relative to that of  $d = 0$  have the opposite phase to that of the Coulomb state. This is rectified by using a negative modification factor  $d < 0$ , in line with the variational energies being lower for reverse flux EP states in figure 5.15.

Interestingly the Jain-Kamilla projection achieves something similar in this case: the JK-EP states of figures 5.17b and 5.17d, yield modified wavefunctions with  $d > 0$  whose relative oscillations of the pair correlation function are in the same phase as the Coulomb state.

### Generalised modified states

The conclusions of the previous sections can be summed up by saying that the modified composite fermion states do not yield as significant improvements relative to the regular states at  $d = 0$  as does the modified Laughlin wavefunctions. This is reflected both by the fact that the variational energies are not lowered as much and the fact that the pair correlations do not have the same degree of resemblance to that of the Coulomb state.

Therefore one might ask if generalisations of the modified CF states (5.35) could better approximate the physics at these filling factors. Keeping in mind that the Laughlin state is realised as a composite fermion wavefunction with  $n = 1$  CF Landau levels filled, a reasonable guess is that it would be favourable to modify the CF orbitals in different levels independently. This would then result in several modification factors  $d_k$  for  $k = 1, 2, \dots, n$ .

A natural construction in this vein becomes apparent when considering the

## 5.5. MODIFIED STATES

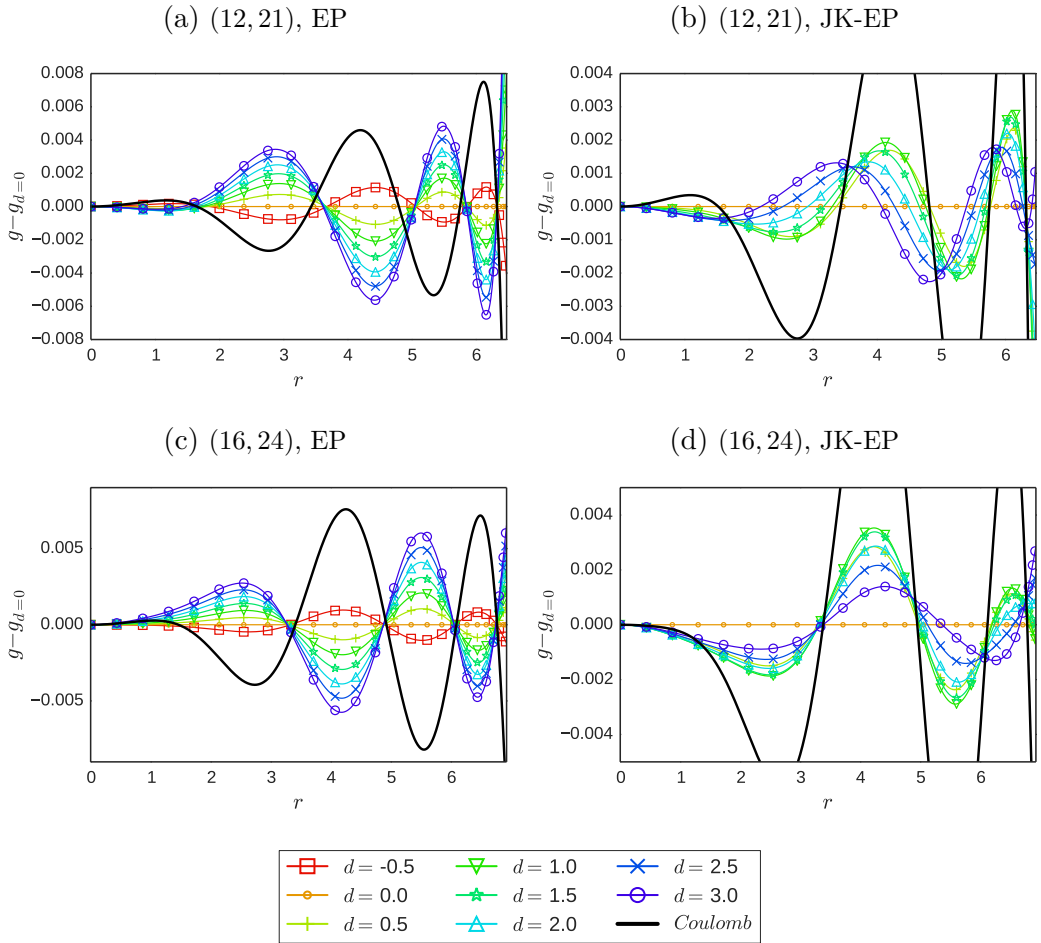


Figure 5.17: Pair correlation functions of modified reverse flux composite fermion states at different modification factors  $d$  together with the corresponding Coulomb eigenstates. The pair correlations of the unmodified states at  $d = 0$  are subtracted. Wavefunctions in (a) and (c) are projected using energy projection while those in (b) and (d) are using a combination of energy projection and Jain-Kamilla projection. Note the different scales.

Haldane-Halperin hierarchy of wavefunctions (section 3.2.3), and their classification in terms of  $K$ -matrices due to Wen [74]. These are square matrices whose dimension is equal to the hierarchy level, suggesting a single modification factor  $d$  for the first level, comprised by the Laughlin wavefunction, and in general one per level. Note that composite fermion wavefunctions filling  $n$  CF Landau levels are analogous to level  $n$  hierarchy wavefunctions in the correspondence between the two [77]. This framework was used for the modified Laughlin wavefunctions on the torus examined in ref. [22].

# Chapter 6

## Pair correlation functions decomposed

The pair correlation function contains a lot of information, but this is usually presented only in graphical plots, making reproduction or quantitative comparison difficult. In order to summarise the functions in a more quantitative manner they can be expanded in a suitable basis. If the coefficients are well behaved this can also facilitate interpolation to the thermodynamic limit. In this chapter one such basis is constructed and applied to study different trial wavefunctions.

### 6.1 Planar decomposition

Girvin defined a decomposition of  $g(r)$  on the disk, i.e. utilising multiparticle wavefunctions expanded in planar symmetric gauge orbitals [113]. By using transversal and rotational symmetries he constructed the sum

$$g(r) = 1 - e^{-r^2/2} + \sum_{m=1, \text{ odd}}^{\infty} \frac{2}{m!} \left(\frac{r}{2}\right)^{2m} c_m e^{-r^2/4} . \quad (6.1)$$

The basis functions

$$f_m = \frac{2}{m!} (r/2)^{2m} \exp(-r^2/4) \quad (6.2)$$

are centered around  $r = 2\sqrt{m}$ . They are chosen so that only a limited number of coefficients are necessary for a good fit, since  $g \rightarrow 1$  when  $0 \ll r < 2R$  then implies  $c_m \rightarrow 0$  when  $m \gg 1$ .

The first two terms of (6.1) correspond to  $g_1$ , the pair correlation function of the state  $\nu = 1$  [114]. Consequently the coefficients can be seen as

a measure of the deviation of a state's two particle correlations from that of  $\nu = 1$ . In addition physical arguments from charge neutrality, screening and compressibility yield constraints on  $c_m$ .

The simplest way to find the coefficients  $c_m$  is to use a least squares fit with chosen sample points and a cutoff  $K$  in number of functions so that  $m \leq K$ . The pair correlation function can then be reproduced to a high accuracy with relatively few coefficients, and (6.1) yields a good representation of a given function  $g(r)$ .

The properties of the coefficients themselves, however, are not as favourable. It is possible [24] but problematic to obtain numerically stable coefficients. By stable we mean that the values of  $c_m$  do not change significantly with the parameters; consisting of the choice and number of sample points, number of functions  $K$  and system size  $N_e$ . This is necessary in order to use the coefficients to uniquely characterise a given state and to scale them to the thermodynamic limit.

The situation can be improved by the following method, which in particular eliminates the need for arbitrarily chosen sample points. Using the basis functions (6.2), we have

$$c_m = \sum_k M_{mk}^{-1} \langle f_k | g - g_1 \rangle, \quad (6.3)$$

where  $M_{jk} = \langle f_j | f_k \rangle$  is the overlap matrix, necessary since the functions  $f_k$  are non-orthogonal. The ensuing Monte Carlo calculations are similar to (5.30):

$$\langle f_k | g \rangle \approx \frac{2 \sum_m \frac{|\tilde{\Psi}|^2}{P} \left( \sum_{i < j} f_k(r_{ij}) \right) \Big|_m}{A_i N_e \rho \sum_m \frac{|\tilde{\Psi}|^2}{P} \Big|_m}. \quad (6.4)$$

The resulting coefficients are different from those obtained using least square fits, and more stable. But the improvement is not adequate for consistent characterisation of a trial state or for scaling, as is demonstrated in detail in section 6.3.

Other possible steps include raising the number of MC samples, using very large system sizes, incorporating the constraints on  $c_m$ , and normalising the functions. However none of these result in a notable improvement, and faced with this situation we opt for constructing a new basis.

## 6.2 Spherical orthogonal decomposition

To obtain a decomposition that gives stable coefficients unhampered by numerical problems we use two measures. Firstly, since all our computations are done on the sphere, we construct a decomposition similar to (6.1) but using spherical instead of planar functions. Secondly, to make the coefficients more independent of each other and hopefully more stable, we formulate an orthogonal basis from these functions using the Gram-Schmidt procedure. The reasoning behind this is that the overlap between the planar  $f_k$  makes it possible to decompose very similar functions using very different coefficients. As an example of this one can get near zero functions using various large  $c_k$ , while for an orthogonal basis one would expect them to be small.

Similarly to the planar version we would like the decomposition to consist of  $g_1$ , the  $\nu = 1$  pair correlation function, plus a sum over basis functions. With this in mind we find  $g_1$  on the sphere:

$$g_1(\eta) = 1 - (1 - \eta^2)^{2Q} , \quad (6.5)$$

in terms of the unit distance  $\eta$  (2.34). The calculation can be found in appendix A; as far as we are aware this result has not appeared in the literature. In the limit of infinite radius we regain the planar  $\nu = 1$  function:

$$\lim_{2Q \rightarrow \infty} g_1(r) = 1 - e^{-r^2/2} . \quad (6.6)$$

### 6.2.1 Decomposition basis

As a starting point we write the wavefunction in a form exposing the dependence on particle 1 and 2:

$$\Psi = \sum_{j < k}^{2Q} a_{jk}(z_3, \dots, z_{N_e}) (\phi_j(z_1)\phi_k(z_2) - \phi_k(z_1)\phi_j(z_2)) , \quad (6.7)$$

where the antisymmetry of  $\Psi$  under exchange of  $z_1$  and  $z_2$  is explicit and  $a_{jk} \in \mathbb{C}$ . Using that the state is isotropic we can assume that particle 1 is at the north pole without loss of generality. With the distance between the particles measured in unit length  $\eta = \frac{r}{2R}$  we then have for the spinor

coordinates:

$$\begin{aligned} (u_1, v_1) &= (1, 0) \\ (u_2, v_2) &= \left( \sqrt{1 - \eta^2} e^{i\phi_2/2}, \eta e^{-i\phi_2/2} \right), \end{aligned} \quad (6.8)$$

where  $\phi_2$  is the azimuthal coordinate of the second particle. Using this together with (A.8), the first term in the brackets of (6.7) is zero unless  $j = 2Q$ , while the same holds true for the second term with  $k = 2Q$ . Since  $j < k \leq 2Q$  the first term vanishes, and we end up with

$$\Psi = - \sum_{j=0}^{2Q-1} a_{j,2Q} (1 - \eta^2)^{\frac{j}{2}} \eta^{2Q-j} e^{i(j-Q)\phi_2}. \quad (6.9)$$

Substituting this into (2.38) and using the fact that  $g(\eta)$  should be independent of  $\phi_2$  then yields

$$g(\eta) = \sum_{k=0}^{2Q-1} A_k (1 - \eta^2)^k \eta^{4Q-2k}, \quad (6.10)$$

where  $A_k = \frac{N_e(N_e-1)}{\rho^2} \int \prod_{i>2} d\Omega_i |a_{k,2Q}|^2$ . In order to extract the terms of  $g_1$  (A.9) we define expansion coefficients by  $A_k = \binom{2Q}{k} + d_k$ . After reordering the terms by  $k \rightarrow 2Q - k$  so that the functions with low indices are centered around the north pole, we end up with

$$\begin{aligned} g(\eta) &= 1 - (1 - \eta^2)^{2Q} + \sum_{k=1}^{2Q} d_k f_k(\eta) \\ f_k(\eta) &= (1 - \eta^2)^{2Q-k} \eta^{2k}. \end{aligned} \quad (6.11)$$

This constitutes a spherical decomposition of the pair correlation; next we want to orthonormalise it. Following the Gram-Schmidt procedure with the integral measure  $dS = 8\pi\eta d\eta$  for the inner products yields the following basis:

$$\begin{aligned} g(\eta) &= 1 - (1 - \eta^2)^{2Q} + \sum_{n=1}^{2Q} c_n G_n(\eta) \\ G_n(\eta) &= \mathcal{N}_n \eta^2 (1 - \eta^2)^{2Q-n} J_{n-1}^{(2,4Q+1-2n)}(1 - 2\eta^2) \\ \mathcal{N}_n &= \sqrt{\frac{(4Q+2-n)(4Q+1-n)(4Q-2n+1)}{4\pi Q n(n+1)}}, \end{aligned} \quad (6.12)$$

in terms of the Jacobi polynomials  $J_k^{(\alpha,\beta)}(z)$ . In a series representation the

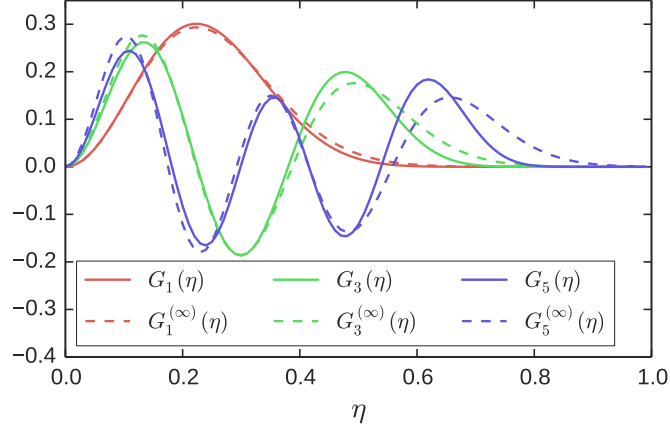


Figure 6.1: *Solid lines:* The first 3 odd orthogonal basis functions  $G_n(\eta)$  (6.12), plotted at  $2Q = 20$ . *Dashed lines:* The basis functions in the thermodynamic limit  $G_n^{(\infty)}(\eta)$  (6.14). The coordinate  $\eta = r/2R$  with  $2R^2 = 2Q = 20$  has been employed in order to compare with the finite functions.

Jacobi polynomials are given as [30]

$$J_k^{(\alpha, \beta)}(z) = \frac{\Gamma(\alpha + k + 1)}{k! \Gamma(\alpha + \beta + k + 1)} \sum_{j=0}^k \binom{k}{j} \frac{\Gamma(\alpha + \beta + k + j + 1)}{\Gamma(\alpha + j + 1)} \left(\frac{z-1}{2}\right)^j. \quad (6.13)$$

A proof that the functions in 6.12 are orthonormal can be found in appendix B. In practice we use a subset of the functions by imposing a cutoff  $K$  so that  $n \in \{1, \dots, K\}$ .

One of the reasons for constructing a new decomposition is to enable scaling of the coefficients to the limit  $N_e \rightarrow \infty$ . This is only meaningful if the corresponding limits of the functions in (6.12) exist, which indeed they do:

Through (2.36) the limit implies  $N_\Phi = 2Q \rightarrow \infty$ , so that the radius of the sphere becomes infinite and the geometry approaches a plane. Then writing  $2Q \approx N_e/\nu$  and reverting to the chord length  $r$  through  $\eta = \frac{r}{2R} \approx \frac{r}{\sqrt{2N_e/\nu}}$ , we find the limits

$$G_n^{(\infty)}(r) = \lim_{N_e \rightarrow \infty} G_n(\eta) = \frac{e^{-r^2/2} r^2}{\sqrt{\pi n(n+1)}} L_{n-1}^2(r^2), \quad (6.14)$$

where  $L_t^s(x)$  are the associated Laguerre polynomials (2.14). The functions  $G_n^{(\infty)}$  are orthonormal with respect to the planar integration measure given by  $dS = 2\pi r dr$ . Some of the basis functions are plotted in figure 6.1 (solid lines for finite systems and dashed lines for the limits).

Since the basis functions are orthogonal the coefficients can be found using

the simpler special case of (6.3):

$$c_n = \langle G_n | g - g_1 \rangle . \quad (6.15)$$

With this in mind the following result is useful:

$$\langle G_n | g_1 \rangle = \mathcal{N}_n (-1)^{n+1} \frac{8\pi Q [(2 + 4n)Q + 1 - n(n - 1)]}{(4Q + 2)(4Q + n - n)(4Q + 1 - n)} . \quad (6.16)$$

### 6.2.2 Condition number

Assuming that the orthogonal spherical basis is stable, as is argued in the section after this one, it is worthwhile to have a quantitative argument showing that the non-orthogonal one is not. The condition number  $C$  gauges the stability of a map between two quantities: if it is big it means that a small change in one induces a large change in the other. As a rule of thumb, if  $C \sim 10^k$ , up to  $k$  digits of accuracy may be lost in the map [115].

For a linear transformation  $\mathbf{a} \mapsto M\mathbf{b}$  the condition number is defined as

$$C_M = \|M\| \cdot \|M^{-1}\| , \quad (6.17)$$

where in our case we use the Euclidian norm.

Transforming between the two spherical bases involves the Gram matrix  $M_{nk}$  defined through  $G_n(\eta) = \sum_{k=1}^n M_{nk} f_k(\eta)$ , and from (6.11) and (6.12) this is given as

$$M_{nk} = \mathcal{N}_n \sqrt{\frac{8\pi(4Q - 2n)!(2n - 1)}{4Q + 1}} \frac{(2 + n - 1)!}{(4Q + 2 - n)!(n - 1)!} \\ \times \binom{n - 1}{k - 1} \frac{(4Q + 1 - n - k)!}{(k + 1)!} . \quad (6.18)$$

Figure 6.2 plots  $C_M$  for this matrix at some chosen values of the flux  $2Q$  against the number of functions included  $K$ , i.e. the dimension of  $M$ . For a given flux the condition number grows faster than exponentially with the dimension, quickly becoming very large. This indicates that if the orthogonal coefficients are accurate the non-orthogonal ones will be very imprecise.

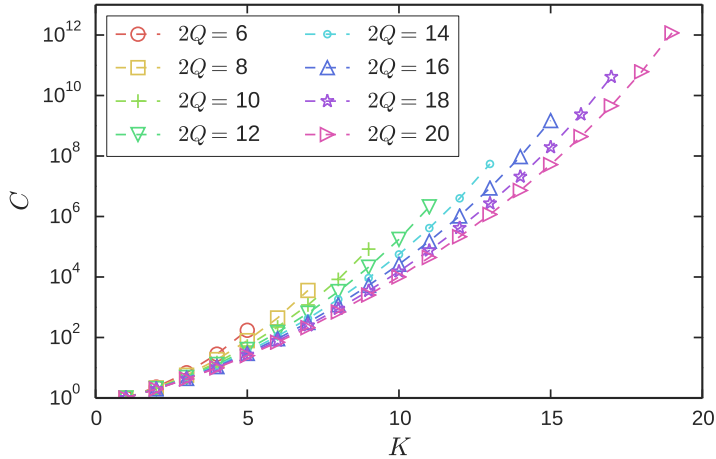


Figure 6.2: Condition number of the matrix in (6.18) at chosen values of  $2Q$ , plotted against dimension  $K$ .

### 6.3 Testing the decomposition

As a demonstration we decompose the Laughlin  $\nu = 1/3$  state at  $N_e = 22$  electrons using  $6 \times 10^6$  samples. The expansion is found using both a least squares fit and the inner product methods in (6.3) and (6.15), for both the planar decomposition in (6.1) and the orthogonal spherical one in (6.12).

We use either a cutoff  $K$  in the number of functions or the maximum number appropriate for the respective decompositions. On the naturally finite geometry of the sphere this is straightforward:  $K_{max} = 2Q$ , as seen in (6.12). For the disk we note that the basis functions  $f_k \propto r^{2k} \exp(-r^2/4)$  have their maximum at  $r = 2\sqrt{k}$  (with odd  $k$ ) and that trying to fit using functions that extend much beyond the system radius, i.e.  $r > 2R$ , gives poor results. With this in mind we impose a limit  $K_{max} = \lceil (2Q + 2)/4 \rceil$ , where  $\lceil \cdot \rceil$  indicates the ceiling function.

Figure 6.3 shows the pair correlation  $g_{MC}$ , computed using Monte Carlo, and  $g_{dc}$ , decomposed using the different expansions and methods, using up to  $K = 25$  coefficients. In the upper panel they are superimposed and visually indistinguishable; the difference is displayed in the lower panel. Note that all the decompositions have a similar small deviation near the end although they are not all visible.

The coefficients themselves are plotted in figure 6.4a. It is immediately striking how much the orthogonal spherical coefficients are independent of the method used to find them, in contrast to the planar ones. The latter also grow much larger (note the logarithmic scale). The spherical functions follow a pattern where coefficient  $n = 3, 8$  and  $15$  are smaller than the trend of their

### 6.3. TESTING THE DECOMPOSITION

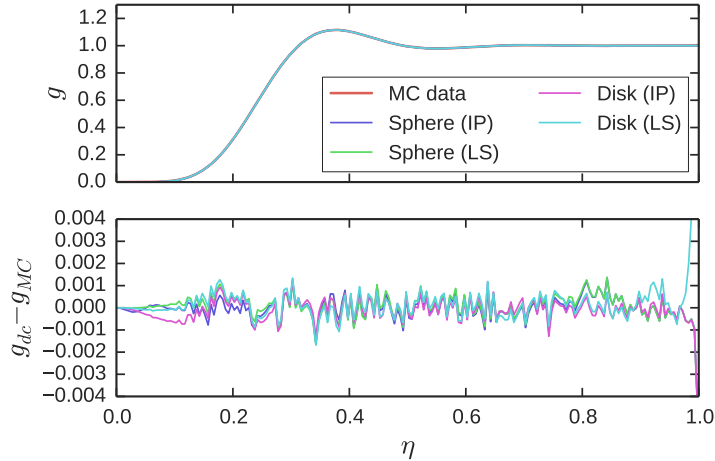


Figure 6.3: Pair correlation function  $g(\eta)$  of Laughlin  $\nu = 1/3$  at  $N_e = 22$  electrons computed using Monte Carlo (MC) and then decomposed (dc) using up to 25 coefficients. Both expansions on the disk and sphere (orthogonal) are used with the coefficients found using least squares (LS) and inner product (IP). The lower panel gives the difference between the correlation function expressed as bins and the expansions.

neighbours.

The Monte Carlo errors  $\sigma_n$  of individual coefficients are plotted in 6.4b, and the relative errors in 6.4c. The errors of the spherical decompositions are generally smaller than those of the planar ones, with some relative errors on the former being a bit larger than the general trend owing to the smaller size of the coefficients.

To compare with the pair correlation approximated with bins as in (5.30) we define the measure

$$\epsilon = \sqrt{\sum_j \frac{(g_{dc}(\eta_j) - g_{MC}(\eta_j))^2}{g_{dc}(\eta_j)}}, \quad (6.19)$$

where  $\eta_j$  are points from the north pole to the south pole corresponding to equidistant chord length.  $g_{MC}$  is the function that is approximated by the least square fits, and thus for the least square method  $\epsilon$  constitutes an expression for the fit error. The approximation obtained from the inner product method, on the other hand, is as fundamental as the bin approximation of  $g_{MC}$ , and so in these cases  $\epsilon$  can in principle be seen as a consistency check between different approximations of the pair correlation. We also use it as an indication of how many basis functions are necessary in order to give as good a fit as the bin approximation.

Figure 6.4d shows the dependence of  $\epsilon$  on the number of included functions  $K$  for the different expansions. The value decreases fast for both de-

### 6.3. TESTING THE DECOMPOSITION

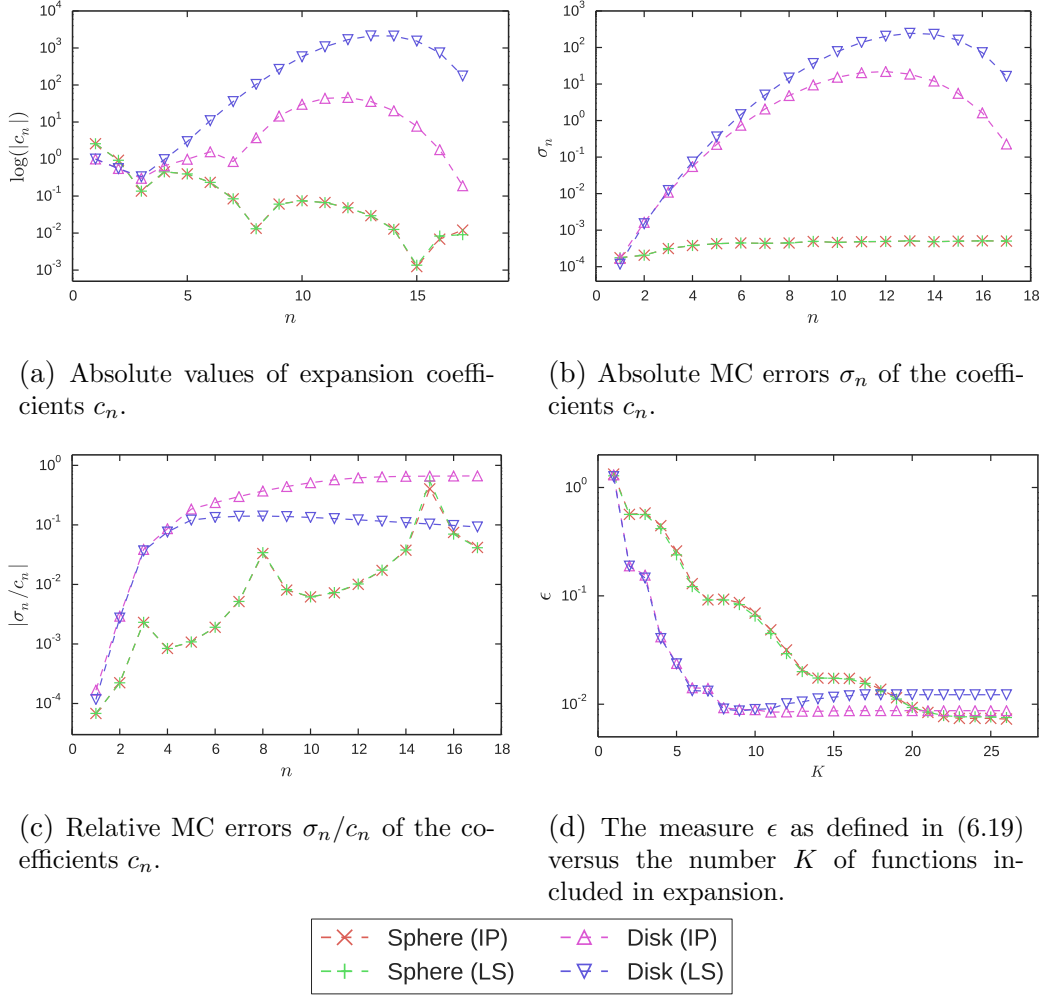


Figure 6.4: Decomposition of the Laughlin  $\nu = 1/3$  state at  $N_e = 22$  electrons and  $6 \times 10^6$  samples done using the planar (6.1) and orthogonal spherical (6.12) expansions. Note the abbreviations IP (inner product) and LS (least squares) for the method used to obtain the coefficients. All the plots are in logarithmic scale.

compositions but faster for the planar one, which also reaches a region of no improvement earlier. Note that the error of the least squares fit using planar functions is seen to increase with  $K$  after a certain value, indicating that this is the optimal number of functions in this case.

From the above considerations we can conclude that both expansions give relatively good representations of the pair correlation, with the orthogonal spherical version having the most advantages. But more important for us is the issue of the stability of the coefficients. We first look at the response to altering the cutoff  $K$  in number of functions included.

Figure 6.5 shows the evolution of the different coefficients as more are added, relative to their final value. This is done using least squares on both geometries and inner products on the disk. The plots are given a shift in the  $y$ -axis corresponding to function index  $n$  to make them visually distinguishable;

### 6.3. TESTING THE DECOMPOSITION

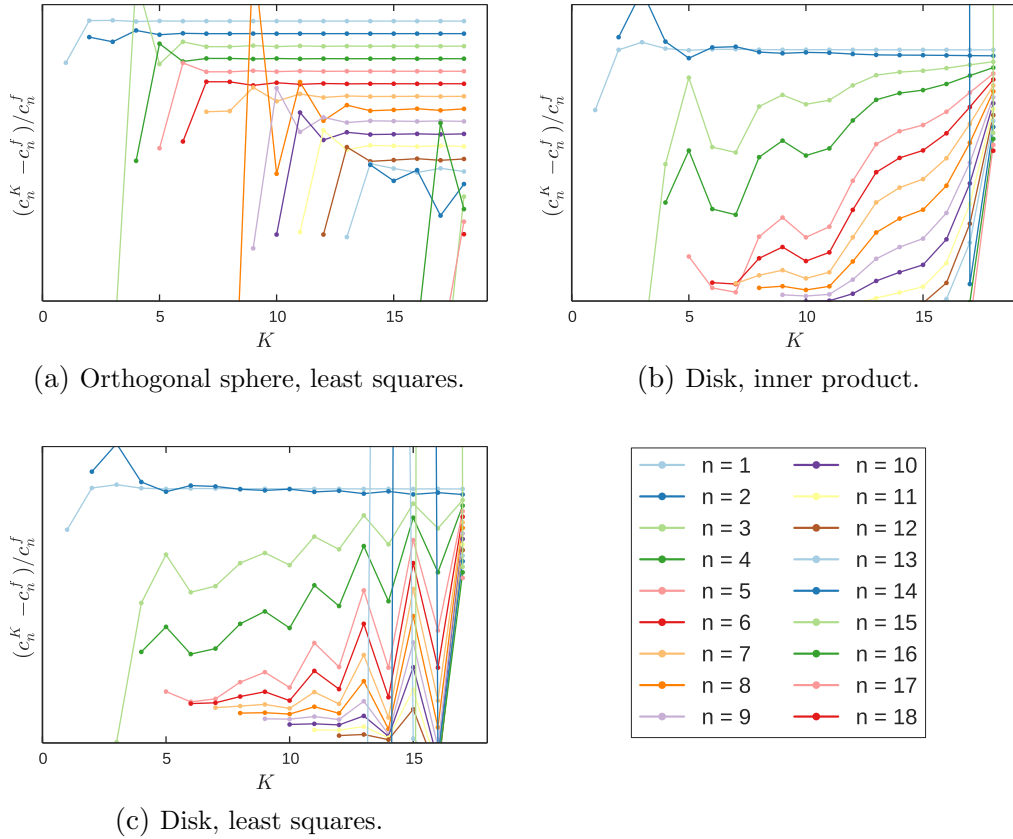


Figure 6.5: Evolution of the pair correlation expansion coefficients quantified as the relative difference between the value  $c_n^K$  when a number  $K$  are included and the final value  $c_n^f$ . The plots feature an offset between coefficients, with the lowest  $n$  on top, and thus the actual values are not displayed. The  $y$ -scale of (a) is narrower than that of (b) and (c); the offsets are the same and the rightmost points are all equal to one.

because of this the actual values are not displayed. However note the difference in scale on the  $y$ -axis of the three plots: they all have the same shift and the rightmost values are equal to one.

It is clear that while the planar expansions have a large variation in  $c_n$  with  $K$ , slightly less so for the inner product method, even the least squares fit gives very stable  $c_n$  using the orthogonal spherical basis (although less so for the extra small ones). Using the inner product method with the orthogonal spherical basis gives completely stable coefficients that have no variation with  $K$ .

Finally we want to confirm that the decomposition coefficients have a well defined thermodynamic limit. Figure 6.6 shows the first 15 orthogonal spherical coefficients obtained through inner products, plotted against  $1/N_e$  (the rest of the coefficients  $c_n$  for higher  $n$  follow a similar pattern). Linear (red line) and parabolic (green line) least square fits are superimposed, and the latter appears to give a good fit in general. The value of the parabolic curve at  $1/N_e = 0$  then gives an estimate of the coefficients in the thermodynamic

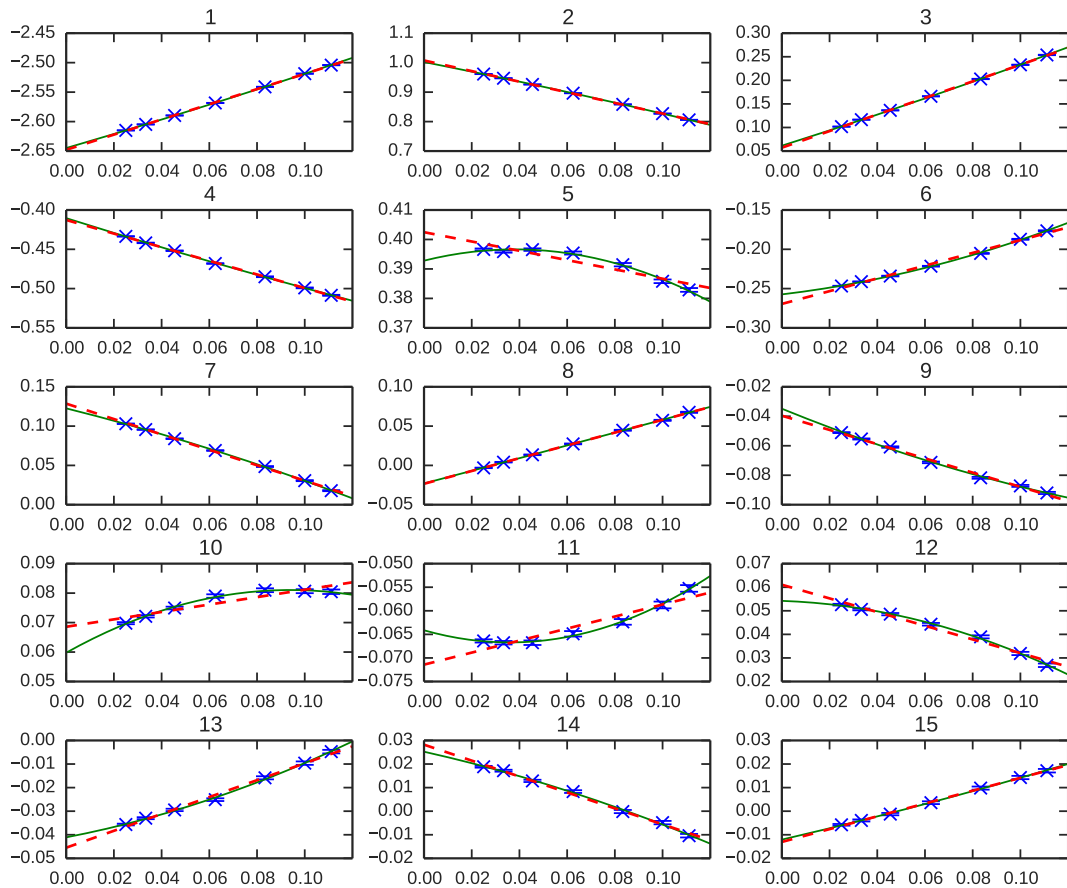


Figure 6.6: Expansion coefficients of the Laughlin  $\nu = 1/3$  wavefunction in the orthogonal spherical decomposition, obtained using inner products, plotted against  $1/N_e$ . The first 15 coefficients are shown together with linear (red, dotted) and parabolic (green, solid) least squares fits.

limit.

As a contrast the first 9 coefficients for the planar expansion, using inner products, are displayed in figure 6.7. The coefficients do not have a similar well defined limit and this gets worse for higher  $n$ . This confirms that the orthogonal spherical basis is far more stable than the planar one both in terms of number of functions included  $K$  and system size  $N_e$ . After these considerations we can turn to examination of various pair correlation functions in the thermodynamic limit.

## 6.4 Pair correlation functions in the thermodynamic limit

In this section we apply the orthogonal spherical expansion basis to scale the pair correlation functions of some of the most prominent trial wavefunctions to the thermodynamic limit. The number of basis functions  $2Q$  at a given system

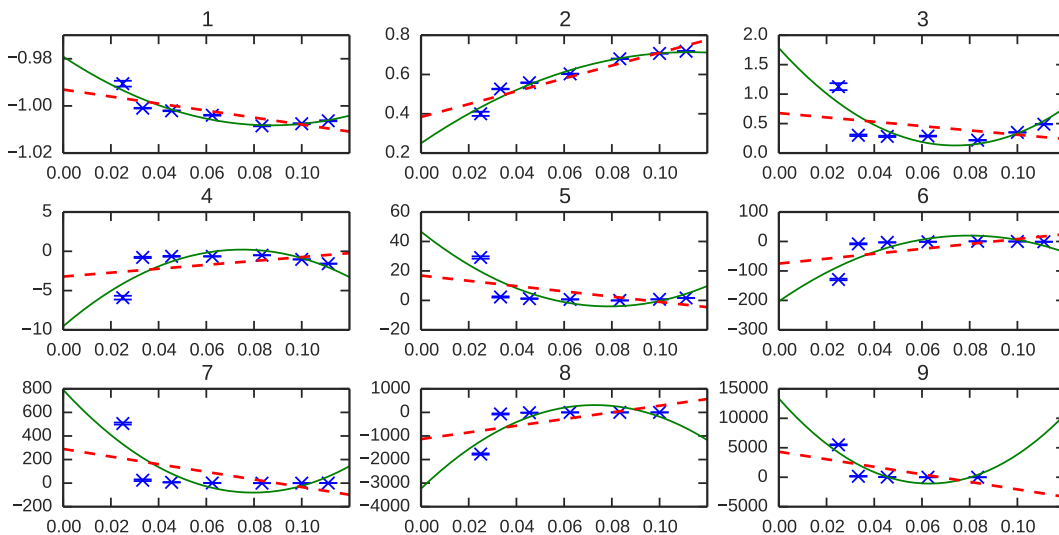


Figure 6.7: Expansion coefficients for the planar decomposition obtained through inner products, plotted against  $1/N_e$ . The first 9 coefficients are shown together with linear (red, dotted) and parabolic (green, solid) least squares fits.

size  $N_e$  goes to infinity in the macroscopic limit. However, since quantum Hall effect states have the property that  $g(\eta) \rightarrow 1$  for  $0 \ll \eta < 1$ , the number of functions required for a good description of the pair correlation is limited. This is indicated in figure 6.4d.

The number of coefficients necessary for a good description depends on the radius for which there are deviations from  $g = 1$ , since the reach of a basis function  $G_n$  increases with  $n$ . This radius is related to the size of the correlation hole, which as a rule of thumb is larger for lower filling fractions, corresponding to lower densities. Therefore especially low density systems, such as the state with filling  $\nu = 1/7$ , require more coefficients.

In line with the above the size of individual coefficients  $c_n$  generally decrease with  $n$ . As a rough guide to how many coefficients  $K$  to include we impose an approximate cutoff around the point where the errors become comparable to the size of the coefficients themselves, for the numbers of samples used in our computations (up to  $n \sim 10^8$  for smaller systems). With this approach we interpolate the pair correlations of the Laughlin wavefunction at filling factors  $\nu = 1/3$ ,  $1/5$  and  $1/7$ , the regular flux composite fermion state at  $\nu = 2/5$  and the Moore-Read wavefunction at filling  $\nu = 2 + 1/2$ . The scaled coefficients are displayed in tables 6.1 and 6.2, and the resulting pair correlation functions are plotted together with the finite system versions in figure 6.8.

As discussed above the number of included coefficients is inversely related to the density, for  $\nu = 1/7$  in particular we judge that  $K = 98$  functions is sufficient although the errors are still not quite at the same sizes as the

coefficients. The most obvious feature of the tabulated coefficients is that the sizes of the coefficients increase with decreasing filling fraction. This is in line with the fact that they measure the deviation from the denser  $\nu = 1$  state (which is described by  $c_n = 0$  for all  $n$ , see section 6.8b), having larger correlation holes and stronger oscillations due to the decreasing density.

Focusing on the trial states for systems in the lowest Landau level, i.e. the plots in figures 6.8b, 6.8c, 6.8d and 6.8e, we see a smooth progression of pair correlations with the number of particles  $N_e$ . The functions for individual system sizes are clearly converging towards the thermodynamic limit, with decreasing differences between plots corresponding to increasing system size.

The second Landau level Moore-Read state in figure 6.8a, however, shows a more complicated behaviour. The graph for the function in the macroscopic limit is significantly removed from the finite size pair correlations, whose difference is also increasing with number of particles  $N_e$  at these sizes. The coefficients still have a well defined behaviour with system size, however, as shown in figure 6.9. These considerations are striking since the Moore-Read state is characterised by pairing of the electrons, and it would be interesting to see the behaviour at higher  $N_e$  – presumably the differences between functions start decreasing at some point.

With these expansion coefficients we have a systematic fingerprint of the chosen trial states in the macroscopic limit. Several immediate further uses come to mind, including computing the single mode approximation [24] of the neutral gap in the macroscopic limit, scaling the pair correlations of Coulomb states, and scaling the density profiles of quasiholes, whose form is closely related to the pair correlation function.

$n$	$\nu = 2 + 1/2$	$\nu = 2/5$	$n$	$\nu = 2/5$	$n$	$\nu = 1/3$
1	-1.2070(1)	-2.02170(9)	39	0.0007(4)	1	-2.6446(1)
2	0.5840(1)	0.6356(3)	40	-0.0025(6)	2	1.0031(1)
3	-0.1156(4)	0.1962(2)	41	0.0011(5)	3	0.0593(2)
4	-0.1180(1)	-0.3787(2)	42	-0.0010(1)	4	-0.4101(4)
5	0.1928(2)	0.2634(2)	43	-0.002(2)	5	0.3950(2)
6	-0.1778(2)	-0.0916(7)	44	-0.0017(5)	6	-0.2611(6)
7	0.1246(3)	-0.0376(8)	45	-0.0016(7)	7	0.1238(7)
8	-0.0659(2)	0.1006(6)	46	0.0017(2)	8	-0.0212(2)
9	0.0176(2)	-0.1098(7)	47	0.0010(9)	9	-0.0343(3)
10	0.0159(2)	0.0885(1)	48	-0.0013(4)	10	0.0593(4)
11	-0.0323(2)	-0.0541(4)	49	0.0014(8)	11	-0.0663(9)
12	0.0358(2)	0.020(1)	50	0.0012(8)	12	0.0560(4)
13	-0.0326(3)	0.005(1)	51	0.0003(3)	13	-0.0424(3)
14	0.0292(3)	-0.025(2)	52	0.0023(9)	14	0.0251(3)
15	-0.0197(1)	0.036(1)	53	0.002(1)	15	-0.0111(3)
16	0.0115(2)	-0.0423(5)	54	0.0015(9)	16	0.0057(6)
17	-0.0069(7)	0.0431(4)	55	0.0003(3)	17	0.0018(5)
18	0.0003(1)	-0.0395(10)	56	-0.0017(8)	18	-0.0103(7)
19	0.0007(3)	0.032(1)	57	-0.007(2)	19	0.0121(3)
20	-0.0048(6)	-0.024(1)			20	-0.0092(3)
21	0.0044(3)	0.016(1)			21	0.0097(2)
22	-0.0049(4)	-0.0052(9)			22	-0.0057(3)
23	0.0065(3)	0.00002(-)			23	0.0043(4)
24	-0.00428(8)	0.0057(1)			24	-0.0044(7)
25	0.0064(2)	-0.0092(3)			25	0.0034(4)
26	-0.0037(2)	0.0118(6)			26	-0.0002(-)
27	0.0034(4)	-0.0125(10)			27	0.0009(3)
28	-0.0028(3)	0.0122(9)				
29	0.0011(3)	-0.0109(10)				
30	-0.0009(8)	0.0086(6)				
31	-0.0002(-)	-0.0073(4)				
32	-0.0004(1)	0.0033(4)				
33	-0.0027(5)	-0.0022(5)				
34	0.0008(-)	0.0026(2)				
35	-0.0004(3)	0.0003(-)				
36	0.0009(4)	-0.0022(2)				
37	-0.0007(2)	0.0009(10)				
38	0.0024(2)	0.00008(-)				

Table 6.1: Expansion coefficients  $c_n$  for the Moore-Read wavefunction at filling  $\nu = 2 + 1/2$ , the composite fermion state at  $\nu = 2/5$ , and the Laughlin wavefunction at  $\nu = 1/3$ .

$n$	$\nu = 1/5$	$n$	$\nu = 1/5$	$n$	$\nu = 1/7$	$n$	$\nu = 1/7$
1	-3.56130(7)	50	0.0181(8)	1	-3.73174(3)	50	-0.098(3)
2	2.84379(6)	51	-0.0166(6)	2	3.4642(1)	51	0.092(5)
3	-1.8247(1)	52	0.013(2)	3	-3.0896(2)	52	-0.074(4)
4	0.7120(1)	53	-0.0167(3)	4	2.4519(3)	53	0.059(4)
5	0.1694(2)	54	0.0160(5)	5	-1.5897(5)	54	-0.052(4)
6	-0.6835(3)	55	-0.0154(5)	6	0.6610(4)	55	0.033(3)
7	0.8748(5)	56	0.013(2)	7	0.1619(1)	56	-0.021(2)
8	-0.8482(5)	57	-0.011(3)	8	-0.7726(5)	57	0.0049(6)
9	0.6996(2)	58	0.0065(4)	9	1.1408(8)	58	0.005(1)
10	-0.5023(5)	59	-0.0047(7)	10	-1.289(1)	59	0.0162(5)
11	0.3068(3)	60	0.0041(3)	11	1.270(2)	60	0.030(3)
12	-0.1353(4)	61	0.002(2)	12	-1.1457(9)	61	-0.034(4)
13	-0.0042(7)	62	-0.004(2)	13	0.9610(5)	62	0.044(3)
14	0.1071(6)	63	0.0039(6)	14	-0.744(1)	63	-0.051(5)
15	-0.174(1)	64	-0.0067(3)	15	0.5197(7)	64	0.036(3)
16	0.2117(7)	65	0.001(1)	16	-0.3082(5)	65	-0.040(1)
17	-0.2255(3)	66	-0.0073(7)	17	0.1247(3)	66	0.040(3)
18	0.2176(4)	67	0.006(1)	18	0.027(1)	67	-0.040(4)
19	-0.1965(6)	68	-0.0033(9)	19	-0.154(1)	68	0.040(5)
20	0.1691(4)	69	0.007(1)	20	0.2573(9)	69	-0.040(5)
21	-0.1362(4)	70	-0.003(1)	21	-0.328(1)	70	0.039(4)
22	0.1026(6)	71		22	0.372(1)	71	-0.039(3)
23	-0.0680(6)	72		23	-0.395(2)	72	0.036(4)
24	0.0387(8)	73		24	0.401(1)	73	-0.038(3)
25	-0.0098(4)	74		25	-0.3924(9)	74	0.038(3)
26	-0.0111(5)	75		26	0.3686(5)	75	-0.039(1)
27	0.0266(10)	76		27	-0.3364(6)	76	0.0384(8)
28	-0.0456(5)	77		28	0.3011(9)	77	0.0345(4)
29	0.0526(4)	78		29	-0.2563(9)	78	0.028(1)
30	-0.0614(7)	79		30	0.208(1)	79	-0.027(1)
31	0.0631(3)	80		31	-0.166(2)	80	0.023(1)
32	-0.064(1)	81		32	0.121(1)	81	-0.021(2)
33	0.061(1)	82		33	-0.076(3)	82	0.017(2)
34	-0.054(1)	83		34	0.037(2)	83	-0.013(1)
35	0.053(2)	84		35	0.003(1)	84	0.0056(8)
36	-0.0453(9)	85		36	-0.038(2)	85	-0.002(1)
37	0.038(1)	86		37	0.061(3)	86	0.0004(-)
38	-0.0266(8)	87		38	-0.083(2)	87	0.007(1)
39	0.0180(5)	88		39	0.102(1)	88	-0.009(1)
40	-0.008(1)	89		40	-0.1193(9)	89	0.0093(9)
41	0.0015(7)	90		41	0.1352(8)	90	-0.009(1)
42	0.0007(-)	91		42	-0.142(1)	91	0.0135(6)
43	-0.006(2)	92		43	0.145(2)	92	-0.020(1)
44	0.015(2)	93		44	-0.143(2)	93	0.013(2)
45	-0.0126(7)	94		45	0.141(2)	94	-0.023(1)
46	0.0139(8)	95		46	-0.140(3)	95	0.018(1)
47	-0.0149(4)	96		47	0.128(2)	96	-0.027(2)
48	0.0163(7)	97		48	-0.121(4)	97	0.024(3)
49	-0.0187(6)	98		49	0.114(3)	98	-0.020(1)

Table 6.2: Expansion coefficients  $c_n$  for the Laughlin wavefunction at filling factors  $\nu = 1/5$  and  $1/7$ .

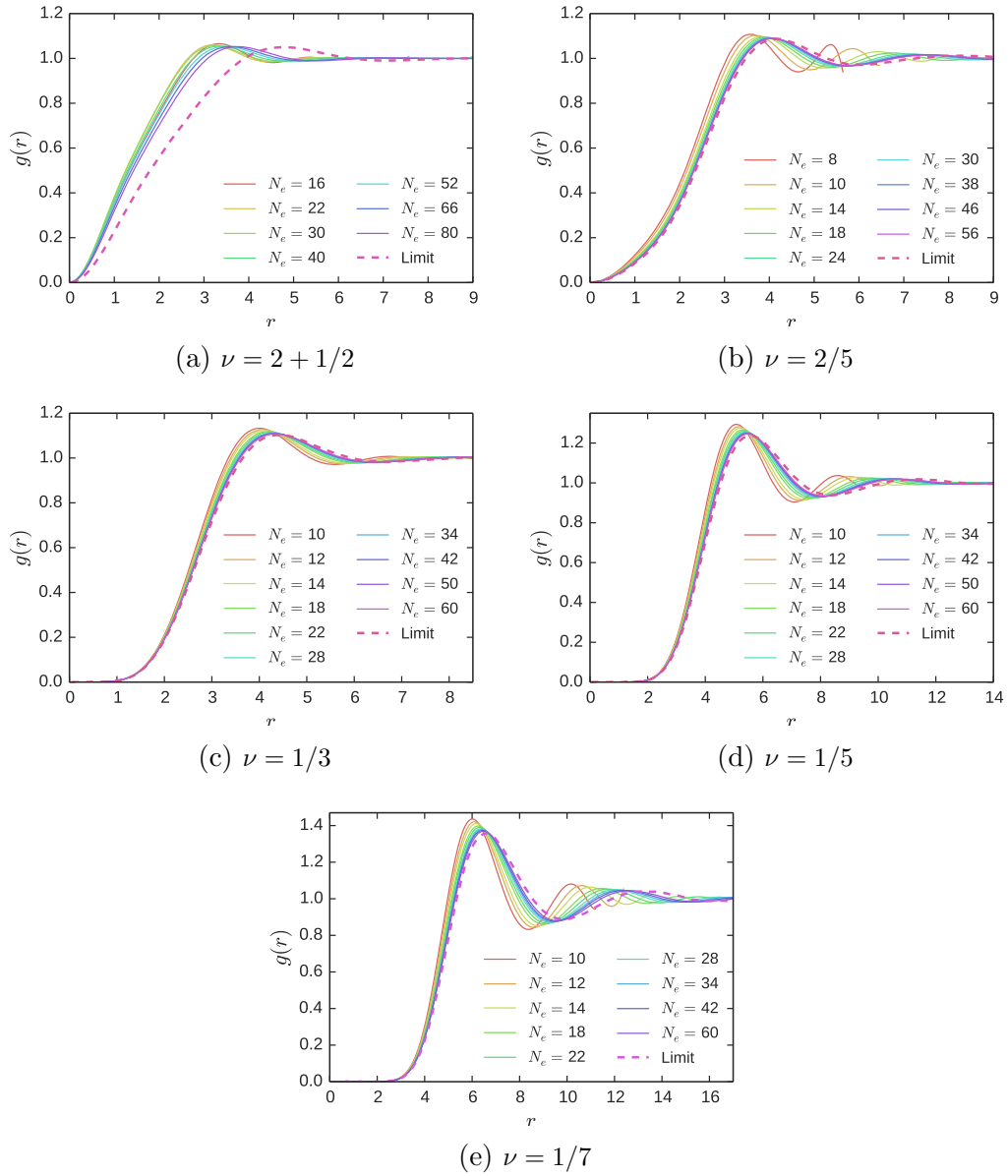


Figure 6.8: Pair correlation functions at finite sizes and in the thermodynamic limit for the following trial wavefunctions and filling factors: Moore-Read at  $\nu = 2 + 1/2$  (6.8a), composite fermions at  $\nu = 2/5$  (6.8b) and Laughlin at  $\nu = 1/3$  (6.8c),  $1/5$  (6.8d) and  $1/7$  (6.8e).

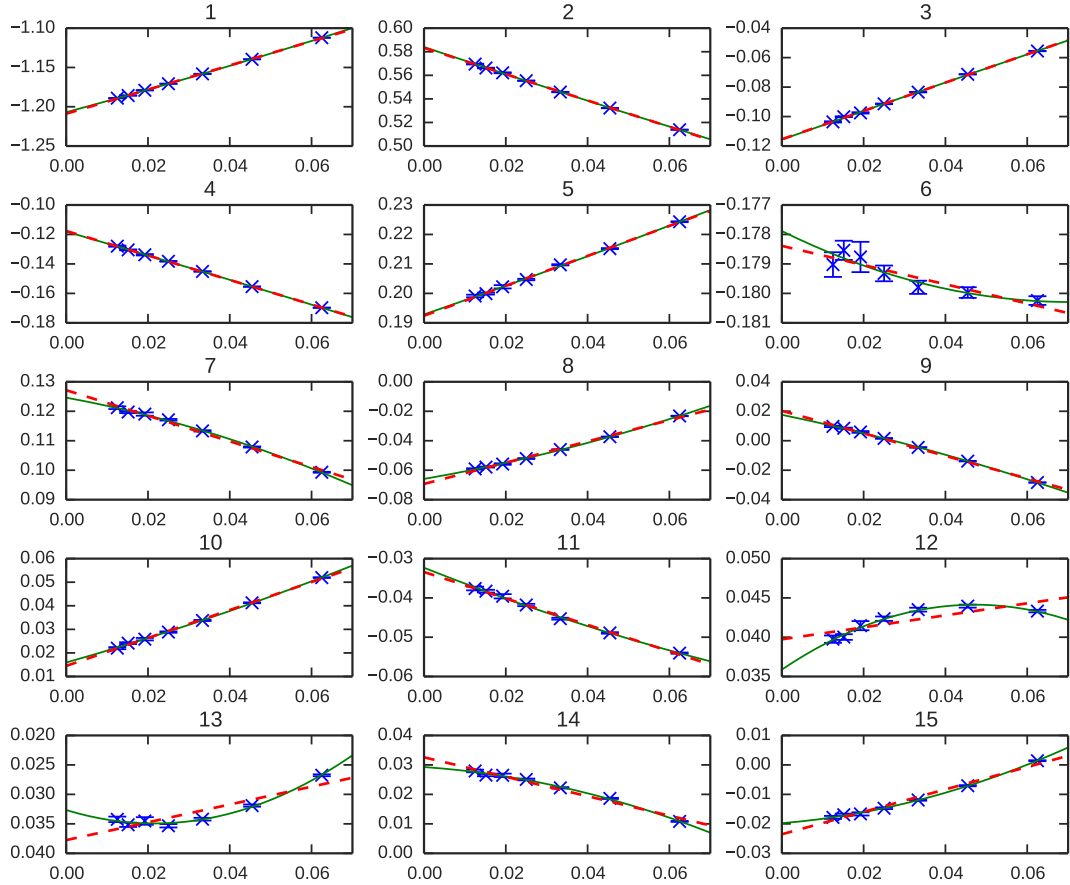


Figure 6.9: Expansion coefficients of the Moore-Read  $\nu = 2 + 1/2$  wavefunction in the orthogonal spherical decomposition, obtained using inner products, plotted against  $1/N_e$ . The first 15 coefficients are shown together with linear (red, dotted) and parabolic (green, solid) least squares fits.

# Chapter 7

## Summary and outlook

The principal focus of this work has been the study of trial wavefunctions describing the fractional quantum Hall effect. Our main contributions to this field consist firstly of techniques for lowest Landau projection, which has been problematic in the past although it is a feature of most proposed trial states. Secondly we have developed a method for analysing pair correlation functions which gives a unique characterisation and allows scaling to macroscopic sizes.

We have investigated the states known as reverse flux composite fermions, whose numerical evaluation was prohibitively time consuming until the advent of several improvements of the approximative Jain-Kamilla projection. These wavefunctions were demonstrated to yield good descriptions of the exact states also in contexts previously unexamined; notably, systems at higher excited energies and at fluxes other than those of the incompressible ground state. The results from the JK approximation were close but slightly less favourable as compared to exact projection, obtained using the energy projection scheme introduced by us.

It is still not fully settled which trial wavefunction gives the best description of the quantum Hall plateau at filling factor  $\nu = 12/5$ . This is an interesting question as different proposals predict distinct topological excitations, including several types of nonabelian quasiparticles. With this in mind we have studied trial wavefunctions for excitations of the Bonderson-Slingerland state at this filling. Similarly to previously published results on the ground states, the variational energies are shown to be small, although not as close to the exact results as is the case for many trial states on different fillings (this tends to be true of second Landau level states as compared to those in the first Landau level). We also saw that the nonabelian excitations of the pfaffian sector generally have lower energies than the abelian ones of the composite fermion

sector. The results using Jain-Kamilla and energy projection are comparable, with no consistent preference for either.

Next we turned to a set of modifications of any FQHE trial wavefunction, termed modified states and parametrised by a real number  $d$ . Positive  $d$  raise the exponents of polynomials in relative coordinates; increasing the correlations before projection, after which their action is harder to predict. Before now these have been difficult to study numerically due to the effect of the projection operator, which can now be handled using the energy projection.

The modification yields significant improvement to the Laughlin wavefunction, removing a large fraction of the excess variational energy and giving an impressive overlap with exact eigenstates also for the largest systems that were studied. Investigations of the pair correlation function revealed that the modification increases the oscillations of the Laughlin state so as to better match those of the exact Coulomb states. The value of  $d$  corresponding to the minimal energy was seen to have a slight increase with the number of particles, and we also saw that the optimal  $d$  is larger for lower density systems.

We gave extra attention to the parameter value  $d = 1$ , whose corresponding wavefunction can be interpreted as a special case of the reverse flux composite fermion states. Thus the Jain-Kamilla projection is also available, facilitating treatment of larger system sizes. With this we remove any doubt that the improvement of the ground state is stable also in the thermodynamic limit. The case is not so clear for a direct translation of the modification to the first band of excited states, however, where the regular  $d = 0$  states yield lower energies than the modified  $d = 1$  states for some values of the angular momentum. The minimal gaps to neutral excitations are the same in the thermodynamic limit up to statistical error.

Applying the modification in the same form to various composite fermion states also gave reductions in the variational energy, but not as dramatic as in the Laughlin case. In line with this the behaviour of the Coulomb state pair correlations was not as readily duplicated. A qualitative difference between the energy projected regular and reverse flux composite fermions was observed in that the latter had a better fit with the exact system when using negative parameters  $d < 0$ , whereas the former benefited from positive values.

In the final section the pair correlation function was the quantity of interest. We constructed an orthogonal decomposition motivated by the lack of a consistent and quantitative parametrisation in the literature, and showed that it has advantages over the preexisting decomposition introduced by Girvin.

Specifically, the coefficients of the new decomposition were demonstrated to be considerably more stable with the number of basis functions and particles, when obtained using standard techniques.

The new expansion makes it possible to scale the correlation functions to the thermodynamic limit, and this was done for a number of states. A smooth convergence with system size up to the limit was observed for lowest Landau level wavefunctions, while the behaviour was more complicated for the second Landau level Moore-Read state. The exact behaviour could be illuminated by studying larger system sizes.

Several avenues of further research are suggested by the investigations in this work. One may construct other excitations of the Bonderson-Slingerland state than those studied here; notably the quasielectrons. Including higher energy excitations should also improve the lower energies when diagonalising the Hamiltonian in the trial state space.

Different implementations of the projection of the BS state would also be possible by multiplication in momentum space, and a more thorough investigation of the effect of varying the Hamiltonian would be pertinent. The same goes for pair optimisations of the wavefunctions. Finally it is possible to mix the excitations in the composite fermion and pfaffian sector by diagonalising the Hamiltonian in the shared space.

The form of the modified states that has been studied is only one possibility. It is not difficult to conceive of natural extensions, involving more parameters, appropriate for various wavefunctions. Considering Laughlin quasiholes one can have different modification factors for the ground state and excitation components. Composite fermion wavefunctions might be improved by using different factors associated with each CF Landau level; this concept is yet clearer when considering the hierarchical forms. Finally pfaffian factors, being constituents of both the Moore-Read and Bonderson-Slingerland states, can be written as antisymmetrised two-layer composite fermion states with separate intra-layer and inter-layer modification factors. It is also possible to alter the form of the modification itself, e.g. using an exponential rather than a polynomial form as suggested by Girvin and Jach.

It would also be interesting to investigate in more detail the effect of the modified Laughlin wavefunctions on the plasma analogy, and see if they can throw some light on the transition from an incompressible electron liquid to a Wigner crystal. In addition the energy projection could be useful for many other states, including hierarchy wavefunctions on the torus, and potentially

other purposes than projection such as explicit symmetrisation and antisymmetrisation.

We have computed the thermodynamic limit of the pair correlation functions of several prominent trial wavefunctions, but there are many more open to the same treatment. Pair correlations of exact eigenstates of the Hamiltonian could also be extrapolated in the same manner. These results can be used to compute additional quantities, notably the single mode approximation for neutral excitations. Furthermore, the density profile of a quasihole is analogous to the pair correlation function, and would presumably also yield a well defined macroscopic limit.

The coefficients can potentially be used to compare different trial wavefunctions at the same filling fraction, and also it would be interesting to compare their limits to computations performed on the disk. It might also be possible to generalise the expansion to the torus geometry. Finally an analytic proof showing that the Gram-Schmidt procedure results in the expansion basis is desirable.

Graphene represents another intriguing two dimensional topological condensed matter system [116, 117]. In addition to other interesting features it has been shown to exhibit both the integer [118] and fractional [119] quantum Hall effects, the latter also at even denominator filling fractions [120]. Variational trial wavefunctions have been useful in describing phases also of this system [121], some of which are related to the fractional quantum Hall effect trial states described in this work. Therefore we expect that techniques introduced here can also be useful in studies of graphene.

# Appendix A

## The $\nu = 1$ pair correlation function on the sphere

This proof was done in collaboration with Niall Moran.

We want to find an expression for the pair correlation function (2.39)

$$g(r_{12}) = \frac{N_e(N_e - 1)}{A\rho^2} \int \prod_{i>1} dS_i |\Psi(\mathbf{r}_2 - \mathbf{r}_{12}, \mathbf{r}_2, \dots, \mathbf{r}_N)|^2, \quad (\text{A.1})$$

for a system on the sphere.

In general, when the wavefunction  $\Psi$  in question is a single determinant, we have  $\langle \mathbf{r}_j | \Psi \rangle = \Psi(\mathbf{r}_j) = \frac{1}{\sqrt{N_e!}} \text{Det}[\phi_i(\mathbf{r}_j)]$  where  $\phi_i$  are the occupied single particle orbitals. Removing state  $k$ , in this case the one corresponding to  $\mathbf{r}_1$ , gives

$$\langle \mathbf{r}_{j>1} | a_k | \Psi \rangle = \frac{1}{\sqrt{N_e - 1}} \text{Det}[\phi_{i \neq k}(\mathbf{r}_{j>1})], \quad (\text{A.2})$$

where  $a_k$  is the annihilation operator.

We will use the decomposition of a determinant into its minors,

$$\text{Det}[M_{ij}] = \sum_{k=1}^n (-1)^{k+t} M_{kt} \text{Det}[M_{i \neq k, j \neq t}], \quad (\text{A.3})$$

the following identity in the space of  $N_e - 1$  particles,

$$\int \prod_{j>1} dS_j |\mathbf{r}_{j>1}\rangle \langle \mathbf{r}_{j>1}| = \mathbf{1}, \quad (\text{A.4})$$

and the fact that  $\Psi$  with one state removed yields an orthonormal set:

$$\langle \Psi | a_k^\dagger a_l | \Psi \rangle = \delta_{kl}. \quad (\text{A.5})$$

Choosing  $t = 1$ , we first find an expression for the expectation value of the density:

$$\begin{aligned}
\rho(\mathbf{r}_1) &= N_e \int \prod_{i>1} dS_i |\Psi|^2 = \frac{N_e}{N_e!} \int \prod_{i>1} dS_i \text{Det}[\phi_i^*(\mathbf{r}_j)] \text{Det}[\phi_i(\mathbf{r}_j)] \\
&= \frac{N_e}{N_e!} \int \prod_{i>1} dS_i \sum_{k=1}^{N_e} \phi_k^*(\mathbf{r}_1) (-1)^{k+1} \text{Det}[\phi_{i \neq k}(\mathbf{r}_{j>1})] \times \\
&\quad \sum_{l=1}^{N_e} \phi_l(\mathbf{r}_1) (-1)^{l+1} \text{Det}[\phi_{i \neq l}(\mathbf{r}_{j>1})] \\
&= \frac{N_e(N_e - 1)!}{N_e!} \sum_{k,l=1}^{N_e} \phi_k^*(\mathbf{r}_1) \phi_l(\mathbf{r}_1) (-1)^{k+l} \times \\
&\quad \langle \Psi | a_k^\dagger \left( \int \prod_{i>1} dS_i |\mathbf{r}_{j>1}\rangle \langle \mathbf{r}_{j>1}| \right) a_l | \Psi \rangle \\
&= \sum_{k,l=1}^{N_e} \phi_k^*(\mathbf{r}_1) \phi_l(\mathbf{r}_1) (-1)^{k+l} \langle \Psi | a_k^\dagger a_l | \Psi \rangle = \sum_{k=1}^{N_e} |\phi_k(\mathbf{r}_1)|^2 . \tag{A.6}
\end{aligned}$$

In a similar manner we can find an expression for the pair correlation function:

$$\begin{aligned}
g(|\mathbf{r}_1 - \mathbf{r}_2|) &= \frac{N_e(N_e - 1)}{\rho^2} \int \prod_{i>2} dS_i |\Psi(\mathbf{r}_1, \mathbf{r}_2, \dots, \mathbf{r}_{N_e})|^2 \\
&= \frac{1}{\rho^2} \sum_{k,l=1}^{N_e} \left( |\phi_k(\mathbf{r}_1)|^2 |\phi_l(\mathbf{r}_2)|^2 - \phi_k^*(\mathbf{r}_1) \phi_l(\mathbf{r}_1) \phi_l^*(\mathbf{r}_2) \phi_k(\mathbf{r}_2) \right) . \tag{A.7}
\end{aligned}$$

At this point we turn to the state  $\nu = 1$ , i.e. a determinant consisting of all the lowest Landau level functions for the chosen  $N_\Phi$ . According to (2.25) these are, in terms of spinor coordinates,

$$\phi_k(u, v) = \sqrt{\frac{2Q+1}{4\pi Q} \binom{2Q}{k}} (-1)^k u^k v^{2Q-k} , \tag{A.8}$$

with  $k \in \{0, 1, \dots, 2Q\}$  and  $2Q = N_\Phi$ . As a consistency check we find using (A.6) that the density is  $\rho = N_e/A$ . Following (A.7) this yields for the pair correlation function, in terms of the chord distance  $r = 2R|u_1 v_2 - u_2 v_1|$ ,

$$g_1(r) = 1 - \left(1 - |u_1 v_2 - u_2 v_1|^2\right)^{2Q} = 1 - \left(1 - \frac{r^2/2}{2Q}\right)^{2Q} . \tag{A.9}$$

In terms of the unit distance (2.34) we find  $g_1(\eta) = 1 - (1 - \eta^2)^{2Q}$ . Note that

expressions for the pair correlation functions of all the excited states of  $\nu = 1$  can be obtained in the same manner, due to the fact that they all consist of a single Slater determinant.

# Appendix B

## Proof of spherical basis orthonormality

We want to prove that the following functions are orthonormal:

$$G_n(\eta) = \mathcal{N}_n \eta^2 (1 - \eta^2)^{2Q-n} J_{n-1}^{(2,4Q+1-2n)}(1 - 2\eta^2)$$
$$\mathcal{N}_n = \sqrt{\frac{(4Q+2-n)(4Q+1-n)(4Q-2n+1)}{4\pi Q n(n+1)}}, \quad (\text{B.1})$$

where  $1 \leq n \leq 2Q$ , under the integration measure  $dS = 4\pi Q \eta d\eta$ .

### Orthogonality

We begin by showing that they are orthogonal. For this the normalisation is irrelevant, and we ignore all constants. Note that although the inner product  $\langle G_n, G_m \rangle$  is reminiscent of that in the orthogonality relation between two Jacobi polynomials  $J_k^{(\alpha, \beta)}$  [30] we cannot use this relation directly. This is because the relation assumes that the parameters  $(\alpha, \beta)$  are equal in the two polynomials, which is not the case for  $G_n$  and  $G_m$  when  $n \neq m$ .

As a first step we substitute the variable  $x = 1 - 2\eta^2$  for  $\eta$ . This leads to  $dS = -\pi Q dx$  and gives the integration limits  $x(\eta = 0) = 1$  and  $x(\eta = 1) = -1$ . Thus (B.1) yields the following inner product:

$$\langle G_n, G_m \rangle \propto \int_{-1}^1 dx \left(\frac{1-x}{2}\right)^2 \left(\frac{1+x}{2}\right)^{4Q-n-m} \times$$
$$J_{n-1}^{(2,4Q+1-2n)}(x) J_{m-1}^{(2,4Q+1-2m)}(x). \quad (\text{B.2})$$

At this point it is convenient to introduce the shorthand

$$\begin{aligned} A(x) &= 1 - x , \\ B(x) &= 1 + x . \end{aligned} \tag{B.3}$$

We note that  $A(-1)B(-1) = A(1)B(1) = 0$ . With this convention Rodrigues' formula [30] reads

$$J_k^{(\alpha,\beta)}(x) = \frac{(-1)^k}{2^k k!} A^{-\alpha} B^{-\beta} \frac{d^k}{dx^k} (A^{\alpha+k} B^{\beta+k}) . \tag{B.4}$$

Using this (B.2) can be written as

$$\langle G_n, G_m \rangle \propto \int_{-1}^1 dx A^{-2} B^{n+m-2-4Q} \frac{d^{n-1}}{dx^{n-1}} (A^{n+1} B^{4Q-n}) \frac{d^{m-1}}{dx^{m-1}} (A^{m+1} B^{4Q-m}) . \tag{B.5}$$

We will show that this equals zero when  $n \neq m$  using repeated integration by parts. In preparation we observe that

$$\text{The polynomial } \frac{d^k}{dx^k} (A^p B^q) \text{ has a factor } AB \text{ when } p > k < q . \tag{B.6}$$

Without loss of generality we assume  $n < m$ . A first integration by parts leaves (B.5) as

$$\begin{aligned} \langle G_n, G_m \rangle &\propto \left[ \left\{ A^{-2} B^{n+m-2-4Q} \frac{d^{n-1}}{dx^{n-1}} (A^{n+1} B^{4Q-n}) \right\} \left\{ \frac{d^{m-2}}{dx^{m-2}} (A^{m+1} B^{4Q-m}) \right\} \right]_{-1}^1 \\ &- \int_{-1}^1 dx \frac{d}{dx} \left\{ A^{-2} B^{n+m-2-4Q} \frac{d^{n-1}}{dx^{n-1}} (A^{n+1} B^{4Q-n}) \right\} \frac{d^{m-2}}{dx^{m-2}} (A^{m+1} B^{4Q-m}) . \end{aligned} \tag{B.7}$$

First we show that the boundary term is zero. We note that the first factor  $A^{-2} B^{n+m-4Q} \frac{d^{n-1}}{dx^{n-1}} (A^{n+1} B^{4Q-n})$  is zero or a polynomial of order  $m - 2$ , and therefore regular.

Next we examine the second factor:  $\frac{d^{m-2}}{dx^{m-2}} (A^{m+1} B^{4Q-m})$ . Looking at the derivative and the polynomial powers we have that  $m - 2 < m + 1$  and that  $m - 2 < 4Q - m$  (since  $m \leq 2Q$ ). (B.6) therefore implies that it has a factor  $AB$ . Thus the boundary term is a product of regular terms and a factor  $AB$ , and therefore equals zero when evaluated at both boundaries  $x = -1$  and  $x = 1$ .

Applying further integrations by parts will produce boundary terms similar

to that in (B.7) but with derivatives acting on the whole of the first factor, in increasing order, while the derivative in the second factor decreases in order. This does not change the reasoning in the previous paragraph, and we see that all boundary terms vanish. Thus the result after  $k$  integrations by parts is

$$\langle G_n, G_m \rangle \propto \int_{-1}^1 dx \frac{d^k}{dx^k} \left\{ A^{-2} B^{n+m-2-4Q} \frac{d^{n-1}}{dx^{n-1}} (A^{n+1} B^{4Q-n}) \right\} \times \frac{d^{m-1-k}}{dx^{m-1-k}} (A^{m+1} B^{4Q-m}) . \quad (\text{B.8})$$

We see that the first factor in (B.8) will have order zero, i.e. be a constant, when  $k = m - 2$ . At this point the integrand is a pure differential:

$$\langle G_n, G_m \rangle \propto \int_{-1}^1 dx \frac{d}{dx} (A^{m+1} B^{4Q-m}) = \left[ A^{m+1} B^{4Q-m} \right]_{-1}^1 = 0 , \quad (\text{B.9})$$

concluding our proof of orthogonality.

### Orthonormality

To prove that the functions are orthonormal it only remains to show that  $\langle G_n, G_n \rangle = 1$ . In this case the caveat no longer holds, however, that we cannot use the Jacobi polynomial orthogonality relation directly, since the two functions now have the same parameters. With some algebra this relation shows that the functions are orthonormal.

# Bibliography

- [1] A. H. MacDonald. Introduction to the physics of the quantum Hall regime. 1994, arXiv:cond-mat/9410047.
- [2] Steven M. Girvin. The quantum Hall effect: Novel excitations and broken symmetries. 1998, arXiv:cond-mat/9907002.
- [3] J. K. Jain. *Composite Fermions*. Cambridge University Press, 2007.
- [4] M. O. Goerbig. Quantum Hall effects. 2009, arXiv:0909.1998.
- [5] E. H. Hall. On a new action of the magnet on electric currents. *American Journal of Mathematics*, 2(3):287–292, 1879.
- [6] K. v. Klitzing, G. Dorda, and M. Pepper. New method for high-accuracy determination of the fine-structure constant based on quantized Hall resistance. *Phys. Rev. Lett.*, 45:494–497, Aug 1980.
- [7] Horst L. Störmer, Daniel C. Tsui, and Arthur C. Gossard. The fractional quantum Hall effect. *Rev. Mod. Phys.*, 71:S298–S305, Mar 1999.
- [8] D. C. Tsui, H. L. Störmer, and A. C. Gossard. Two-dimensional magnetotransport in the extreme quantum limit. *Phys. Rev. Lett.*, 48:1559–1562, May 1982.
- [9] H. L. Störmer, A. Chang, D. C. Tsui, J. C. M. Hwang, A. C. Gossard, and W. Wiegmann. Fractional quantization of the Hall effect. *Phys. Rev. Lett.*, 50:1953–1956, Jun 1983.
- [10] E. E. Mendez, M. Heiblum, L. L. Chang, and L. Esaki. High-magnetic-field transport in a dilute two-dimensional electron gas. *Phys. Rev. B*, 28:4886–4888, Oct 1983.
- [11] A. M. Chang, P. Berglund, D. C. Tsui, H. L. Störmer, and J. C. M. Hwang. Higher-order states in the multiple-series, fractional, quantum Hall effect. *Phys. Rev. Lett.*, 53:997–1000, Sep 1984.

- [12] R. Willett, H.L. Störmer, D.C. Tsui, A.C. Gossard, J.H. English, and K.W. Baldwin. Fractional quantum Hall effect in extremely high mobility GaAs/(AlGa)As heterostructures. *Surface Science*, 196(13):257 – 262, 1988.
- [13] V. J. Goldman, M. Shayegan, and D. C. Tsui. Evidence for the fractional quantum Hall state at  $\nu = \frac{1}{7}$ . *Phys. Rev. Lett.*, 61:881–884, Aug 1988.
- [14] W. Pan, K. W. Baldwin, K. W. West, L. N. Pfeiffer, and D. C. Tsui. Fractional quantum hall effect at landau level filling  $\nu = 4/11$ . *Phys. Rev. B*, 91:041301, Jan 2015, arXiv:1412.7451.
- [15] R. Willett, J. P. Eisenstein, H. L. Störmer, D. C. Tsui, A. C. Gossard, and J. H. English. Observation of an even-denominator quantum number in the fractional quantum Hall effect. *Phys. Rev. Lett.*, 59:1776–1779, Oct 1987.
- [16] J. S. Xia, W. Pan, C. L. Vicente, E. D. Adams, N. S. Sullivan, H. L. Stormer, D. C. Tsui, L. N. Pfeiffer, K. W. Baldwin, and K. W. West. Electron correlation in the second Landau level: A competition between many nearly degenerate quantum phases. *Phys. Rev. Lett.*, 93:176809, Oct 2004, arXiv:cond-mat/0406724.
- [17] J. K. Jain. Composite-fermion approach for the fractional quantum Hall effect. *Phys. Rev. Lett.*, 63:199–202, Jul 1989.
- [18] J. K. Jain and R. K. Kamilla. Composite fermions in the hilbert space of the lowest electronic Landau level. *Int. J. Mod. Phys. B*, 11:2621, 1997, arXiv:cond-mat/9704031.
- [19] Gunnar Möller and Steven H. Simon. Composite fermions in a negative effective magnetic field: A monte carlo study. *Phys. Rev. B*, 72:045344, Jul 2005, arXiv:cond-mat/0502514.
- [20] Simon C. Davenport and Steven H. Simon. Spinful composite fermions in a negative effective field. *Phys. Rev. B*, 85:245303, Jun 2012, arXiv:1203.0004.
- [21] Sutirtha Mukherjee and Sudhansu S. Mandal. Incompressible states of the interacting composite fermions in negative effective magnetic fields at  $\nu = 4/13$ ,  $5/17$ , and  $3/10$ . *Phys. Rev. B*, 92:235302, Dec 2015, arXiv:1510.03555.

## BIBLIOGRAPHY

- [22] M. Fremling, J. Fulsebakke, N. Moran, and J. K. Slingerland. Energy projection and modified Laughlin states. *Phys. Rev. B*, 93:235149, Jun 2016, arXiv:1601.06736.
- [23] S. M. Girvin and Terrence Jach. Formalism for the quantum Hall effect: Hilbert space of analytic functions. *Phys. Rev. B*, 29:5617–5625, May 1984.
- [24] S. M. Girvin, A. H. MacDonald, and P. M. Platzman. Magneto-roton theory of collective excitations in the fractional quantum Hall effect. *Phys. Rev. B*, 33:2481–2494, Feb 1986.
- [25] Theodore G Northrop. The guiding center approximation to charged particle motion. *Annals of Physics*, 15(1):79 – 101, 1961.
- [26] F. D. M. Haldane. Fractional quantization of the Hall effect: A hierarchy of incompressible quantum fluid states. *Phys. Rev. Lett.*, 51:605–608, Aug 1983.
- [27] Steven H. Simon, E. H. Rezayi, and Nigel R. Cooper. Pseudopotentials for multiparticle interactions in the quantum Hall regime. *Phys. Rev. B*, 75:195306, May 2007, arXiv:cond-mat/0701260.
- [28] E. J. Bergholtz and A. Karlhede. Quantum hall system in Tao-Thouless limit. *Phys. Rev. B*, 77:155308, Apr 2008, arXiv:0712.1927.
- [29] Rachel Wooten and Joseph Macek. Configuration interaction matrix elements for the quantum Hall effect. Aug 2014, arXiv:1408.5379.
- [30] Milton Abramowitz and Irene A. Stegun. *Handbook of Mathematical Functions*. United States National Bureau of Standards, 1964.
- [31] Tai Tsun Wu and Chen Ning Yang. Dirac monopole without strings: Monopole harmonics. *Nuclear Physics B*, 107(3):365 – 380, 1976.
- [32] J. E. Avron, R. Seiler, and P. G. Zograf. Viscosity of quantum Hall fluids. *Phys. Rev. Lett.*, 75:697–700, Jul 1995.
- [33] N. Read. Non-abelian adiabatic statistics and hall viscosity in quantum Hall states and  $p_x + ip_y$  paired superfluids. *Phys. Rev. B*, 79:045308, Jan 2009, arXiv:0805.2507.

- [34] M. Fremling. Coherent state wave functions on a torus with a constant magnetic field. *J. Phys. A: Math. Theor*, 46:275302, Jun 2013, arXiv:1302.6471.
- [35] D. Yoshioka, B. I. Halperin, and P. A. Lee. Ground state of two-dimensional electrons in strong magnetic fields and  $\frac{1}{3}$  quantized Hall effect. *Phys. Rev. Lett.*, 50:1219–1222, Apr 1983.
- [36] F. D. M. Haldane and E. H. Rezayi. Periodic Laughlin-Jastrow wave functions for the fractional quantized Hall effect. *Phys. Rev. B*, 31:2529–2531, Feb 1985.
- [37] J. Shabani, T. Gokmen, Y. T. Chiu, and M. Shayegan. Evidence for developing fractional quantum Hall states at even denominator  $1/2$  and  $1/4$  fillings in asymmetric wide quantum wells. *Phys. Rev. Lett.*, 103:256802, Dec 2009.
- [38] D. R. Luhman, W. Pan, D. C. Tsui, L. N. Pfeiffer, K. W. Baldwin, and K. W. West. Observation of a fractional quantum Hall state at  $\nu = 1/4$  in a wide gas quantum well. *Phys. Rev. Lett.*, 101:266804, Dec 2008, arXiv:0810.2274.
- [39] K. Park, V. Melik-Alaverdian, N. E. Bonesteel, and J. K. Jain. Possibility of p-wave pairing of composite fermions at  $\nu = \frac{1}{2}$ . *Phys. Rev. B*, 58:R10167–R10170, Oct 1998, arXiv:cond-mat/9806271.
- [40] Csaba Töke, Michael R. Peterson, Gun Sang Jeon, and Jainendra K. Jain. Fractional quantum Hall effect in the second Landau level: The importance of inter-composite-fermion interaction. *Phys. Rev. B*, 72:125315, Sep 2005, arXiv:cond-mat/0504571.
- [41] V. J. Goldman and B. Su. Resonant tunneling in the quantum Hall regime: measurement of fractional charge. *Science*, 267:1010, 1995.
- [42] L. Saminadayar, D. C. Glattli, Y. Jin, and B. Etienne. Observation of the  $e/3$  fractionally charged Laughlin quasiparticle. *Phys. Rev. Lett.*, 79:2526–2529, Sep 1997, arXiv:cond-mat/9706307.
- [43] R. de Picciotto, M. Reznikov, M. Heiblum, V. Umansky, G. Bunin, and D. Mahalu. Direct observation of a fractional charge. *Nature*, 389:162, 1997, arXiv:cond-mat/9707289.

- [44] J. M. Leinaas and J. Myrheim. On the theory of identical particles. *Nuovo Cimento B Serie*, 37:1–23, January 1977.
- [45] F. Wilczek. Quantum Mechanics of Fractional-Spin Particles. *Physical Review Letters*, 49:957–959, October 1982.
- [46] F. E. Camino, Wei Zhou, and V. J. Goldman. Realization of a Laughlin quasiparticle interferometer: Observation of fractional statistics. *Phys. Rev. B*, 72:075342, Aug 2005, arXiv:cond-mat/0502406.
- [47] W. Pan, J. S. Xia, H. L. Störmer, D. C. Tsui, C. Vicente, E. D. Adams, N. S. Sullivan, L. N. Pfeiffer, K. W. Baldwin, and K. W. West. Experimental studies of the fractional quantum Hall effect in the first excited Landau level. *Phys. Rev. B*, 77:075307, Feb 2008, arXiv:0801.1318.
- [48] Gregory Moore and Nicholas Read. Nonabelions in the fractional quantum hall effect. *Nuclear Physics B*, 360(23):362 – 396, 1991.
- [49] Chetan Nayak and Frank Wilczek.  $2n$ -quasihole states realize  $2^{n-1}$ -dimensional spinor braiding statistics in paired quantum Hall states. *Nuclear Physics B*, 479(3):529 – 553, 1996, arXiv:cond-mat/9605145.
- [50] Michael H. Freedman, Alexei Kitaev, and Zhenghan Wang. Simulation of topological field theories by quantum computers. *Commun. Math. Phys.*, 227:587–603, 2002.
- [51] A.Yu. Kitaev. Fault-tolerant quantum computation by anyons. *Annals of Physics*, 303(1):2 – 30, 2003, arXiv:quant-ph/9707021.
- [52] Chetan Nayak, Steven H. Simon, Ady Stern, Michael Freedman, and Sankar Das Sarma. Non-abelian anyons and topological quantum computation. *Rev. Mod. Phys.*, 80:1083–1159, Sep 2008, arXiv:0707.1889.
- [53] R. B. Laughlin. Anomalous quantum Hall effect: An incompressible quantum fluid with fractionally charged excitations. *Phys. Rev. Lett.*, 50:1395–1398, May 1983.
- [54] H. Deng Yang Liu, M. Shayegan, L.N. Pfeiffer, K.W. West, and K.W. Baldwin. Composite fermions waltz to the tune of a Wigner crystal. Oct 2014, arXiv:1410.3435.

- [55] J. M. Caillol, D. Levesque, J. J. Weis, and J. P. Hansen. A Monte Carlo study of the classical two-dimensional one-component plasma. *Journal of Statistical Physics*, 28(2):325–349, June 1982.
- [56] Daniel Arovas, J. R. Schrieffer, and Frank Wilczek. Fractional statistics and the quantum Hall effect. *Phys. Rev. Lett.*, 53:722–723, Aug 1984.
- [57] Heidi Kjønsberg and Jan Myrheim. Numerical study of charge and statistics of Laughlin quasiparticles. *International Journal of Modern Physics A*, 14(04):537–557, 1999.
- [58] B. I. Halperin. Statistics of quasiparticles and the hierarchy of fractional quantized Hall states. *Phys. Rev. Lett.*, 52:1583–1586, Apr 1984.
- [59] T. H. Hansson, C.-C. Chang, J. K. Jain, and S. Viefers. Composite-fermion wave functions as correlators in conformal field theory. *Phys. Rev. B*, 76:075347, Aug 2007, arXiv:0704.0570.
- [60] T. H. Hansson, M. Hermanns, and S. Viefers. Quantum Hall quasielectron operators in conformal field theory. *Phys. Rev. B*, 80:165330, Oct 2009, arXiv:0903.0937.
- [61] J. Suorsa, S. Viefers, and T. H. Hansson. Quasihole condensates in quantum Hall liquids. *Phys. Rev. B*, 83:235130, Jun 2011, arXiv:1004.3657.
- [62] Thomas Kvorning. Quantum Hall hierarchy in a spherical geometry. *Phys. Rev. B*, 87:195131, May 2013, arXiv:1302.3808.
- [63] M. Hermanns, J. Suorsa, E. J. Bergholtz, T. H. Hansson, and A. Karlhede. Quantum Hall wave functions on the torus. *Phys. Rev. B*, 77:125321, Mar 2008, arXiv:0711.4684.
- [64] M. Fremling, T. H. Hansson, and J. Suorsa. Hall viscosity of hierarchical quantum Hall states. *Phys. Rev. B*, 89:125303, Mar 2014, arXiv:1312.6038.
- [65] V. Melik-Alaverdian and N. E. Bonesteel. Monte Carlo comparison of quasielectron wave functions. *Phys. Rev. B*, 58:1451–1456, Jul 1998, arXiv:cond-mat/9807343.
- [66] Gun Sang Jeon and Jainendra K. Jain. Nature of quasiparticle excitations in the fractional quantum Hall effect. *Phys. Rev. B*, 68:165346, Oct 2003, arXiv:cond-mat/0310708.

- [67] X. G. Wu and J. K. Jain. Excitation spectrum and collective modes of composite fermions. *Phys. Rev. B*, 51:1752–1761, Jan 1995.
- [68] Jainendra K. Jain, Chia-Chen Chang, Gun Sang Jeon, and Michael R. Peterson. Composite fermions in the neighborhood of  $\nu = 1/3$ . *Solid State Communications*, 127(12):805 – 811, 2003, arXiv:cond-mat/0309168.
- [69] Ajit C. Balram, Arkadiusz Wójs, and Jainendra K. Jain. State counting for excited bands of the fractional quantum Hall effect: Exclusion rules for bound excitons. *Phys. Rev. B*, 88:205312, Nov 2013.
- [70] W. P. Su. Statistics of the fractionally charged excitations in the quantum Hall effect. *Phys. Rev. B*, 34:1031–1033, Jul 1986.
- [71] H. Kjønsberg and J.M. Leinaas. Charge and statistics of quantum Hall quasi-particles a numerical study of mean values and fluctuations. *Nuclear Physics B*, 559(3):705 – 742, 1999, arXiv:cond-mat/9901266.
- [72] Gun Sang Jeon, Kenneth L. Graham, and Jainendra K. Jain. Berry phases for composite fermions: Effective magnetic field and fractional statistics. *Phys. Rev. B*, 70:125316, Sep 2004, arXiv:cond-mat/0407137.
- [73] Philippe Fransesco, Pierre Mathieu, and David Sénéchal. *Conformal Field Theory*. Springer-Verlag New York, Inc., 1997.
- [74] X.G. Wen. Theory of the edge excitations in FQH effects. *Int. J. Mod. Phys.*, B6:1711, 1992.
- [75] S. M. Girvin and A. H. MacDonald. Off-diagonal long-range order, oblique confinement, and the fractional quantum Hall effect. *Phys. Rev. Lett.*, 58:1252–1255, Mar 1987.
- [76] S. C. Zhang, T. H. Hansson, and S. Kivelson. Effective-field-theory model for the fractional quantum Hall effect. *Phys. Rev. Lett.*, 62:82–85, Jan 1989.
- [77] E. J. Bergholtz, T. H. Hansson, M. Hermanns, A. Karlhede, and S. Viefers. Quantum Hall hierarchy wave functions: From conformal correlators to Tao-Thouless states. *Phys. Rev. B*, 77:165325, Apr 2008, arXiv:0712.3848.

- [78] Martin Greiter, Xiao-Gang Wen, and Frank Wilczek. Paired Hall state at half filling. *Phys. Rev. Lett.*, 66:3205–3208, Jun 1991.
- [79] R. H. Morf. Transition from quantum Hall to compressible states in the second Landau level: New light on the  $\nu = 5/2$  enigma. *Phys. Rev. Lett.*, 80:1505–1508, Feb 1998.
- [80] E. H. Rezayi and F. D. M. Haldane. Incompressible paired Hall state, stripe order, and the composite fermion liquid phase in half-filled Landau levels. *Phys. Rev. Lett.*, 84:4685–4688, May 2000, arXiv:cond-mat/9906137.
- [81] Sung-Sik Lee, Shinsei Ryu, Chetan Nayak, and Matthew P. A. Fisher. Particle-hole symmetry and the  $\nu = \frac{5}{2}$  quantum Hall state. *Phys. Rev. Lett.*, 99:236807, Dec 2007.
- [82] Michael Levin, Bertrand I. Halperin, and Bernd Rosenow. Particle-hole symmetry and the Pfaffian state. *Phys. Rev. Lett.*, 99:236806, Dec 2007.
- [83] Xin Wan, Zi-Xiang Hu, E. H. Rezayi, and Kun Yang. Fractional quantum Hall effect at  $\nu = 5/2$ : Ground states, non-Abelian quasiholes, and edge modes in a microscopic model. *Phys. Rev. B*, 77:165316, Apr 2008.
- [84] Sergey Bravyi. Universal quantum computation with the  $\nu = 5/2$  fractional quantum Hall state. *Phys. Rev. A*, 73:042313, Apr 2006, arXiv:quant-ph/0511178.
- [85] N. Read and E. Rezayi. Beyond paired quantum Hall states: Parafermions and incompressible states in the first excited Landau level. *Phys. Rev. B*, 59:8084–8092, Mar 1999, arXiv:cond-mat/9809384.
- [86] N. Read and E. Rezayi. Quasiholes and fermionic zero modes of paired fractional quantum hall states: The mechanism for non-abelian statistics. *Phys. Rev. B*, 54:16864–16887, Dec 1996, arXiv:cond-mat/9609079.
- [87] N. Regnault and Th. Jolicoeur. Parafermionic states in rotating Bose-Einstein condensates. *Phys. Rev. B*, 76:235324, Dec 2007, arXiv:cond-mat/060155.
- [88] T. H. Hansson, M. Hermanns, N. Regnault, and S. Viefers. Conformal field theory approach to Abelian and non-Abelian quantum Hall quasi-electrons. *Phys. Rev. Lett.*, 102:166805, Apr 2009, arXiv:0810.0636.

- [89] B. Andrei Bernevig and F. D. M. Haldane. Clustering properties and model wave functions for non-Abelian fractional quantum Hall quasielectrons. *Phys. Rev. Lett.*, 102:066802, Feb 2009, arXiv:0810.2366.
- [90] Ivan D. Rodríguez, A. Sterdyniak, M. Hermanns, J. K. Slingerland, and N. Regnault. Quasiparticles and excitons for the Pfaffian quantum Hall state. *Phys. Rev. B*, 85:035128, Jan 2012, arXiv:1110.0454.
- [91] G. J. Sreejith, A. Wójs, and J. K. Jain. Unpaired composite fermion, topological exciton, and zero mode. *Phys. Rev. Lett.*, 107:136802, Sep 2011, arXiv:1106.0865.
- [92] Eddy Ardonne. Parafermion statistics and application to non-Abelian quantum Hall states. *Journal of Physics A: Mathematical and General*, 35(3):447, 2002, arXiv:cond-mat/0110108.
- [93] Parsa Bonderson and J. K. Slingerland. Fractional quantum Hall hierarchy and the second Landau level. *Phys. Rev. B*, 78:125323, Sep 2008, arXiv:0711.3204.
- [94] W. Pan, J.-S. Xia, V. Shvarts, D. E. Adams, H. L. Störmer, D. C. Tsui, L. N. Pfeiffer, K. W. Baldwin, and K. W. West. Exact quantization of the even-denominator fractional quantum Hall state at  $\nu = 5/2$  Landau level filling factor. *Phys. Rev. Lett.*, 83:3530–3533, Oct 1999, arXiv:cond-mat/9907356.
- [95] Parsa Bonderson, Adrian E. Feiguin, Gunnar Möller, and J. K. Slingerland. Competing topological orders in the  $\nu = 12/5$  quantum Hall state. *Phys. Rev. Lett.*, 108:036806, Jan 2012, arXiv:0901.4965.
- [96] G. J. Sreejith, C. Tóke, A. Wójs, and J. K. Jain. Bipartite composite fermion states. *Phys. Rev. Lett.*, 107:086806, Aug 2011.
- [97] M. Hermanns. Condensing non-Abelian quasiparticles. *Phys. Rev. Lett.*, 104:056803, Feb 2010, arXiv:0906.2073.
- [98] Arkadiusz Wójs. Transition from Abelian to non-Abelian quantum liquids in the second Landau level. *Phys. Rev. B*, 80:041104, Jul 2009, arXiv:0811.4072.
- [99] G. Möller and S. H. Simon. Paired composite-fermion wave functions. *Phys. Rev. B*, 77:075319, Feb 2008, arXiv:0708.2680.

## BIBLIOGRAPHY

- [100] Roger S. K. Mong, Michael P. Zaletel, Frank Pollmann, and Zlatko Papić. Fibonacci anyons and charge density order in the  $12/5$  and  $13/5$  plateaus. May 2015, arXiv:1505.02843.
- [101] Gilbert W Stewart. A Krylov–Schur algorithm for large eigenproblems. *SIAM Journal on Matrix Analysis and Applications*, 23(3):601–614, 2002.
- [102] Walter Edwin Arnoldi. The principle of minimized iterations in the solution of the matrix eigenvalue problem. *Quarterly of Applied Mathematics*, 9(1):17–29, 1951.
- [103] Cornelius Lanczos. *An iteration method for the solution of the eigenvalue problem of linear differential and integral operators*. United States Governm. Press Office Los Angeles, CA, 1950.
- [104] M.E.J. Newman and G. T. Barkema. *Monte Carlo Methods in Mathematical Physics*. Oxford University Press, 2002.
- [105] Nicholas Metropolis, Arianna W. Rosenbluth, Marshall N. Rosenbluth, Augusta H. Teller, and Edward Teller. Equation of state calculations by fast computing machines. *J. Chem. Phys.*, 21:1087, 1953.
- [106] Gautam Dev and J. K. Jain. Jastrow-Slater trial wave functions for the fractional quantum Hall effect: Results for few-particle systems. *Phys. Rev. B*, 45:1223–1230, Jan 1992.
- [107] N. E. Bonesteel. Composite fermions and the energy gap in the fractional quantum Hall effect. *Phys. Rev. B*, 51:9917–9921, Apr 1995.
- [108] V. Melik-Alaverdian and N. E. Bonesteel. Composite fermions and Landau-level mixing in the fractional quantum Hall effect. *Phys. Rev. B*, 52:R17032–R17035, Dec 1995, arXiv:cond-mat/9508060.
- [109] R. K. Kamilla, X. G. Wu, and J. K. Jain. Composite fermion theory of collective excitations in fractional quantum Hall effect. *Phys. Rev. Lett.*, 76:1332–1335, Feb 1996, arXiv:cond-mat/9511136.
- [110] M. Hermanns. Composite fermion states on the torus. *Phys. Rev. B*, 87:235128, Jun 2013, arXiv:1304.4486.

- [111] Piotr Sitko and Lucjan Jacak. Hartree-Fock ground state of the composite fermion metal. *Modern Physics Letters B*, 09(14):889–894, 1995, arXiv:cond-mat/9506018.
- [112] C. González-Ballester, L.M. Robledo, and G.F. Bertsch. Numeric and symbolic evaluation of the Pfaffian of general skew-symmetric matrices. *Computer Physics Communications*, 182(10):2213 – 2218, 2011, arXiv:1012.5022.
- [113] S. M. Girvin. Anomalous quantum Hall effect and two-dimensional classical plasmas: Analytic approximations for correlation functions and ground-state energies. *Phys. Rev. B*, 30:558–560, Jul 1984.
- [114] B. Jancovici. Exact results for the two-dimensional one-component plasma. *Phys. Rev. Lett.*, 46:386–388, Feb 1981.
- [115] Ward Cheney and David Kincaid. *Numerical Mathematics and Computing*. Brooks/Cole Cengage Learning, 2004.
- [116] K. S. Novoselov, A. K. Geim, S. V. Morozov, D. Jiang, Y. Zhang, S. V. Dubonos, I. V. Grigorieva, and A. A. Firsov. Electric field effect in atomically thin carbon films. *Science*, 306:666–669, Oct 2004, arXiv:cond-mat/0410550.
- [117] A. K. Geim and K. S. Novoselov. The rise of Graphene. *Nature*, 6:183–191, 2007, arXiv:cond-mat/0702595.
- [118] Yuanbo Zhang, Yan-Wen Tan, Horst L. Störmer, and Philip Kim. Experimental observation of the quantum Hall effect and Berry’s phase in graphene. *Nature*, 438:201–204, Sep 2005, arXiv:cond-mat/0509355.
- [119] Kirill I. Bolotin, Fereshte Ghahari, Michael D. Shulman, Horst L. Störmer, and Philip Kim. Observation of the fractional quantum Hall effect in graphene. *Nature*, 462:196–199, Oct 2009, arXiv:0910.2763.
- [120] Dong-Keun Ki, Vladimir I. Fal’ko, Dmitry A. Abanin, and Alberto F. Morpurgo. Observation of even denominator fractional quantum Hall effect in suspended bilayer graphene. *Nano Letters*, 14:2135–2139, Mar 2014, arXiv:1305.4761.
- [121] Z. Papic, M.O. Goerbig, and N. Regnault. Theoretical expectations for a fractional quantum hall effect in graphene. *Solid State Communications*, 149(2728):1056 – 1060, 2009.